

## Dissertation

# Low alloyed martensitic TRIP assisted Steels by Quenching and Partitioning

ausgeführt zum Zwecke der Erlangung des akademischen Grades eines  
Doktors der technischen Wissenschaften unter der Leitung von

Univ. Prof. Dr. Ernst Kozeschnik

E308

Institut für Werkstoffwissenschaft und Werkstofftechnologie

eingereicht an der Technischen Universität Wien

Fakultät für Maschinenwesen und  
Betriebswissenschaften

von

Dipl.-Ing. Niko Große-Heilmann

Matrikelnummer: 1029573

Brockhäger Straße 12, 33428 Harsewinkel, Deutschland

Wien, am 30. Oktober 2015

## Deutsche Kurzfassung der Dissertation

Die Idee einer neuen, international als Quenching and Partitioning bekannten, Wärmebehandlung zur Herstellung niedriglegierter TRIP unterstützter Stähle mit martensitischer Matrix wird in dieser Dissertation aufgegriffen. Anhand eines niedriglegierten Stahles mit mittlerem Kohlenstoffgehalt und Zugaben von Silizium und Chrom werden geeignete Wärmebehandlungen entwickelt, um mit diesem konventionellen Werkstoff herausragende Eigenschaften zu erreichen.

Das Constrained Carbon Equilibrium Modell wird eingesetzt, um die Wärmebehandlung grundlegend auszulegen. Dieses wird durch analytische und numerische Simulationen der Kohlenstoffdiffusion zwischen Martensit und Austenit unter Berücksichtigung der Mikrostruktur von martensitischen TRIP unterstützten Stählen ergänzt. Die Mikrostruktur und die damit verknüpften Vorhersagen der Diffusionsrechnungen werden mittels Dilatometrie und Transmissions-Elektronen-Mikroskopie validiert. In-situ Versuche im Röntgendiffraktometer ermöglichen die Beobachtung der für Quenching and Partitioning essentiellen Kohlenstoffdiffusion während der Wärmebehandlung.

Längenänderungen, die während der Quenching and Partitioning Wärmebehandlung zu beobachten sind, werden auf kristallographischer Ebene mit den bekannten Einflüssen der martensitischen und der bainitischen Umwandlung sowie der Karbidbildung auf die Gitterkonstanten korreliert. Damit kann analytisch der Einfluss der Kohlenstoffumverteilung auf die Längenänderung während der Quenching and Partitioning Wärmebehandlung beschrieben und durch dilatometrische Experimente verifiziert werden.

Kontraproduktive Effekte wie die Bainitbildung in der Nähe der Martensitstarttemperatur und die Zementitbildung bei erhöhten Partitioning-Temperaturen werden sowohl experimentell untersucht als auch modelliert und simuliert, um ihre negativen Einflüsse durch geschickte Temperaturführung zu vermeiden.

Durch die sich ergebende zweistufige Temperaturführung konnten 20% Restaustenit in 42SiCrB Stahl stabilisiert werden, die nachweislich zu besonderen Eigenschaften führen. Der TRIP Effekt wird qualitativ und quantitativ durch die Phasenanalyse mit Röntgendiffraktometrie ebenfalls nachgewiesen.

Die finale Analyse der erreichten mechanischen Eigenschaften zeigt deutlich die Besonderheiten dieser neuen Stahlfamilie von niedrig legierten TRIP unterstützten Stählen mit martensitischer Matrix. Diese zeichnen sich aus durch ein niedriges Streckgrenzenverhältnis, eine hohe Gleichmaßdehnung sowie hohe Festigkeiten bei gleichzeitig hoher Bruchdehnung.

## Abstract

Low alloyed martensitic TRIP assisted steels, obtained by Quenching and Partitioning heat treatment, attract attention in materials science as well as in the steel industry. Their microstructure promises advanced properties at high strength levels, though many questions arise regarding the interaction between the heat treatment parameters and the metallurgical mechanisms.

Medium carbon steel containing significant amount of silicon is extensively characterized in this study for the application of Quenching and Partitioning heat treatment. In addition to the mechanical properties, which can be achieved, the beneficial carbon partitioning and the counteracting mechanisms bainite formation and cementite precipitation are of particular interest within this study.

The essential carbon partitioning from martensite to austenite is investigated by analytical and numerical simulation and experiments also. X-ray diffraction and dilatometry are used to track the way of carbon in-situ while the Quenching and Partitioning heat treatment is applied. The expected microstructure of low alloyed martensitic TRIP assisted steels is derived from the well-known martensitic transformation kinetics and used to estimate the dimensions and shapes of retained austenite within. The results are validated by Transmission Electron Microscopy and used for the carbon partitioning simulations.

Furthermore, the counteracting carbide precipitation in retained austenite is analyzed by numerical precipitation simulation and dilatometric experiments. The change in length caused by Quenching and Partitioning is derived from the changes in the crystallographic structure and affirmed by dilatometry and X-ray diffraction. Experimental evidence is found that the cementite precipitation is occurring from retained austenite at high carbon levels, caused by partitioning and high dislocation densities, established by the prior martensitic phase transformation.

The effect of bainite formation below martensite start temperature is reviewed and confirmed by dilatometry. The reaction is taken into account by new combination of bainite start regression and the Constrained Carbon Equilibrium model, which allows prediction of reasonable partitioning temperatures avoiding bainite formation.

Finally, the findings are used to develop appropriate Quenching and Partitioning heat treatment of  $42\text{SiCrB}$  steel, avoiding counteracting mechanisms while full carbon partitioning takes place. Outstanding mechanical properties, characterizing a new steel family, are achieved. Due to the TRIP effect, analyzed by means of X-ray diffraction, the retained austenite contributes remarkably to the stress-strain behavior. Low alloyed martensitic steels feature high strength and high uniform- and total elongation due to the significant retained austenite volume fractions, exceeding 20 % in this study.



## Acknowledgement

This dissertation was carried out between July 2010 and April 2015 under the supervision of Univ. Prof. Dr. Ernst Kozeschnik and Prof. Dr. Isabella-Maria Zylla. I am very thankful for the opportunity to work with their research groups in TU Wien and University of Applied Sciences Osnabrück and for the provision of MATCALC software and laboratory facilities.

This work was generously funded by Benteler Steel/Tube GmbH, Paderborn. I want to express my sincere gratitude to Dr. Andreas Peters, who set this prospective research project in motion and pointed the way from start to finish. I wish to acknowledge the support of my team leaders Dr. Christian Kronholz, Dr. Jozef Balun and Dr. Thomas Vietoris.

The readiness for scientific discussions of my co-workers in Paderborn, Osnabrück and Vienna was outstanding, my best wishes to all of you that nobody bursts with curiosity. Special thanks to Elke Herberhold, George Predko and Jayaram Dadda; without your faithful proof-reading it would be a mess.

I am grateful to Prof. Pierre Stadelmann, working at Interdisciplinary Centre for Electron Microscopy (CIME) at École Polytechnique Fédérale de Lausanne, for a free scientific license for JAVA Electron Microscopy Software (JEMS). I pay tribute to the Open Source Community creating and supporting great and helpful software.

Parts of this research were carried out at the light source PETRA III at DESY, a member of the Helmholtz Association (HGF). I would like to thank Norbert Schell and his team for assistance in using beamline Po7.

I owe so much to my beloved wife Daniela for her endless patience, her confidence and her kind encouragement when motivation was low, Thank You.

Zu guter Letzt danke ich meinen Eltern Heinrich und Annette sowie meinen Schwiegereltern Erich und Hannelore dafür, dass Ihr immer für uns und für Eure Enkelkinder Hannah und Justus da seid.

## Contents

1.	Introduction.....	1
2.	Objective .....	2
3.	Background .....	3
3.1.	Transformation Induced Plasticity (TRIP).....	3
3.2.	TRIP assisted Steels.....	4
3.3.	Quenching and Partitioning .....	6
3.4.	Constrained Carbon Equilibrium .....	8
3.5.	Counteracting Mechanisms .....	12
3.6.	Observation .....	15
3.7.	Properties and Application .....	18
3.8.	Crystallography .....	20
4.	Experimental.....	24
4.1.	Material.....	24
4.2.	Phase Transformation Diagrams .....	25
4.3.	Dilatometric Study of Quenching and Partitioning .....	26
4.3.1.	Heat Treatment.....	27
4.3.2.	One-step Quenching and Partitioning .....	28
4.3.3.	Two-step Quenching and Partitioning.....	28
4.3.4.	Tempering of Martensite.....	29
4.4.	In-situ X-Ray Diffraction.....	29
4.4.1.	PETRA III Synchrotron.....	30
4.4.2.	Fast in-situ X-Ray Diffraction.....	30
4.4.3.	Lattice Parameter and Austenite Carbon Content .....	31
4.4.4.	Determination of Retained Austenite Phase Fraction .....	31
4.5.	Tensile Testing .....	34
4.6.	Transmission Electron Microscopy.....	35
4.7.	X-Ray Diffraction .....	36
5.	Simulation.....	38
5.1.	CALculation of PHase Diagrams (CALPHAD).....	38
5.2.	Simulation of the Martensitic Transformation.....	39
5.3.	Cementite Precipitation in Austenite .....	40
5.4.	Stability of Retained Austenite in Absence of Cementite.....	43
5.5.	Microstructural Aspects of Quenching and Partitioning.....	44
5.6.	Diffusivity of Carbon.....	46
5.7.	Analytical Simulation of Carbon Partitioning.....	48
5.7.1.	Random Walk.....	48

---

5.7.2.	Analytical Solution for planar Interface .....	49
5.7.3.	Analytical Solution for infinite thin Plate .....	50
5.7.4.	Analytical Solution for spherical Interface .....	52
5.8.	Numerical Simulation of Carbon Partitioning .....	54
5.8.1.	DICTRA Simulation with mobile Interface.....	55
5.8.2.	MATCALC Diffusional Simulation with stationary Interface.....	57
6.	Results.....	60
6.1.	Phase Transformation Diagrams .....	60
6.2.	Dilatometry of Quenching and Partitioning.....	66
6.2.1.	One-step Quenching and Partitioning .....	66
6.2.2.	Two-step Quenching and Partitioning.....	68
6.2.3.	Tempering of Martensite .....	69
6.3.	In-Situ X-Ray Diffraction.....	70
6.3.1.	One-step Quenching and Partitioning .....	70
6.3.2.	Two-step Quenching and Partitioning.....	74
6.3.3.	Quenching and Tempering .....	80
6.4.	Mechanical Properties.....	82
6.4.1.	Two-step Quenching and Partitioning.....	82
6.4.2.	Quenching and Tempering .....	84
6.5.	Transmission Electron Microscopy .....	85
6.6.	X-Ray Diffraction .....	87
7.	Discussion.....	89
7.1.	Change in Length during Quenching and Partitioning .....	89
7.2.	Carbon Partitioning .....	92
7.3.	Counteracting Cementite Precipitation .....	97
7.4.	Counteracting Bainite Formation.....	99
7.5.	Mechanical Properties.....	101
8.	Summary.....	104
9.	References.....	105
10.	Appendix.....	116

## 1. Introduction

The high value for money is the most important advantage ensuring outstanding economic success of low alloyed steel. The possibilities to enhance low alloyed steels and contribute to weight and cost savings or higher product performance are limited since the necessary increase in strength lowers the available ductility. New strengthening mechanisms besides the well-known work-, precipitation-, solid solution- and grain boundary- hardening, all hindering dislocation movement and obviously reducing ductility as well, are required to overcome this dilemma. One mechanism to strain materials without dislocation movement is Transformation Induced Plasticity (TRIP).

This effect was discovered in 1924 by Albert Sauveur finding “that” increased hot ductility within pure iron near the phase transformation temperature at 900 °C [Sauveur1924]. The effect was not available at room temperature until 1967 when high alloyed metastable austenitic steels were researched by Victor F. Zackay et al. [Zackay1967]. In 1979, amounts of up to 20 % of the retained austenite were found in silicon containing low alloyed steels after bainitic phase transformation and the carbon partitioning from ferrite to austenite was observed [Bhadeshia1979].

Carbon enriched retained austenite is the solution for an economic stabilization of austenite and the successful broad use of Transformation Induced Plasticity (TRIP) in low alloyed steels. In 1987, the first generation of TRIP assisted steels was developed on the basis of a matrix from proeutectoid ferrite and bainite by Osamu Matsumura et al. [Matsumura1987]. This type of TRIP steel presently comprises the standard part of the commercial product range of steel producers and are used in industry, e.g. in automotive crash components.

The concept of Quenching and Partitioning was introduced in 2003 as a novel heat treatment for low alloyed high strength steels [Speer2003]. The idea to construct a TRIP assisted steel upon a martensitic matrix offers the opportunity to enlarge the portfolio of TRIP assisted steels to higher strength levels. Due to the lean alloying concept, an economic success of martensitic TRIP assisted steels is extremely likely and this topic is an important part of recent research. Recently, ten years after their invention, first variants of martensitic TRIP assisted steels reached prototype status.

There are already models, simulations and results available in the literature, nevertheless valid information about the design of Quenching and Partitioning heat treatments is barely available and spread. It is undeniable today that austenite stabilizing carbon partitioning occurs and that the Constrained Carbon Equilibrium model gives reasonable advice for suitable quenching temperatures. Furthermore, carbide formation and bainite phase transformation are already identified as counteracting mechanisms.



## 2. Objective

The retained austenite stabilized by Quenching and Partitioning promises outstanding mechanical properties due to the TRIP effect. The more retained austenite available, the more TRIP effect is expected. Unfortunately it is evident, that the possible volume fractions of retained austenite, proposed by the Constrained Carbon Equilibrium Model, are never achieved. Counteracting bainite formation, secondary martensite and cementite precipitation are observed instead.

Drawing on the example of  $42\text{SiCrB}$  steel, with probable sufficient cementite suppressing silicon content, Quenching and Partitioning is explored experimentally with regard to the counteracting mechanisms during Partitioning after full austenitization and quenching.

It is further intent of this study to identify and develop models for the carbon diffusion from martensite to austenite, the counteracting bainite formation and the cementite precipitation as this is necessary to optimize the heat treatment parameters.

Finally optimized heat treatments have to be realized in laboratory scale to test the associated mechanical properties. These heat treatments should of course prevent counteracting mechanisms by using the gathered intelligence to stabilize as much retained austenite as possible, since best mechanical properties are expected then.

### 3. Background

Martensitic TRIP assisted steels are part of a new category of steels with unique microstructure and resulting particular properties. To expose their unique qualities it is necessary to take a closer look at the TRIP effect and its thermodynamic conditions. From the resulting chemical prerequisites, the idea and history of TRIP effect in steels are described in this chapter. Furthermore, the differences between TRIP steels, TRIP assisted steels and martensitic TRIP assisted steels are highlighted. Ultimately, the available models and newest achievements of martensitic TRIP assisted steels are summarized.

#### 3.1. Transformation Induced Plasticity (TRIP)

The martensitic phase transformation is the basis for Transformation Induced Plasticity. The thermodynamic instability of austenite at lower temperatures is responsible for martensitic transformation to occur. The difference in the free Gibbs energy of austenite  $\gamma$  and martensite  $\alpha'$  is the driving force for the phase transformation, see figure 1.

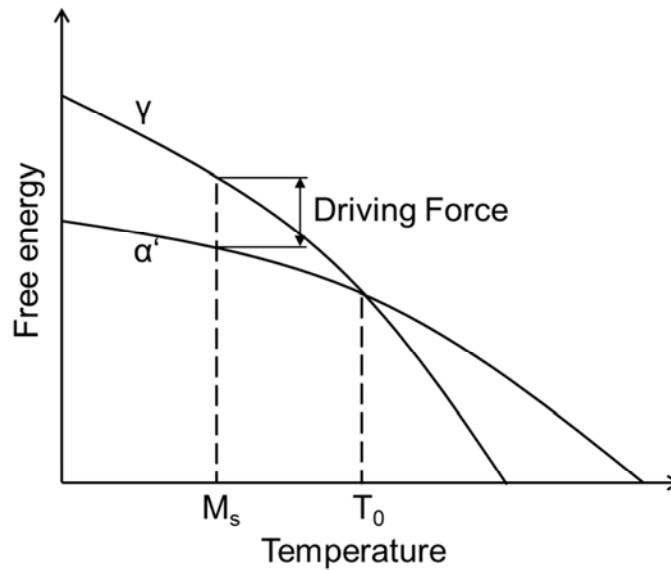


Figure 1: Driving force for martensitic  $\gamma$  to  $\alpha'$  transformation [Nishiyama1978]

Considering only the chemical energies, the phase transformation from austenite to ferrite has to start when the temperature falls short of  $T_0$  temperature, in which the Free Gibbs Energies of both phases are equal. To initiate the phase transformation, the system must overcome additional non-chemical energy barriers, necessary for the creation of new surfaces, compensation of elastic stresses and plastic deformation due to volume expansion and shear. This energy is in the order of 1250 J/mol for low alloyed steels, dependent on micro structural conditions [Nishiyama1978]. If the chemical driving force exceeds this barrier, the austenite transforms spontaneously with the corresponding temperature is defined with the martensite start temperature

$M_s$ . In low alloyed steels, the transformation proceeds especially with falling temperature; therefore it is called “athermal martensite”. [Nishiyama1978]. In this context, the temperature with which the transformation is complete is defined as the “martensite finish  $M_f$  temperature”. At this point it should be stated, that all phase transformations, including the athermal martensitic ones of low alloyed steels, involve a nucleation and growth process. A strict athermal definition is at odds with the classical nucleation theory, since nucleation is always a time dependent probabilistic process, even if it is very fast. Nevertheless the term athermal is useful to distinguish this athermal singularity from regular isothermal martensitic phase transformations.

Isothermal martensite on iron basis is reported especially in high alloy steels and Fe-Ni alloys. Annika Borgenstam and Mats Hillert reviewed the available experimental data in [Borgenstam1997] and concluded that isothermal martensite is observed in low alloyed high carbon steels as well, e.g. in the study of Muneo Oka and Hisaki Okamoto on hypereutectoid steels [Oka1988]. The isothermal martensite start temperature  $M_{si}$  is mainly dependent on the chemical composition. Both reactions can take place in the same alloy [Nishiyama1978].

For temperatures between martensite finish  $M_f$  and  $T_o$ , the martensitic transformation cannot finish by formation of athermal martensite as the chemical driving force is too small, i.e. the retained austenite is arrested in a metastable state. Additional elastic stress and plastic deformation can help to overcome the barrier and initiate the transformation. This effect is significant if no athermal martensite is formed, i.e. above martensite start temperature  $M_s$ . The growth of martensite in low alloyed steels is associated with a volumetric increase and a shear deformation, contributing to the plasticity of the steel. This is defined as the “TRIP” effect.

The contribution of ideal transformation plasticity to the total elongation of a fully austenitic tensile sample is estimated by Harshad K. D. H. Bhadeshia [Bhadeshia2002] to be 15 % at maximum. For conventional TRIP assisted steels, typically containing up to 0.15 volume fraction of retained austenite, the contribution of ideal transformation plasticity is reduced to 2 % maximum. Nevertheless, TRIP assisted steels exceed conventional steels in uniform elongation for at least 5 % [TKSE2009] [ArcelorMittal2013]. Harshad K. D. H. Bhadeshia [Bhadeshia2002] suggests that multiphase steels show additional beneficial properties because of their composite structure made from both a hard and a soft phase to be used in addition to compressive stress generated due to the increase of volume during the martensitic transformation that enhances the properties of TRIP-steels.

The mechanical behavior of TRIP steels is temperature dependent. At low application temperatures, a spontaneous athermal martensitic transformation is expected due to undercooling, as shown for TRIP assisted steels by Niels van Dijk et al. [Dijk2005]. At elevated temperatures above  $T_o$  temperature no TRIP effect is reported because the retained austenite is thermodynamically stable and the necessary driving force is absent.

### 3.2. TRIP assisted Steels

The TRIP related temperatures  $M_s$ ,  $M_d$ ,  $T_o$  and  $M_f$  are mainly dependent on the chemical composition. It is conceivable to compose an alloy with TRIP effect for room temperature applications. Regression formulas to approximate the martensite start

temperature of low alloyed steels are available, e.g. the linear Andrews equation (1). The martensite start temperature  $M_s$  has to be used in °C and  $c_x$  is the concentration of element x in wt.% [Andrews1965] in this example.

$$M_s = 539 - 423 c_C - 30,4 c_{Mn} - 12,1 c_{Cr} - 17,7 c_{Ni} - 7,5 c_{Mo} \quad (1)$$

The equation (1) illustrates the impact of important alloying elements demonstrating that carbon has a very strong influence on the martensite start temperature  $M_s$  compared to the other elements. Only 1.3 wt.% of Carbon can lower  $M_s$  to room temperature theoretically, but the linear extrapolation of K. W. Andrews regression, based on low and medium carbon level steel data to high carbon contents is doubtful.

Furthermore, low alloyed steels with more than 1.3 wt.% of carbon are not available commercially [Stahlschluessel2013], because of the very high austenitization temperature necessary to dissolve all carbides creating larger austenite grains and corresponding negative properties. Even within the Fe 1.7 wt.% C system, a mixed microstructure of martensite and retained austenite is reported by Eduard Houdremont [Houdremont1956], i.e. martensite start temperature above room temperature. Nishiyama reviewed research activities on the influence of the austenite grain size on the martensite start temperature and it was reported that the transformation starts earlier while the grains are of a larger size [Nishiyama1978]. Hence, fully austenitic Fe-C steels are not available at room temperature.

Designing TRIP steel by adding substitutional alloying elements reducing martensite start temperature below room temperature results in high alloyed concepts. These high alloyed metastable austenitic steels have been recognized since 1967 when Zackay et al. confirmed their enhanced ductility [Zackay1967]. These high alloyed metastable austenitic steels are available commercially, e.g. X10CrNi18-8 (1.4310) or X2CrNi18-9 (1.4307) [Roth2009], and they are often referred to as “TRIP steels”. Because of the high alloying cost austenitic steels never reached mass production for cars, though they possess superior properties. The sports car DeLorean DMC-12 with its car body build from austenitic steel was one of the rare attempts with minimal economic success.

An additional 20 years of research was necessary to introduce TRIP to low alloyed steels. The development of ferritic/martensitic dual phase (DP) steels produced by intercritical annealing together with the basic understanding of the bainite transformation of low alloyed silicon containing steels [Bhadeshia1980] lead Matsumura et al. to the idea of TRIP assisted steels. Intercritical annealing and austempering, i.e. isothermal bainite transformation of 0.4 wt.% C, 1.5 wt.% Si, 0.8 wt.% Mn low alloyed steel, established a multiphase microstructure of ferrite, bainite and carbon enriched retained austenite with TRIP effect [Matsumura1987]. The term “assisted” indicates that TRIP assisted steels are distinguished from fully austenitic metastable TRIP steels, noted by their non-austenitic matrix.

Today’s TRIP assisted steels are available based on a matrix of proeutectoid ferrite and bainite matrix, as shown in figure 2. Yield Strength ranges in the dimension of 400 to 500 MPa, Tensile Strength from 700 to 800 MPa and the total elongation exceeds 20 % [TKSE2009][ArcelorMittal2013]. The distinguished property of TRIP assisted steels is the high strain hardening behavior resulting in high uniform elongation and high tensile strength combined with a low yield ratio. Due to the improved ductility and high tensile strength, TRIP steels exhibits high energy absorption potential and show

promise in fail safe design. The high uniform elongation also allows complex formed components. Low alloyed TRIP-Steels are presently used in industrial applications, e.g. in automotive crash elements.

In summary, there are two types of TRIP steels at room temperature commercially available today: high alloyed fully or partly austenitic TRIP steels and low alloyed TRIP assisted steels with ferritic / bainitic matrix. Presently, martensitic TRIP assisted steels manufactured by Quenching and Partitioning are under development.

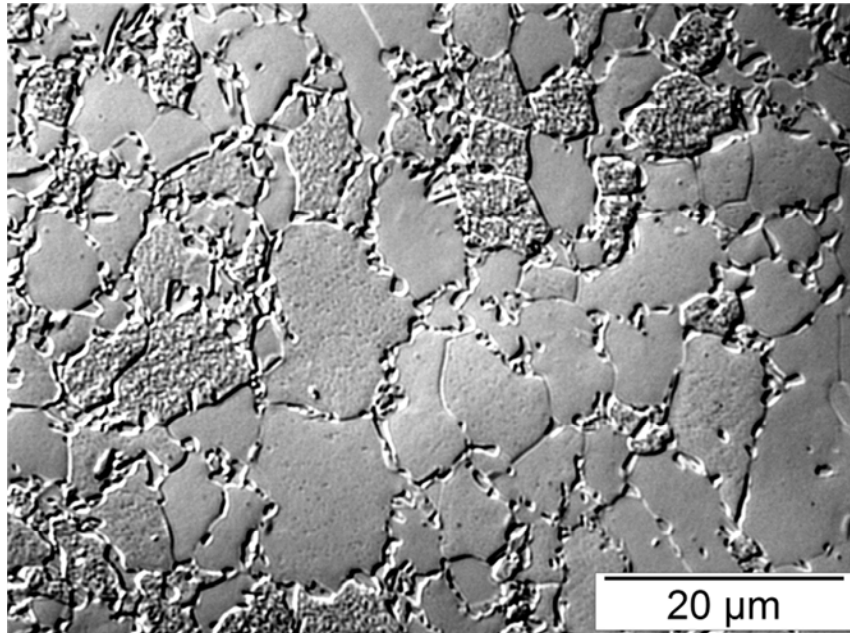


Figure 2: Grayscale Light micrograph of ThyssenKrupp RA-K<sup>®</sup> 40/70 TRIP assisted steel in differential interference contrast. Sub structured grey bainite grains, smooth grey ferrite grains and small white retained austenite islands become apparent after electrochemical polishing

### 3.3. Quenching and Partitioning

Quenching and Partitioning was introduced in 2003 as novel heat treatment by John G. Speer et al. [Speer2003]. As shown in figure 3, the Quenching and Partitioning heat treatment is creating a three phase microstructure, consisting of low carbon martensite  $m_1$ , high carbon martensite  $m_2$  and retained austenite  $\gamma$ . It should be noted that the corresponding heat treatment can be divided into two parts:

During the quenching step, the steel is usually fully austenitized at austenitization temperature ( $A_T$ ) and then quenched to a temperature between the martensite start  $M_s$  and martensite finish  $M_f$  temperature, called “quenching temperature” ( $Q_T$ ). Accordingly, the microstructure is composed of martensite  $m_1$  and austenite  $\gamma$  with equal carbon content with diffusion fully suppressed during the rapid cooling process.

Due to the high difference in chemical potentials, carbon diffuses from supersaturated martensite  $m_1$  to austenite  $\gamma$  during the subsequent partitioning step at “partitioning temperature” ( $P_T$ ). If the partitioning temperature equals the quenching temperature,

the process is called “one-step” otherwise “two-step” Quenching and Partitioning. With the inclusion of the austenite stabilizing effect of carbon, the martensite finish temperature of the carbon-enriched austenite is decreased below room temperature. Hence, after final quenching to room temperature carbon-enriched austenite remains untransformed. If the martensite start temperature of high carbon austenite remains above room temperature additional high carbon martensite  $m_2$  originates.

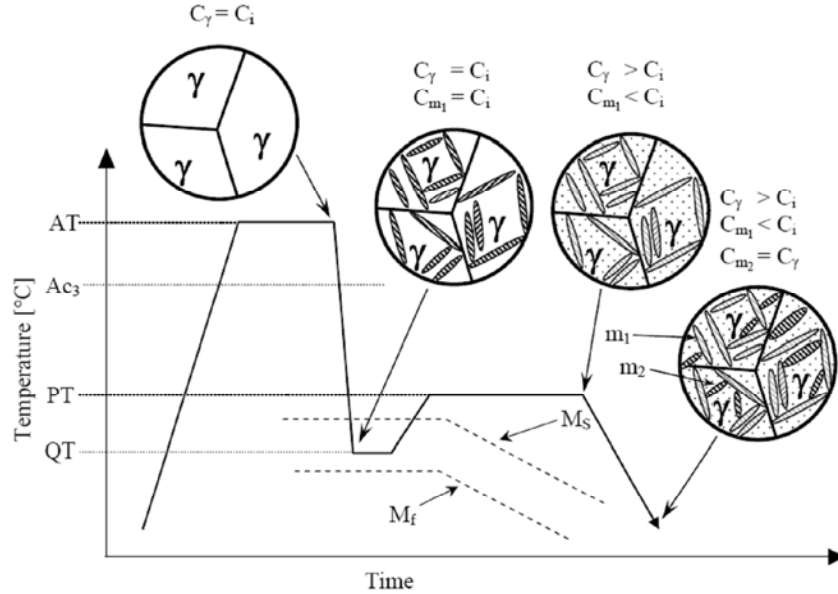


Figure 3: Schematic Quenching and Partitioning heat treatment creating low alloyed martensitic TRIP assisted steel [Speer2003a]

Several production routes for martensitic TRIP assisted steels have been proposed. Integrated routes attempt to apply the Quenching and Partitioning process directly to hot rolling or forging of long products during the manufacturing process, cf. [Thomas2008] [Futch2012]. Subsequent routes perform the heat treatment to final products, e.g. during hot stamping [Liu2011][Liu2011a] or as usual heat treatments for cold rolled automotive sheet steels, similar to the manufacturing process of conventional TRIP assisted steels [Wang2011a].

Considerable research in the field of quenching and partitioning uses intercritical annealing for TRIP assisted steels processing. Industrially available TRIP assisted steels with their typical chemical compositions (0.2 wt.% C, 1.5 wt.% Mn and 1.5 wt.% Si) are often used in the context of Quenching and Partitioning, cf. [Streicher2004] [Edmonds2006a] [Santofimia2008a] [Santofimia2008b] [Clarke2008] [DeMoor2008] [DeMoor2011]. Due to the prior isothermal heat treatment in the two phase region from proeutectoid ferrite and austenite a final microstructure of proeutectoid ferrite, martensite and retained austenite is obtained.

Recently, Chinese researchers suggested that an alternative Quenching-Partitioning-Tempering (Q-P-T) process enhances the mechanical properties by the additional use of precipitation hardening [Hsu2007] [Zhang2011] [Zhou2012] [Gao2013] [Hsu2013]. A Stepping-Quenching-Partitioning (S-Q-P) process with two Quenching and Partitioning steps at descending Quenching Temperature in sequence is proposed by YueFeng Zhu [Zhu2012] in addition.

### 3.4. Constrained Carbon Equilibrium

Along with the Quenching and Partitioning heat treatment the Constrained Carbon Equilibrium (CCE) was introduced by John G. Speer et al. [Speer2003] It is “[...] defined by complete absence of iron or substitutional atom movements, along with freedom of the carbon (or interstitial) atoms to migrate as needed.”

To avoid confusion with the essential definition of paraequilibrium, the original designation Constrained Paraequilibrium (CPE) was renamed as Constrained Carbon Equilibrium (CCE) in discussion with Mats Hillert and John Ågren, who reviewed the definitions with John G. Speer [Hillert2004][Speer2004]. In contrast to paraequilibrium, the interface is assumed as immobile under constrained carbon equilibrium condition, i.e. the phases are already formed, neither iron nor substitutional elements move. Mats Hillert and John Ågren [Hillert2004] further noted that it is difficult to avoid any changes in the substitutional compositions at the interface after the occurrence of partitioning at high temperatures or with long partitioning times.

The application of Constrained Carbon Equilibrium to Quenching and Partitioning heat treatment offers the final carbon distribution after a complete partitioning between quenched martensite and retained austenite, provided that carbide formation and phase transformation are fully suppressed. For low alloyed steels it is valid to use the estimation that all carbon diffuses into the austenite, because the content of carbon in martensite, respectively ferrite, under equilibrium conditions is very small. By this approximation the concentration of carbon in austenite  $c_C^Y$  can be derived by the volume fraction of austenite  $V^Y$  and the total carbon content of the alloy  $c_C^{\text{alloy}}$  by the following expression [Speer2003]:

$$c_C^Y = \frac{1}{V^Y} \cdot c_C^{\text{alloy}} \quad (2)$$

From this formula, it is possible to construct a best case approximation of the maximum achievable amount of retained austenite if a description of the martensitic phase transformation is available.

In addition, the volume fraction of martensite  $V^{\alpha'}$  can be best described mathematically as a function of the temperature  $T$  by the Koistinen and Marburger relationship, see equation (3) [Koistinen1959]. The constant  $\alpha$  is 0.011 for pure Fe-C alloys and plain carbon steels if temperatures are inserted in °C. Although the equation was found empirically by plotting data logarithmically against the difference between  $M_s$  and  $T$ , recent work of Hong-Seok Yang and Harry Bhadeshia confirmed the physical validity under certain restrictions [Yang2009].

$$V^{\alpha'} = 1 - e^{-\alpha(M_s - T)} \quad (3)$$

More recent work, e.g. Sung J. Kim and Jérémy Epp [Kim2008][Epp2012], use a slight modification of the Koistinen-Marburger equation, cf. equation (4), to achieve higher corresponding rate of accuracy in regression analysis of phase transformation data obtained from dilatometric measurements. The first mentioning of this equation is published by Hans Paul Hougardy around 1984 [Hougardy1984], but it is likely much older.

$$V^{\alpha'} = 1 - e^{-\alpha(M_s - T)^n} \quad (4)$$

The combination of DeMeyer's linear regression formula [DeMeyer2002] for martensite start temperature in equation (5), considering Si and Al content, and equation (3) defines the amounts of martensite and austenite after initial quenching.

$$M_s^I = 539 - 423c_C^{\text{alloy}} - 30.4c_{\text{Mn}}^{\text{alloy}} - 7.5c_{\text{Si}}^{\text{alloy}} + 30c_{\text{Al}}^{\text{alloy}} \quad (5)$$

The stabilization due to partitioning is represented by replacing the nominal carbon content in equation (5) with the carbon content of austenite after complete partitioning under Constrained Carbon Equilibrium conditions, cf. equation (2). The resulting martensite start temperature of carbon enriched austenite becomes:

$$M_s^{\text{II}} = 539 - 423c_C^{\text{Y}} - 30.4c_{\text{Mn}}^{\text{alloy}} - 7.5c_{\text{Si}}^{\text{alloy}} + 30c_{\text{Al}}^{\text{alloy}} \quad (6)$$

As long as the martensite start temperature of carbon enriched austenite remains below room temperature (RT), all carbon enriched austenite remains stable after final quenching. If it is above room temperature, some amount of the carbon enriched austenite decomposes to carbon enriched martensite. Using the Koistinen-Marburger relationship and scaling to the phase fraction of carbon enriched austenite, the content of carbon enriched martensite is given by:

$$V^{\alpha_2'} = (1 - e^{-\alpha^*(M_s^{\text{II}} - \text{RT})}) \cdot V^{\text{Y}} \quad (7)$$

John G. Speer proposed this model to estimate the quenching temperature creating maximum content of retained austenite. Figure 4 shows the result of 0.60 wt.% C, 0.95 wt.% Mn and 1.96 wt.% Si steel [Gerdemann2004]. The shark fin shape is characteristic for the retained austenite volume fraction calculated by the CCE model. The maximum amount of carbon enriched retained austenite is achieved if the martensite start temperature after partitioning is at room temperature. Very high volume fractions of carbon enriched austenite are proposed.

Figure 5 shows a comparison of the model and corresponding experiments, see figure 5, revealing similar characteristics. However the experimental data show less content of retained austenite at all quenching temperatures. This behavior is attributed to the best case estimation of full partitioning, stationary interfaces and totally suppressed carbide formation and it suggests that neglected competing mechanisms are present in the experiments [Gerdemann2004].



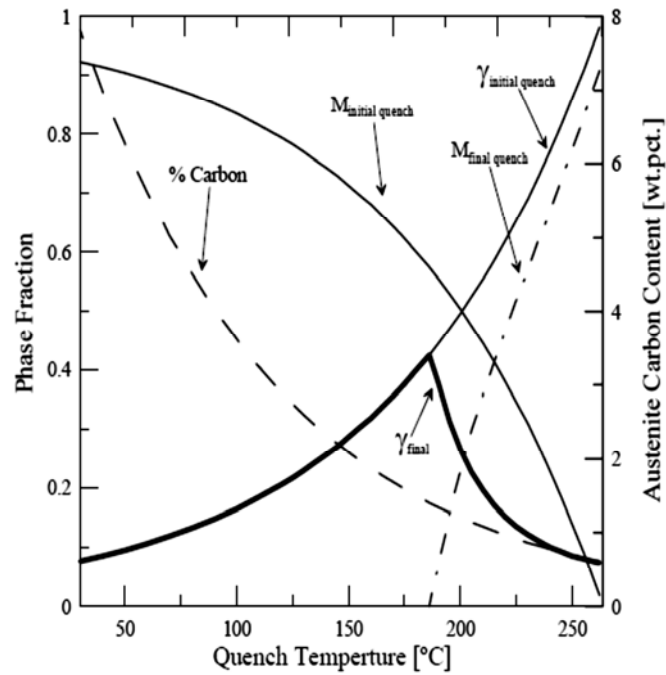


Figure 4: Approximation of retained austenite volume fraction in dependence of Quench Temperature for 0.60 wt.% C, 0.95 wt.% Mn and 1.96 wt.% Si medium carbon bar steel [Gerdemann2004]

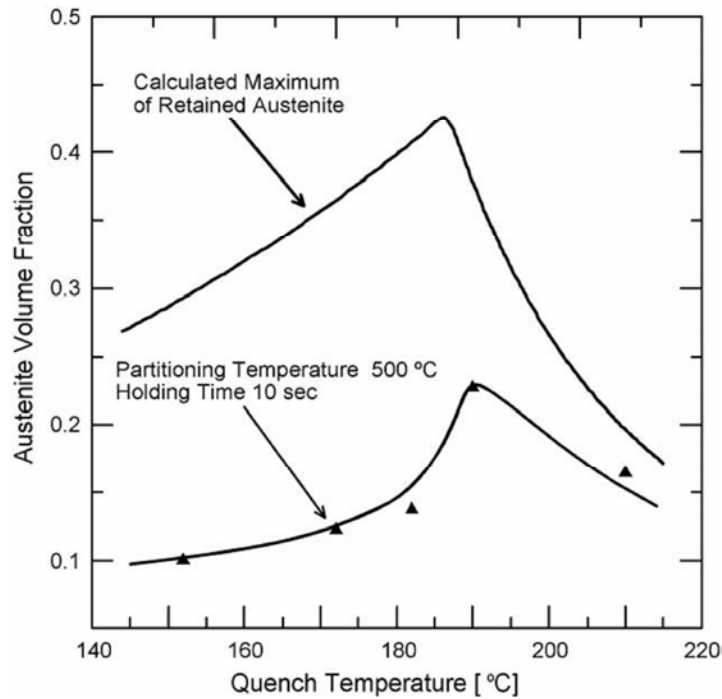


Figure 5: Calculated and measured retained austenite in a 0.60 wt.% C, 0.95 wt.% Mn and 1.96 wt.% Si medium carbon steel after two-step Quenching and Partitioning heat treatment [Gerdemann2004]

The previously demonstrated model using Constrained Carbon Equilibrium does not consider any kinetic aspects, thus it is limited in parameters and prediction possibilities, i.e. the quenching temperature is the only process factor included. On the other hand numerical methods offer the opportunity to analyze kinetic aspects as well required during the partitioning phase when diffusion becomes part of the equation.

David Edmonds et. al. [Edmonds2006] simulated the carbon diffusion from martensite to austenite during the partitioning phase with Diffusion Controlled phase TRAnsformations (DICTRA) software under CCE conditions:

- austenite and martensite are infinite plate-shaped,
- no existence of phase transformations,
- diffusion occurs normal to the interface
- with identical initial composition of austenite and martensite,
- 0.19 wt.% C–1.59 wt.% Mn–1.63 wt.% Si as chemical composition,
- partitioning at 400 °C,
- 0.3  $\mu\text{m}$  ferrite lath and 0.14  $\mu\text{m}$  austenite lath (taken from TEM investigation).

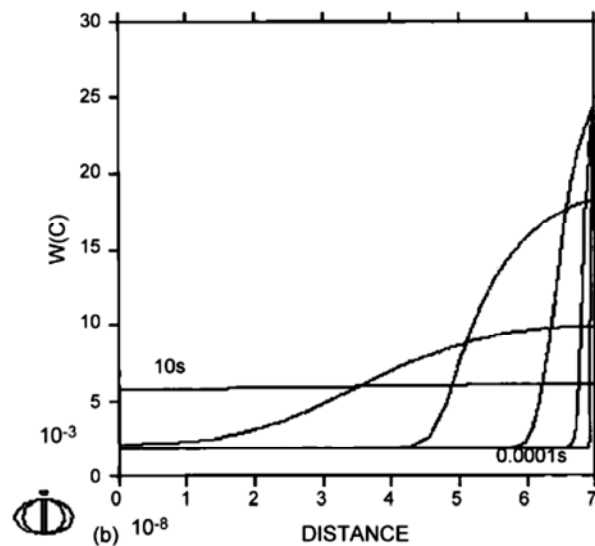


Figure 6: The carbon concentration profiles calculated perpendicular to the planar interface for austenite plate-shaped region for different partitioning times from 0.0001, 0.001 to 10 s in Fe–0.19% C–1.59% Mn–1.63% Si (wt.%) partitioned at 400 °C [Edmonds2006]

The calculation, see figure 6, shows very high carbon concentrations next to the interface in the onset of the process. Homogenous carbon distribution in austenite is reached after approximately 10 s at 400 °C partitioning temperature [Edmonds2006]. In addition to the work of David V. Edmonds, Amy Clarke, née Streicher, et al. [Clarke2009] performed similar diffusion calculations under CCE conditions with DICTRA software predicting the local distribution of carbon in the austenite as well. Upon completion of the process, the stable austenite fractions are calculated using the best case approach of Speer with Koistinen-Marburger equation. Results of the simulation are shown in figure 7.

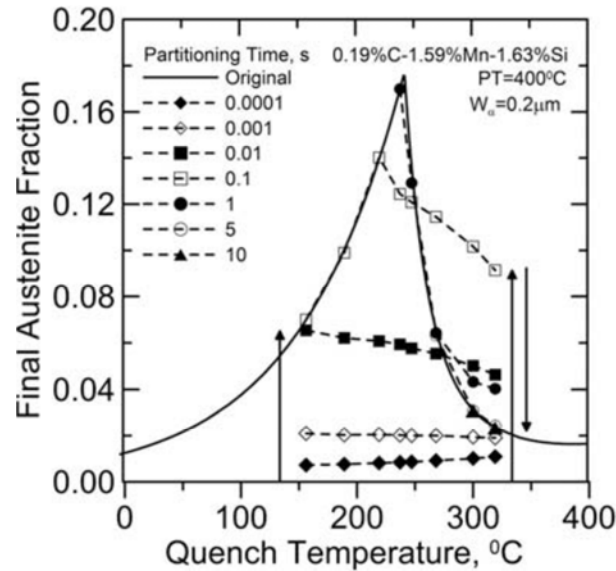


Figure 7: Simulation of 0.19 wt.% C, 1.59 wt.% Mn, 1.63 wt.% Si steel using local carbon distribution at 400 °C, ferrite and austenite half lath width were 0.1 μm; compared to the original model of Speer [Clarke2009]

It is noteworthy that due to the local carbon aggregation at the interface, the retained austenite fraction overcomes the best case approach of Speer at high quenching temperatures and short partitioning times. Due to the CCE approach, the model converges to the best case model of Speer after full homogenization of carbon in the austenite.

In this case, the approximation of optimal quenching temperature is extended by kinetic carbon partitioning simulation. Further process parameters, i.e. partitioning temperature and partitioning time are predictable.

### 3.5. Counteracting Mechanisms

There are still reservations with the Constrained Carbon Equilibrium approach, as it assumes immobile interfaces and fully suppressed carbides that is not the case in real situations. Several investigations determine cementite and transitional carbide precipitation as well as displacive bainite formation. [Edmonds2006] [Zhong2006] [Clarke2008] [Nayak2008] [Li2010] [Mola2013]

It is obvious that carbides are counterproductive in Quenching and Partitioning heat treatment process. When carbides form in the austenite or martensite, less free carbon is available for the stabilization of retained austenite, which is beneficial for the overall mechanical properties. Effective measures are required to prevent carbide formation. Generally, the cementite precipitation is successfully suppressed within the austenite using either high silicon (>1.2 wt.%) or high aluminum (>1.1 wt.%) content, cf. [Zhou2011][Santofimia2008a]. Experiments without aluminum and silicon by David K. Matlock et al. [Matlock2003] accordingly show phase fractions of retained austenite below 0.07.

Ernst Kozeschnik and Harshad K. D. H. Bhadeshia [Kozeschnik2008] explained the effect of silicon on the cementite precipitation in austenite by the use of simulation with MATCALC software under paraequilibrium conditions. This addition of silicon drastically slows down the cementite precipitation, because of considerable reduction of the chemical driving force under paraequilibrium condition, cf. figure 8 and figure 9.

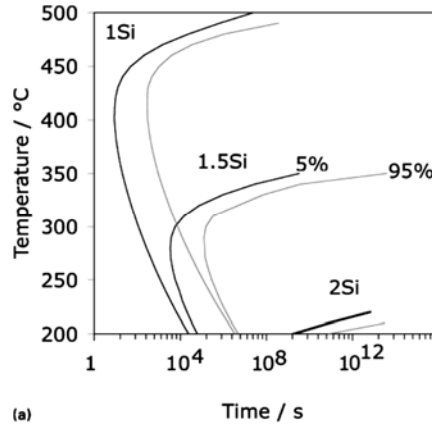


Figure 8: Time temperature precipitation diagram for paraequilibrium cementite in low alloyed steel with 1.2 wt.% C, 1.5 wt.% Mn, 1.5 wt.% Si (percentages represent portion of completed cementite precipitation) [Kozeschnik2008]

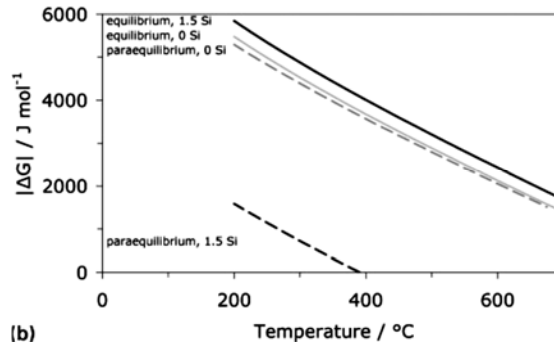


Figure 9: Magnitude of free energy change accompanying  $\gamma \rightarrow \alpha + \gamma$  reaction for both equilibrium and paraequilibrium conditions as function of silicon concentration of austenite [Kozeschnik2008]

Currently, there are no reliable thermodynamic descriptions for transitional carbides available. Accordingly, transitional carbide precipitation simulations are viable. Experimental investigations are available, e.g. John G. Speer observes that transitional carbides during Quenching and Partitioning heat treatment and asked the scientific community to develop new alloying concepts to avoid them [Speer2004]. David V. Edmonds [Edmonds2006] additionally confirms that transitional and  $\epsilon$ -Carbides in the 0.60 wt.% C, 0.95 wt.% Mn and 1.96 wt.% Si medium carbon bar steel by Transmission Electron Microscopy as well. Based on these studies they suggested that silicon is unable to suppress transitional carbide formation, he opined that the lowest partitioning temperature should be high enough to avoid transitional carbides as

shown schematically in figure 10. Furthermore, he proposed that transitional carbides may likely dissolve at higher temperatures.

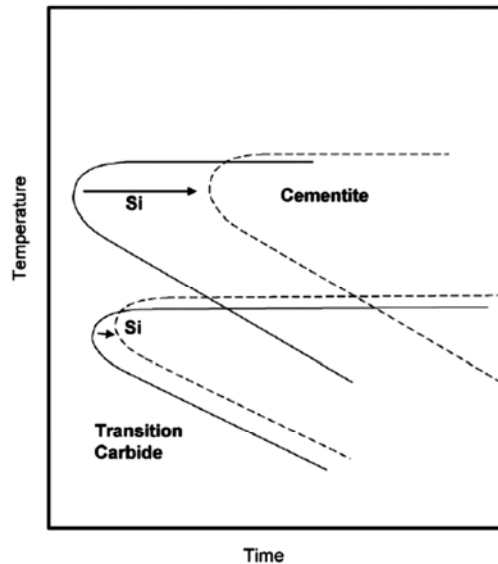


Figure 10: Schematic Influence of Silicon on Cementite and Transitional Carbides [Edmonds2006]

Additionally, MTDATA Simulations, cf. figure 11, shown by Maria J. Santofimia et al. [Santofimia2008] result in rapid carbon partitioning at 400 °C for nanometer-sized austenite microstructures. Furthermore, interface migration is also considered, showing “significant and bi-directional movement of the bcc-fcc interface” having a high negative impact on the amount of austenite retained.

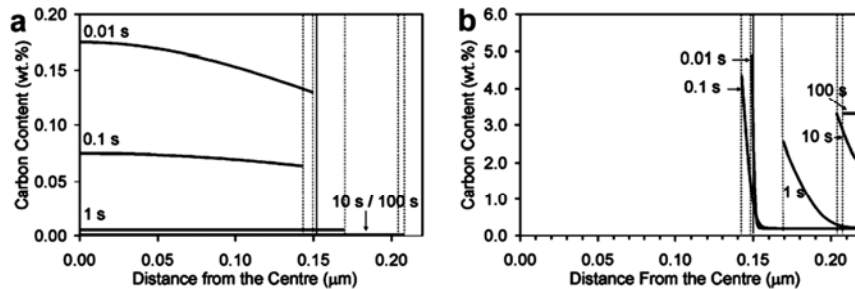


Figure 11: Calculated carbon profiles in a) bcc and b) fcc during partitioning at 400 °C [Santofimia2008]

During very early stages of partitioning at elevated temperatures, the austenite may grow, but is limited to within a half a second as the direction turns and martensite is growing until the equilibrium phase fractions are finally reached. The simulated austenite lath and the related retained austenite phase fraction are reduced drastically. Maria J. Santofimia et al. [Santofimia2009] tested their model in consideration of distinct levels of interface mobility and proposed a strong dependence on the retained austenite phase fraction.

Bainite formation during Quenching and Partitioning heat treatments is claimed by many authors, actually since the first results of David Matlock, Volker Bräutigam and

John Speer [Matlock2003]. In recent research, e.g. the work of Dong Kim et al. [Kim2009] and Stefan van Bohemen et al. [vanBohemen2008] isothermal phase transformations are observed and they are most probable related to bainite formation, though incontestable proof is still not achieved.

### 3.6. Observation

Martensitic TRIP assisted steels obtained by Quenching and Partitioning are dominated by their high strength martensite matrix. Hence, it is appropriate to know about the microstructure of martensite and its evolution. The first packet of martensite nucleating in an austenite grain grows usually from grain boundary to grain boundary. This leaves less space for the next generation of packages, which become shorter and shorter. The martensite formation in low alloyed steels is depicted schematically in figure 12, taken from Hans Paul Hougardy [Hougardy1990].

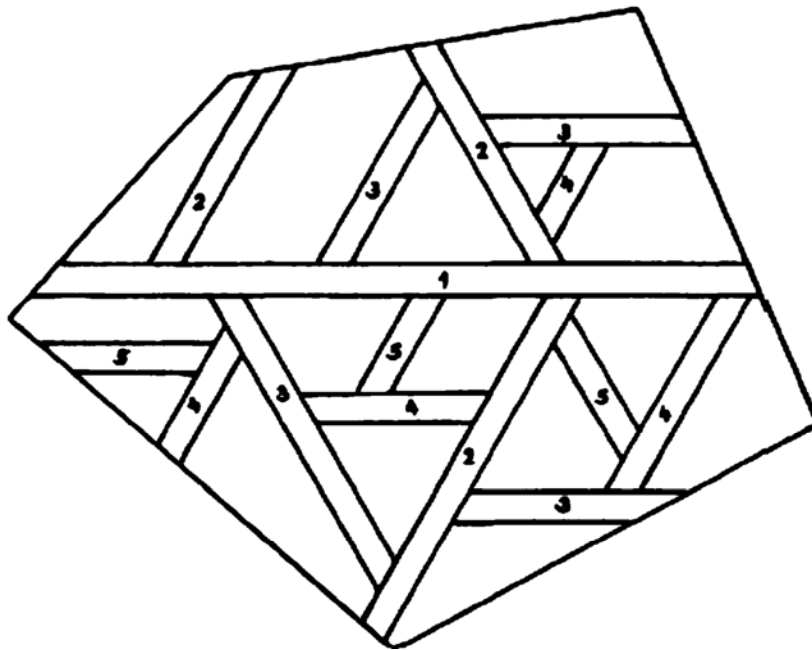


Figure 12: Formation of martensite within the prior austenite grain. The martensite plates grow in sequence from 1 to 5. With ascending number the plates become shorter [Hougardy1990]

Additionally, snapshots of Toshihiko Koseki's recommendable in-situ video of the martensitic transformation of 0.18 wt.% C, 0.2 wt.% Si, 0.9 wt.% Mn, 2.9 wt.% Ni, 1.5 wt.% Cr and 0.4 wt.% Mo steel [Koseki2011] are shown in figure 13 to impart a realistic impression of the process. The observed changes in the topography of the surface are caused by the displacive character of the athermal martensitic phase transformation. It should be mentioned here that the visible austenite grain size of 150  $\mu\text{m}$  is unlikely in steels and is created artificially, but the effects become broader.

The creation of new packets within the prior austenite grain is clearly visible and the sequence, suggested by Hans Paul Hougardy [Hougardy1990], can be reconstructed following the descending length of the packets.

This work is using the common definitions of George Krauss [Krauss1990] to designate the single parts of the martensite structure. Hiromoto Kitahara [Kitahara2006] provided a perfect depictive representation of these, cf. figure 14.

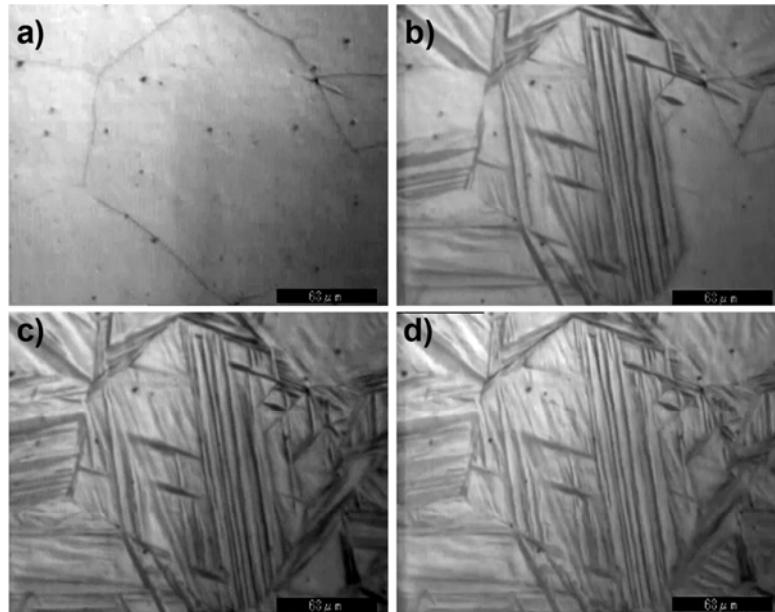


Figure 13: Snapshots from a movie of martensitic transformation in 0.18 wt.% C, 0.2 wt.% Si, 0.9 wt.% Mn, 2.9 wt.% Ni, 1.5 wt.% Cr and 0.4 wt.% Mo steel ( $M_s \sim 390^\circ\text{C}$ ) with approximately  $150\ \mu\text{m}$  austenite grain size using confocal laser microscopy. a)  $400^\circ\text{C} \sim 0\%$ , b)  $365^\circ\text{C} \sim 50\%$ , c)  $350^\circ\text{C} \sim 70\%$ , d)  $300^\circ\text{C}$  [Koseki2011]

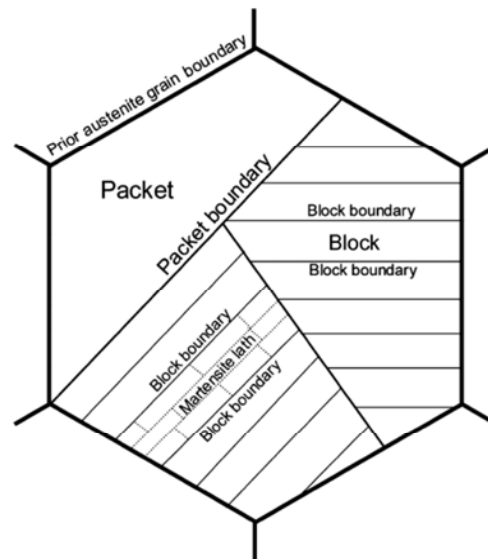


Figure 14: Common designations for the characterization of martensite. The image is taken from Hiromoto Kitahara [Kitahara2006] in reference to the definitions of George Krauss [Krauss1990]

The structures of retained austenite processed by Quenching and Partitioning are located within the sub micrometer scale and are not visible in light microscopy. Investigation of the microstructure of martensitic TRIP steels made by Quenching and Partitioning using electron microscopy reveals the nanometer-sized structures of carbon enriched austenite within the martensitic matrix.

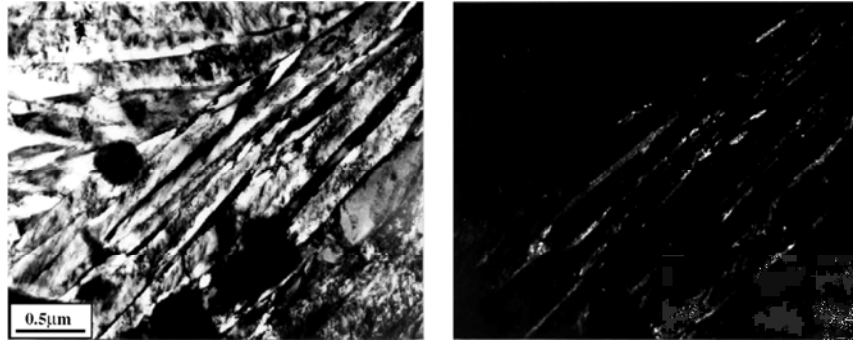


Figure 15: Transmission Electron Microscopy (TEM) image of 0.60 wt.% C, 0.95 wt.% Mn and 1.96 wt.% Si steel quenched to 190 °C and partitioned at 250 °C [Edmonds2006] Bright field (left) and the dark field using (002) austenite reflection

In the case of low partitioning temperatures, cf. figure 15, the retained austenite has a thin foil shape surrounding martensitic lath microstructure. With increasing partitioning temperatures, the foils enlarge and form blocky areas, as shown in figure 16.

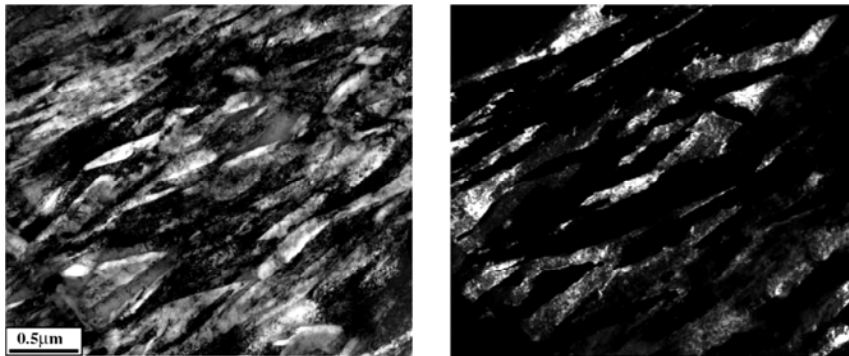


Figure 16: Transmission Electron Microscopy (TEM) image of 0.60 wt.% C, 0.95 wt.% Mn and 1.96 wt.% Si steel quenched to 190 °C and partitioned at 400 °C [Edmonds2006] Bright field (left) and the dark field using (200) austenite reflection

Amy Clarke, née Streicher [Clarke2008], analyzed furthermore the local carbon content of low alloyed steels applied to Quenching and Partitioning heat treatment and found evidence for significant carbon partitioning, cf. figure 17.



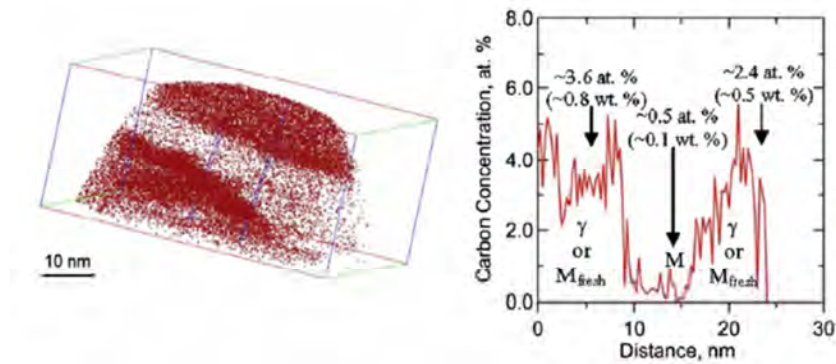


Figure 17: Atom probe tomography of 0.19 wt.% C, 1.59 wt.% Mn, 1.63 wt.% Si and 0.036 wt.% Al steel after intercritical annealing producing approximately 25% intercritical ferrite, quenching to 220 °C for 10 s and partitioning at 400 °C for 10 s [Clarke2008]

Recently, Dorien DeKnijf et al. [DeKnijf2012] were able to show EBSD investigations of microstructures made by Quenching and Partitioning. It is evident from the crystallographic orientations in figure 18 that the block-shaped austenite areas are retained from the prior austenite grains, which are visible by their unique color, respective of its orientation.

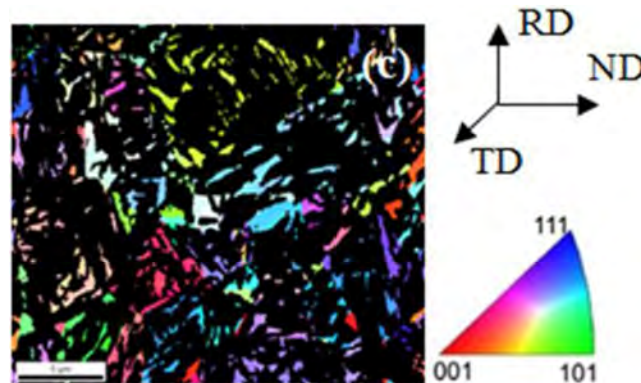


Figure 18: Austenite Inverse Pole Figure (IPF) map of 0.25 wt.% C, 3 wt.% Mn and 1.5 wt.% Si steel after quenching at 244°C and partitioning at 400°C for 1,000 s showing crystallographic dependence of prior austenite grains obtained by Electron Back Scattered Diffraction (EBSD) [DeKnijf2012]

### 3.7. Properties and Application

There are only limited investigations of Quenching and Partitioning with full austenitization available. The available results of tensile tests from various resources are summarized in figure 19 and figure 20.

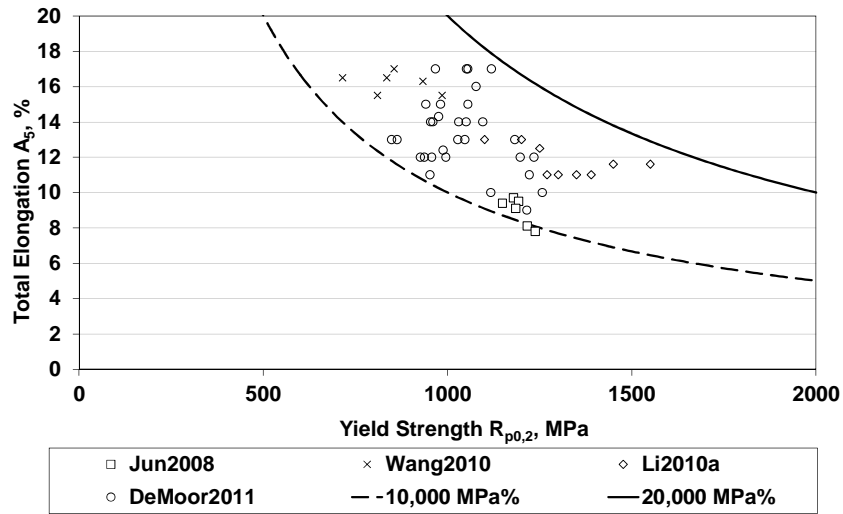


Figure 19: Total elongation vs. yield strength of martensitic TRIP assisted steels made by Quenching and Partitioning after full austenitization [Jun2008] [Wang2010] [Li2010] [DeMoor2011]

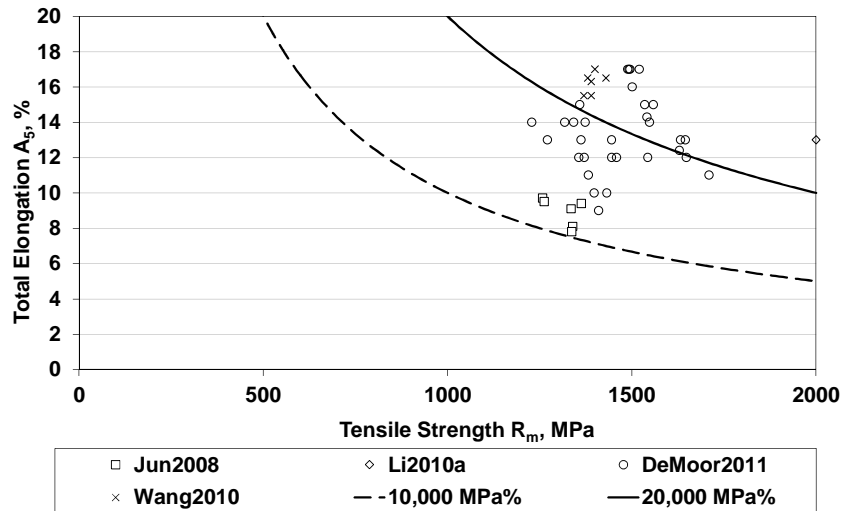


Figure 20: Total elongation vs. tensile strength of martensitic TRIP assisted steels made by Quenching and Partitioning after full austenitization [Jun2008] [Wang2010] [Li2010] [DeMoor2011]

Due to different tensile sample geometries, the total elongation data was corrected to a proportional  $A_5$  sample by D. A. Oliver's formula [Oliver1928], see equation (8), as described in international standards [ISO2566] whereas  $A_x$ ,  $l_{0x}$  and  $S_{0x}$  are the total elongation in percent, the gauge length in mm and the cross section in  $\text{mm}^2$  of the original samples.

$$A_5 = A_x \left( \frac{l_{0x}}{5,65\sqrt{S_{0x}}} \right) \quad (8)$$

High ductility at high tensile strength is the tenor of the investigations on Quenching and Partitioning steels. Compared to competing Quenched and Tempered steels, which satisfy the same strength level, it is remarkable that the yield strength is decreased at the same tensile strength. At the same time uniform elongation, only cited in the studies of C. Y. Wang [Wang2010] and Emmanuel De Moor [DeMoor2011], and strain hardening are increasing in Quenching and Partitioning steels. These properties allow complex forming at high strength levels and for example application in crash components, as they can benefit from the high amount of absorbed energy during deformation.

Beside the tensile test data less information is available for additional technical capabilities. An investigation of E. Paravicini Bagliani et al. [Bagliani2013] on 0,28 wt.% C, 1.4 wt.% Si, 1.5 wt.% Cr, 0.7 wt.% Mn and 0.56 wt.% Mo steel shows enhanced toughness and another study of Ivo Černý et al. [Cerny2011] shows better fatigue test performance on 42SiCrB steel after Quenching and Partitioning compared to their Quenched and Tempered condition. The lack of important properties like corrosion, toughness and fatigue will be disclosed when industrial scale prototype material is finally available.

The concepts to use martensitic TRIP assisted steels made by Quenching and Partitioning are broad and range from bearings, cf. the work of Adam J. Shutts et al. [Shutts2006], to automotive structural parts suggested by John G. Speer [Speer2011], however there are no substantive components derived from these at the present time.

### 3.8. Crystallography

Diffraction experiments using interference of electrons and X-rays with the iron lattice are of particular relevance for this study, as the atomic structure is directly related to its corresponding macroscopic properties. The crystallographic information given is used in X-ray diffraction, Transmission Electron Microscopy and in dilatometry.

The crystal structure of pure iron is allotropic, i.e. depending on pressure and temperature five different crystallographic modifications, designated with the Greek letters  $\alpha$ ,  $\beta$ ,  $\gamma$ ,  $\delta$  and  $\epsilon$  exist. In the present study, the  $\alpha$ - and  $\gamma$ -iron modifications, also known as ferrite and austenite, are of interest and are described in detail, see figure 21. Moreover the distorted crystallographic structure of the  $\alpha$ -iron called martensite, which is designated by  $\alpha'$  and formed by the diffusionless athermal  $\gamma$  to  $\alpha'$  transformation during rapid quenching, is elucidated. Furthermore, the corresponding sublattice void accommodating carbon atoms are taken into account. It should be mentioned, in the case of the 42SiCrB steel one carbon atom per 50 iron atoms is present in the interstitial sublattice, because 0.42 wt.% C is almost equal 2 at.% C. For the three-dimensional visualization of crystal data VESTA Software package, cf. [Momma2011], is used.

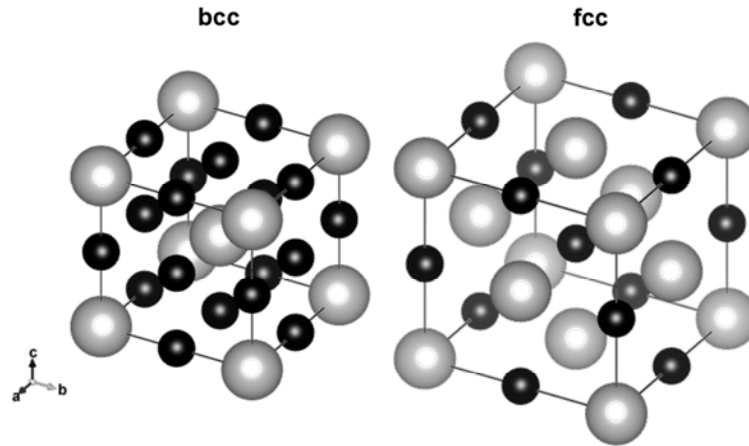


Figure 21: Relevant crystallographic structures of iron-carbon system. Grey spheres represent iron atoms and possible octahedral sublattice voids potentially occupied by carbon atoms are illustrated as black spheres. The size of the unit cell is drawn to scale, unrealistic atom sizes are chosen for better illustration

Ferrite, also designated as  $\alpha$ -iron, has a body-centered cubic (bcc) crystal structure. The Hermann–Mauguin notation is “Im3m” and the space group number is 229. Crystal structure and the lattice parameter of 0.28665 nm were identified with X-ray diffraction experiments by Ralph W. G. Wyckoff [Wyckoff1963]. The neutron diffraction experiments by Marcel Onink et al. [Onink1993] also investigated the influence of the temperature on the lattice parameter, as shown in equation (9):

$$a_{\alpha}(T) = 0.28863 \cdot \{1 + 17.5 \cdot 10^{-6} [T - 800]\} \quad (9)$$

The microscopic interstitial voids in ferrite limit the solubility of carbon in ferrite. Even if the symmetric tetrahedral voids are increased by means of geometrical considerations, carbon prefers the energetically favorable asymmetric octahedral sublattice sites causing distortion in  $\langle 100 \rangle$  directions. Due to the low solubility, the crystal appears altogether as cubic; cf. the work of George Krauss [Krauss1990], Nicholas Hatcher et al. [Hatcher2012] and Jae Hoon Jang et al. [Jang2013].

Austenite, commonly designated as  $\gamma$ -iron, has a face-centered cubic (fcc) crystal structure. The space group number is 225 and the Hermann-Mauguin notation is “Fm3m”. The lattice parameter 0.3591 nm was also determined by Ralph W. G. Wyckoff [Wyckoff1963] and is listed in the American Mineralogist Crystal Structure Database [Downs2003]. The sublattice places, which are usually occupied by carbon atoms, contain the octahedral interstitial voids. This is of particular relevance for the martensitic transformation, because trapped carbon in this position leads to the tetragonal distortion in martensite.

Ichiro Seki and Kazuhiro Nagata [Sekiz005] measured the influence of the carbon content and the temperature on the lattice parameter using high temperature cobalt X-ray diffraction of pure iron above  $A_{c3}$  temperature and developed the following equation (10) where T is temperature in K and C is carbon concentration in weight percent.

$$a_0 = 0.35519 + 8.1593 \cdot 10^{-6} T + 1.7341 \cdot 10^{-3} C \quad (10)$$

Marcel Onink et al. [Onink1993] cited the temperature dependence of the lattice parameter of austenite and the impact of solute carbon as well, cf. equation (11)

$$a_\gamma(x_C, T) = (0.36306 + 0.00078x_C) \cdot \{1 + (24.9 - 0.5x_C) \cdot 10^{-6} [T - 1000]\} \quad (11)$$

The conclusions made by Ichiro Seki and Kazuhiro Nagata show independent effect of carbon and temperature on the lattice parameter, as it is expected by physics of solid solutions, and is hence, more probable and used in this study. In general, the impact of carbon on the lattice parameter of 0.0017 in equation (10) is significantly smaller than the temperature dependent factor of approximately 0.004 in equation (11). The temperature dependence is nearly the same in both investigations.

Martensite, also designated as  $\alpha'$ -iron, in as quenched condition has a body-centered tetragonal (bct) crystal structure, because carbon is trapped in octahedral sublattice voids on the c-axis, as explained in figure 22. The space group number is 139 and the Hermann-Mauguin symbol is “I4/mmm”. The tetragonal distortion is increasing with carbon content. For the carbon content of 0.42 wt.%, given in this investigation, the a lattice parameter is given by [Honda1932] to 0.286 nm and c lattice parameter to 0.291 nm.

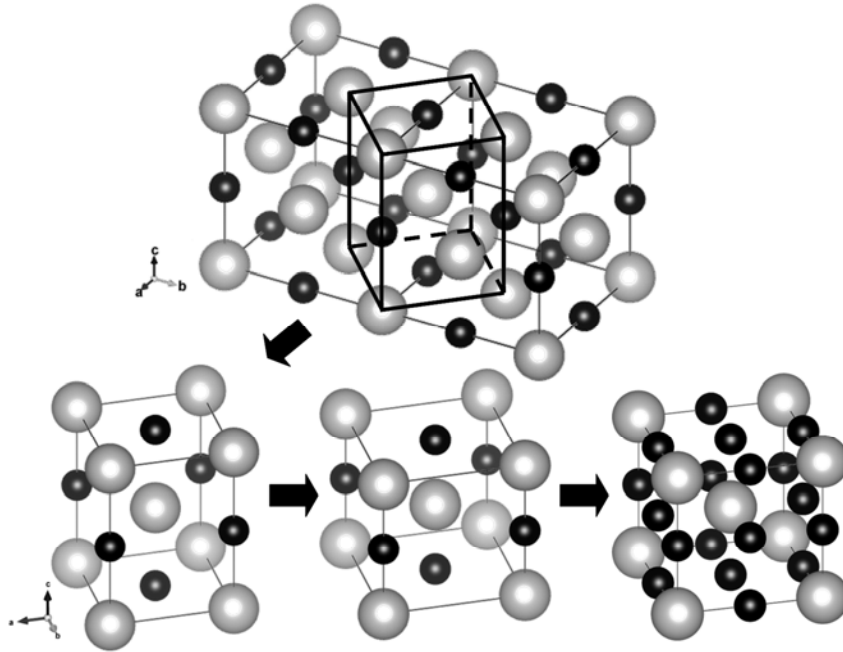


Figure 22: Bain Transformation from Austenite to tetragonal and subsequent cubic martensite schematically. Iron atoms (gray) and octahedral sublattice voids (black) usually occupied by carbon atoms explaining the tetragonal structure of martensite after quenching

The tetragonal structure is lost if carbon diffusion occurs, e.g. during tempering, due to likely random carbon distribution in the sublattice. The resulting structure is labelled “cubic martensite”. Due to the cubic structure, martensite is often treated as

ferrite, even if the lattice parameter is slightly enlarged and additional lattice defects like dislocations, stacking faults or internal twins due to the shear compensation are present. These simplifications are done with regard to diffraction experiments.

Furthermore, Kôtarô Honda and Zenji Nishiyama [Honda1932] observed that the martensite lattice parameters are dependent on the carbon content as well, since it is possible to dissolve carbon as interstitials. Their diffraction measurements show 0.12 % higher lattice parameter of 0.4 wt.% C martensite compared to carbon free martensite. Shrinking of the martensite lattice during tempering is also observed as carbon diminishes.

Cementite, sometimes also designated as  $\theta$ -Carbide, is the most important iron carbide used in the formation of low alloyed steels. Cementite has an orthorhombic crystal structure, space group number 62, Hermann-Mauguin symbol "Pnma" and its stoichiometry is  $\text{Fe}_3\text{C}$ . Cementite is orthorhombic, with lattice parameters  $a=0.452$  nm,  $b=0.509$  nm, and  $c=0.674$  nm [Krauss1990].

## 4. Experimental

The material and the process of Quenching and Partitioning are described in this section. Furthermore, the concept of heat treatments, the used experimental program and the scientific methods to analyze experimental data of dilatometric and diffraction experiments are described in detail.

The experiments are divided into three parts: The dilatometric analysis, the in-situ X-ray diffraction and finally the application of Quenching and Partitioning heat treatment with investigation of the resulting mechanical properties.

Two variants are considered in the experiments: One-step at which the partitioning temperature is equal to the quenching temperature and two-step with increased partitioning temperature. One-step is easier to realize and is therefore of economic interest, though some research suggests better results by two-step experiments, cf. chapter 3.7.

### 4.1. Material

42SiCrB steel is used in this study. Material's chemical analysis, determined by spark atomic emission spectroscopy with a Belec Vario Lab device, is given in table 1, where non-specified impurities are neglected. The material is a medium carbon low alloyed steel with 2 wt.% silicon and 1.3 wt.% of chromium. Additionally, small amounts of niobium and boron are used as micro alloying elements. Niobium ensures small austenite grain size by precipitation of niobium-carbonitrides Nb(C,N) and the Boron is enhancing the hardenability, cf. relevant literature, e.g. [Lyakishev1984] [Werner1990] [Gupta1994]. The nitrogen content is usual for steel production without vacuum degassing technologies. This kind of chemical composition is usually used as spring steel, e.g. for automotive suspension.

Table 1: Chemical Composition of 42SiCrB steel in wt.%

C	Si	Mn	Cr	Al	Nb	N	B
0.43	2.0	0.59	1.3	0.008	0.035	0.0076	0.0025

The composition is currently produced on a large scale production. The steel is molten in an electric arc furnace and continuously casted to billets. Charles White summed up literature on the "amount of hot reduction required to achieve the transition from cast to wrought structure and properties" [White1998] and found literature values between 3:1 and 7:1. Accordingly blocks are forged manually with a minimum true strain of  $\varphi=2$  (7:1) to a plate with a final thickness of 30 mm. This ensures that the as cast dendritic microstructure is replaced by fine grained austenite. The material is used in the forged condition. Homogenization annealing to avoid any segregation related effects is deliberately not applied to keep the experimental results applicable to industrial heat treatment processes. The samples are taken in longitudinal direction, the exact positions are shown in figure 23.

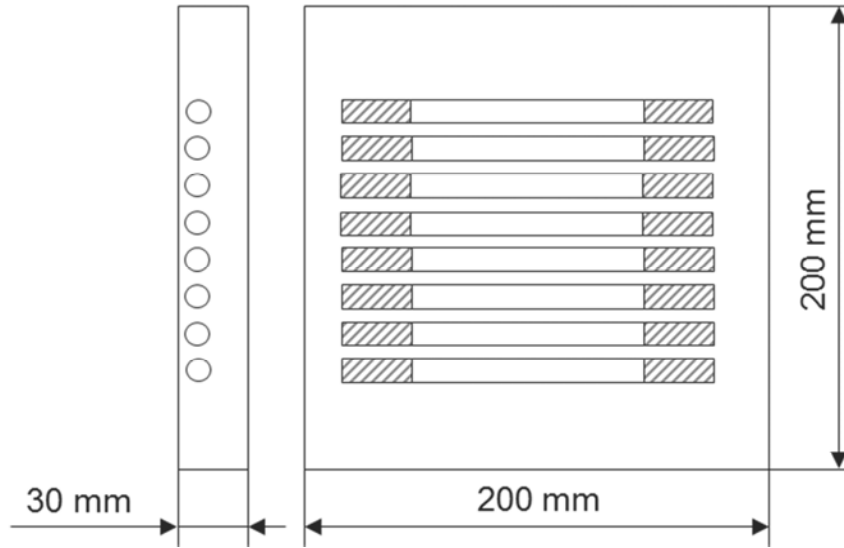


Figure 23: Design of the forged plates and positions of the samples

#### 4.2. Phase Transformation Diagrams

The Continuous Cooling Transformation and the Isothermal Time Temperature Transformation Diagrams of  $42\text{SiCrB}$  steel are investigated to analyze the material behavior in general. The experiments to establish CCT diagram are carried out on LINSEIS RITA L78 quenching dilatometer. Full rod Samples of 3 mm diameter and 10 mm length are used in this case. All samples are turned from the forged material. To characterize the phase transformation behavior of  $42\text{SiCrB}$  steel after full austenitization at 950 C for 300 s the samples are cooled continuously with different cooling rates:  $20 \text{ Ks}^{-1}$ ,  $10 \text{ Ks}^{-1}$ ,  $4 \text{ Ks}^{-1}$ ,  $2 \text{ Ks}^{-1}$ ,  $1 \text{ Ks}^{-1}$  and  $0.5 \text{ Ks}^{-1}$ .

During continuous heating with  $10 \text{ Ks}^{-1}$  the ferrite to austenite phase transformation temperatures  $A_{c1}$  and  $A_{c3}$  and during continuous cooling the austenite to ferrite  $A_{r3}$  and  $A_{r1}$ , austenite to bainite start  $B_s$  and austenite to martensite start  $M_s$  and finish  $M_f$  phase transformation temperatures are determined from physical data, respectively change in length, at 1 % of phase transformation according to standard SEP1681 [SEP1681]. The change in length  $\Delta l$  as a function of the change in temperature  $\Delta T$  is well described by the linear approximation in equation (12) by the initial length  $l_0$  and the thermal expansion  $\alpha$ .

$$\Delta l \approx l_0 \alpha \Delta T \quad (12)$$

The phase fraction of austenite  $V^Y$  is calculated by linear combination of ferrite and austenite expansion, also known as lever rule, which is acceptable if isotropic material behavior is assumed.

$$V^Y(T) = \frac{\Delta l(T) \left( \alpha_Y T l_0 + c_Y \right)}{\left( \alpha_\alpha T l_0 + c_\alpha \right) \left( \alpha_Y T l_0 + c_Y \right)} \quad (13)$$



Thermal expansion coefficients for austenite  $\alpha_\gamma$  and ferrite  $\alpha_\alpha$  and the corresponding intercepts  $c_\gamma$  and  $c_\alpha$  are determined from each experiment in a range of interest 25 K to 75 K above or below the transformation by least squares fit. This requires a complete phase transformation, i.e. all austenite decomposes during cooling.

The microstructure is characterized by light microscopy using Nital etchant and finally, hardness is tested on STRUERS DURAMIN Micro Hardness indenter in Vickers mode with a load of 9.81 N, i.e. "HV 1", according to ISO 6507 standard [ISO6507]. The hardness is always averaged from three indents.

To analyze the isothermal phase transformation quenching to isothermal holding temperature is carried out at  $100 \text{ Ks}^{-1}$  to accurately measure short transformation start times after full austenitization at  $950 \text{ °C}$  for 300 s. In the beginning of the isothermal section the steady state situation between constant gas cooling and fast high frequency induction heating is avoided by turning off the gas as fast as possible. Otherwise, temperature gradients within the samples cause serious artificial changes in length.

To characterize the steel of this study a wide isothermal temperature range from  $300 \text{ °C}$  to  $750 \text{ °C}$  with step size of 50 K is used. The temperature is kept as long as no change in length is observed, although the experiment is stopped after 10,000 s.

In the case of isothermal phase transformation, the change in length is directly proportional to the degree of phase transformation, as described by Eric Mittemeijer [Mittemeijer1992]. The phase fraction of ferrite or bainite  $V^\alpha$  transformed at any instant  $t$  is defined by the current length  $\Delta l$  in relation to the length at start  $\Delta l_{(\text{begin})}$  and end  $\Delta l_{(\text{end})}$ , cf. equation (14).

$$V^\alpha(t) = \frac{\Delta l(t) - \Delta l_{(\text{begin})}}{\Delta l_{(\text{end})} - \Delta l_{(\text{begin})}} \quad (14)$$

### 4.3. Dilatometric Study of Quenching and Partitioning

All dilatometric experiments, excluding the ones for the continuous cooling transformation (CCT) diagram, are carried out on BÄHR DIL805 A/D Deformation and Quenching Dilatometer using inductive heating and nitrogen inert gas for cooling. BÄHR standard hollow samples for inner cooling with 4 mm outer diameter, 2 mm inner diameter and 10 mm length are used. The sampling rate is 1,000 measurements per heat treatment segment and always higher than  $1 \text{ s}^{-1}$ . For long time experiments, i.e. segments with more than 1,000 s, the sampling rate varies logarithmically from  $100 \text{ s}^{-1}$  to  $0.1 \text{ s}^{-1}$ .

Austenitization of all samples in this study is accomplished by continuous heating at the rate of  $10 \text{ Ks}^{-1}$  and holding at  $950 \text{ °C}$  for 300 s in order to dissolve all carbides and to create a homogeneous carbon distribution in austenite. Furthermore, the quenching rate after austenitization is set to  $40 \text{ Ks}^{-1}$ , if not designated otherwise, e.g. in the TTT experiments where faster cooling is necessary. This reduces the number of variables and ensures good comparability to the sample continuously quenched to room temperature used for the determination of the Koistinen-Marburger parameters.

### 4.3.1. Heat Treatment

To select reasonable temperatures for the dilatometric study of Quenching and Partitioning the Constrained Carbon Equilibrium Model is used. The parameters for the Koistinen-Marburger equation, cf. equation (3), are measured by means of dilatometry. The martensite start temperature and the coefficient  $\alpha$  are determined by least squares fit method. As the Koistinen-Marburger equation suits the martensitic transformation of  $42\text{SiCrB}$  steel after full austenitization and quenching at the rate of  $40\text{ Ks}^{-1}$ , the extended description, see chapter 3.4, is not needed here.

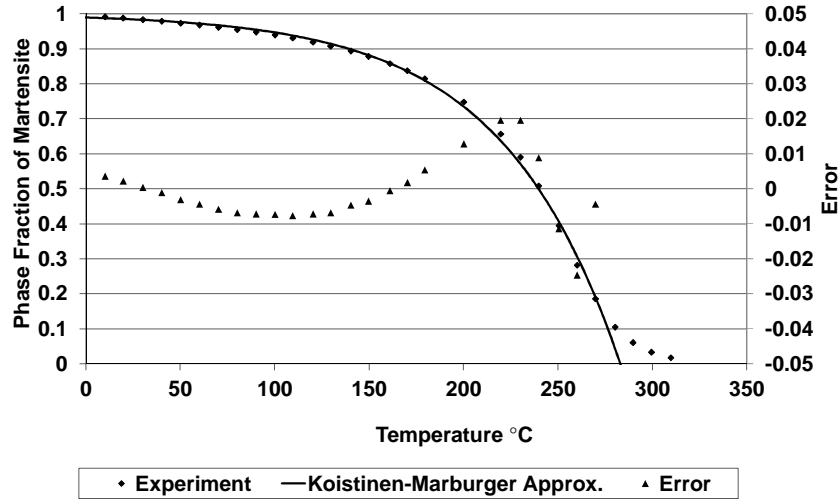


Figure 24: Modified Koistinen-Marburger Approximation for  $42\text{SiCrB}$  steel determined from dilatometric data and least squares fit

The experimental data, the approximation and the resulting errors are shown in figure 24 with the resulting parameters listed in table 2. The overall error in this case is below 5 % and smaller than 2 % in the region of interest, i.e. in the martensite rich corner below 250 C.

Table 2: Parameters to describe the martensitic transformation by the Koistinen-Marburger equation, derived by least squares fit

Coefficient	Value
A	0.016
Martensite start Temperature $M_s$	283 °C

The shark fin model for  $42\text{SiCrB}$  steel, plotted in figure 25, is derived using the coefficients of table 2 and the equations of chapter 3.4. As already suggested, cf. chapter 3.1, low amounts of retained austenite do not contribute significantly to Transformation Induced Plasticity. Hence, the experiments characterizing the mechanical properties mainly focus on quenching temperatures above 150 °C to stabilize at least 10 % of carbon enriched austenite. Moreover, the maximum quenching temperature is limited to 210 °C, corresponds to austenite phase fraction of 0.3, to guarantee that no fresh high carbon martensite forms during final cooling to room temperature, what is expected to start at 225 °C.

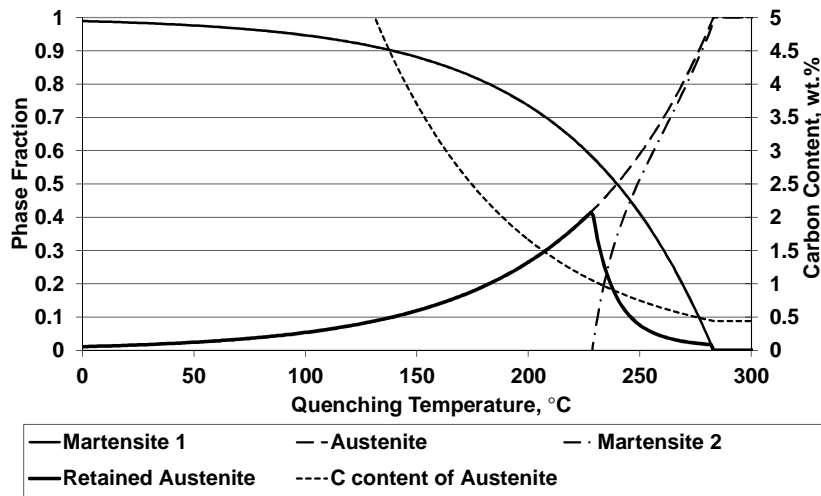


Figure 25: Constrained Carbon Equilibrium model of 42SiCrB steel

#### 4.3.2. One-step Quenching and Partitioning

During the dilatometric investigations with regard to one-step Quenching and Partitioning only two parameters are varied systematically: the quenching temperature and the partitioning time.

First, dilatometric one-step Quenching and Partitioning experiments vary the quenching temperature systematically from 125 °C up to 275 °C while the partitioning time is limited to a technically viable, constant time span of 1,000 s, before the samples are quenched to room temperature. The temperatures should stabilize austenite phase fractions up to 0.4 according to the shark fin model described in the preceding chapter.

In the second part of one-step Quenching and Partitioning experiments the partitioning time is varied systematically from 100 s to 30,000 s at constant quenching temperature of 200 °C.

Finally, to understand the mechanisms contributing, additional experiments are performed with different quenching temperatures. The policy of the isothermal segment of the TTT diagram experiments, described previously, is applied to the partitioning time.

#### 4.3.3. Two-step Quenching and Partitioning

During two-step Quenching and Partitioning, two additional parameters become part of the equation: the quenching time and the partitioning temperature. As it is pointless to design full factorial experiments, because of the immoderate effort, smart restrictions are necessary. Since the isothermal behavior throughout the quenching phase is already investigated by the one-step experiments, ideal short and stable quenching is aspired. Therefore, cooling to quenching temperature and reheating to partitioning temperature are carried out at high speed of 100 Ks<sup>-1</sup> to remove time dependence to the most without losing the control. To guarantee the stable and accurate quenching temperature the quenching time is set to 20 s. Preliminary experiments to adjust the temperature regulation parameters showed that 20 seconds

are necessary to reach the quenching temperature without dropping below the set temperature.

#### 4.3.4. Tempering of Martensite

As the tempering of the martensite matrix is affecting the dilatometric experiments during partitioning, the influence on the change in length is measured as well. Therefore, a hardened sample, that was quenched to room temperature, of  $42\text{SiCrB}$  steel is applied to slow heating with  $1\text{ Ks}^{-1}$  up to  $600\text{ }^\circ\text{C}$ , simulating different tempering temperatures. This is not as accurate as measuring the change in length during several isothermal experiments, but experiments by Eduard Houdremont [Houdremont1956] show that all effects during tempering of martensite are observed with only one experiment.

#### 4.4. In-situ X-Ray Diffraction

To overcome the lack of superimposed effects during dilatometric investigations and the characterization of mechanisms, in-situ X-ray diffraction experiments are carried out during one- and two-step Quenching and Partitioning and Quenching and Tempering heat treatments for comparison.

Synchrotron X-ray transmission experiments in Debye-Scherrer [Debye1916] geometry and fast-in-situ X-ray reflection, respectively Bragg-Brentano theta-theta geometry, experiments are used to investigate the change of lattice parameters and phase fractions during isothermal partitioning.

Two X-ray sources with different provided energies, i.e. wavelengths, are used to analyze the present phases and their properties within the steel samples:

- SEIFERT SUN XRD fast in-situ X-ray diffractometer with cobalt radiation and
- PETRA III synchrotron source in Hamburg, Germany.

According to Planck's relation, cf. equation (15), corresponding wave lengths are calculated in table 3. A value of  $1.23984193\text{ keV/nm}$  is used for Planck's constant multiplied with the speed of light. The wavelength of copper and cobalt radiation is taken from table 2.3 in the standard work of Lothar Spieß et. al. [Spieß2009].

$$E = \frac{hc}{\lambda} \quad (15)$$

Table 3: Overview of x-radiation, photon energy and wavelength

Source	Energy	Wavelength
Copper anode	8.05 keV	0.15406 nm
Cobalt anode	6.93 keV	0.17903 nm
PETRA III	100.00 keV	0.0124 nm

Accuracy and precision of in-situ experiments are always limited, as the dwell time has to be small enough to describe the changes over time and as high as possible to obtain very accurate and precise results. Assuming, that an accuracy of  $0.001\text{ nm}$  in

the lattice parameter is quite possible if the diffraction intensities are distinct, what is, by the way, inadequate for X-ray diffraction experiments, only drastic changes of approximately 0.6 wt.% in the carbon content of the austenite would be traceable. The expected changes in the martensite lattice of 0.00034 nm, cf. chapter 7.1, would still be invisible in this case. As the precision of X-ray diffraction experiments is usually orders of magnitude higher than the accuracy, there are still good chances to observe small changes qualitatively.

#### 4.4.1. PETRA III Synchrotron

In-situ experiments are carried out at the PETRA III, High Energy Materials Science Beamline Po7 of Helmholtz-Zentrum Geesthacht (HZG), Hamburg, Germany [Schell2014]. The 16 inch image plate detector Perkin Elmer XRD 1622 Flat Panel with 2048 x 2048 pixels is used to analyze cubic face-centered austenite and cubic body-centered ferrite and martensite at 1919 mm sample to detector distance and 100 keV photon energy. The sampling and dwell time is set to 3 s. As the High Energy Materials Science Beamline is equipped with a special BÄHR DIL805 A Quenching Dilatometer, already prepared for transmission XRD<sup>2</sup> experiments, BÄHR standard hollow cylindrical samples with 4 mm outer and 2 mm inner diameter are used as in the other dilatometric experiments. A LaB6 powder reference sample is used to calibrate the measurement before the in-situ test and afterwards to exclude the systematic measurement error. The Fit2D software integrates the 2D-images over 360° to 2 $\theta$  scans and during the integration polarization correction is applied, please refer to the publications of Andy Hammersley and Bob He [Hammersley1989] [Hammersley1997][He2003][He2009] for further information.

The synchrotron in-situ X-ray diffraction experiments are performed with the kind assistance of Assistant Prof. Dipl.-Ing. Dr. techn. Guillermo Carlos Requena and his team at the Institute of Materials Science and Technology, TU Wien.

#### 4.4.2. Fast in-situ X-Ray Diffraction

The SEIFERT SUN XRD equipped with three METEOR1D detectors allows simultaneous measurement of 48° - 96° 2 $\theta$  angle sector at 0,02° step size and attractive rate of one scan per second. To achieve reasonable signal to noise ratio together with high resolution the data of ten recordings must be accumulated. Accordingly, the used sampling interval is 10 s. The cobalt anode is operated with 40 kV voltage and 45 mA current with an iron filter. The Bragg-Brentano theta-theta geometry is characterized by the goniometer radius of 250 mm.

To apply the designated heat treatment to the samples, a fast heat treatment chamber of DESETEC THIN FILM ENGINEERING AND TECHNOLOGY is used. The chamber is equipped with fused silica radiation heating devices of 3.5 kW and inert gas nitrogen cooling. The sample holder made from carbon fiber carbon composite ensures a stable sample position during the heat treatment. A type K thermocouple of 0.5 mm thickness is welded on the sample surface to control the temperature. Squared samples with an edge length of 11 mm and 1 mm thickness are used.

During the austenitization phase within fast-in-situ experiments using Cobalt radiation, peak splitting because of  $K_{\alpha 1}$  (6.93 keV, 0.17889 nm) and  $K_{\alpha 2}$  (6.92 keV, 0.17928 nm) radiation is observed as an additional peak of half integrated intensity right beside all appearances. To take the both intensities into account, a mean

wavelength of 0.17903 nm [Spieß2009] is used for the calculation of phase fractions by reference intensities, and accordingly the integrated intensities of both peaks are determined by only one Voigtian peak.

Fast in-situ X-ray diffraction experiments are performed with kind assistance of Prof. Dr. rer. nat. Gerhard Schneider, his team from Materials Research Institute of Aalen University and Dr. Dieter Schmid from DeSeTec.

#### 4.4.3. Lattice Parameter and Austenite Carbon Content

Sir William Lawrence Bragg and his father, Sir William Henry Bragg established the science of crystallography with their famous Bragg's Law, cf. equation (16). It describes the relationship between lattice plane spacing  $d_{(hkl)}$  and the experimental parameters wavelength  $\lambda$  and the diffraction angle  $\theta$  in diffraction experiments. [Bragg1915]

$$d_{(hkl)} = \frac{\lambda}{2\sin(\theta_{(hkl)})} \quad (16)$$

From the lattice plane spacing, the corresponding lattice parameter in cubic crystal structures can be easily derived by the following expression (17):

$$a = d_{(hkl)} \cdot \sqrt{h^2 + k^2 + l^2} \quad (17)$$

The equation (10) of Ichiro Seki and Kazuhiro Nagata [Sekiz005], cf. chapter 3.8, is used to calculate the austenite carbon content from the obtained lattice parameter. Within the equation no information is given on the influence of the substitutional elements and their effect on the lattice parameter is assumed to be constant. This allows us to use offset correction making the carbon content of austenite matching the nominal carbon content in the end of the austenitization process.

Equation (9) is used to compensate the influence of temperature on the lattice parameter of martensite. As the ferrite coefficient of expansion is unsuitable to martensite,  $13.5 \cdot 10^{-6} \text{ K}^{-1}$  is used in this case of 42SiCrB steel instead.

#### 4.4.4. Determination of Retained Austenite Phase Fraction

The reference intensity ratio (RIR) method, based on American Society for Testing and Materials standard E975 [ASTM-E975], is used to determine the retained austenite volume fraction. It is obtained from the measured integrated  $I_{\gamma(200)}$ ,  $I_{\gamma(220)}$  austenite and  $I_{\alpha(200)}$ ,  $I_{\alpha(211)}$  ferrite intensities and corresponding reference intensity ratios ( $R_{\gamma(200)}$ ,  $R_{\gamma(220)}$ ,  $R_{\alpha(200)}$ ,  $R_{\alpha(211)}$ ) by equation (18).

$$V^{\gamma} = \frac{\left( \frac{I_{\gamma(200)}}{R_{\gamma(200)}} + \frac{I_{\gamma(220)}}{R_{\gamma(220)}} \right)}{\left( \frac{I_{\gamma(200)}}{R_{\gamma(200)}} + \frac{I_{\gamma(220)}}{R_{\gamma(220)}} \right) + \left( \frac{I_{\alpha(200)}}{R_{\alpha(200)}} + \frac{I_{\alpha(211)}}{R_{\alpha(211)}} \right)} \quad (18)$$

The Integrated intensities, respectively the area of every considered peak, and the peak positions are determined from the experimental data using the Voigtian peak profiles and linear background functions with least squares fit method.

The integrated reference intensity values  $R_{i(hkl)}$  are calculated from the theoretical integrated intensities divided by the squared volume of the corresponding unit cell  $V_i$ . According to equation (19), the integrated intensity is dependent on the number of equivalent crystallographic planes within the unit cell  $m_{i(hkl)}$ , the structural factor  $F_{i(hkl)}$  and the experimental setup, represented by the Lorentz- and Polarization factors  $L$  and  $P$ . Because the RIR method merely uses ratios of intensities all constant parameters can be neglected and the values are given in arbitrary units.

$$R_{i(hkl)} = m_{i(hkl)} \frac{|F_{i(hkl)}|^2}{V_i^2} LP \quad (19)$$

The absolute value of the Structure factor  $|F_{i(hkl)}|$  is written in a simplified version as well in equation (20). This is possible if only one type of atoms is present in the sample, as it is valid for the determination of retained austenite in low alloyed steels.

$$|F_{i(hkl)}| = |f_0 + f' + f'' + f_T * K| \quad (20)$$

The atom factor  $f_0$  is calculated from Cromer-Mann coefficients, see table 4, taken from International tables for X-ray crystallography [IUCr1968], by equation (21).

$$f_0 = c + \sum_1^4 a_i e^{b_i \sin^2\left(\frac{\theta}{\lambda}\right)} \quad (21)$$

Table 4: Cromer-Mann coefficients for iron from [IUCr1968]

a1	a2	a3	a4	c	b1	b2	b3	b4
11.7695	7.3573	3.5222	2.3045	1.0369	4.7611	0.3072	15.3535	76.8805

The anomalous scattering factors  $f' = -1.1$  and  $f'' = 3.3$  for iron atoms and copper x-radiation are taken from “International tables for X-ray crystallography” [IUCr1968] and the values  $f' = -3.3$  and  $f'' = 0.48$  for cobalt x-radiation are taken from “X-Ray Form Factor, Attenuation and Scattering Tables” [Chantler1995][Chantler2005]. Anomalous scattering is neglected for synchrotron sources as the influence at high energies decreases.

The temperature factor  $f_T$  is dependent on the Debye parameter  $B$ , Bragg angle  $\Theta$  and wavelength  $\lambda$  with

$$f_T = e^{-B \frac{\sin^2 \theta}{\lambda^2}} \quad (22)$$

The Debye parameter  $B$  is dependent on the Debye Temperature of the Material, which lies between 355 and 467 K for iron.  $B$  equals, to a wide range, values of 0.29 to 0.5 according to the “International tables for X-ray crystallography” [IUCr1968]. New research determined the Debye temperature of iron to be  $428 \pm 9$  K [Pickardt2003].

Hence, the Debye parameter B is calculated to be 0.35 in good agreement to the value of 0.355 used by the American Society for Testing and Materials [ASTM-E975].

The absolute value of  $|K|$  considers systematic extinctions caused from the lattice structure. Every basis atom  $j$  of a unit cell is represented by the scalars  $x_j$ ,  $y_j$  and  $z_j$ , respectively the basis vector, and its extinction behavior is analyzed in equation (23) for each family of  $(hkl)$  planes. The number of basis atoms  $N$  per unit cell is 2 for ferrite (bcc) and 4 in austenite (fcc) structure.

$$|K_{hkl}| = \sqrt{\sum_j^N \cos^2(2\pi(hx_j + ky_j + lz_j)) + \sum_j^N \sin^2(2\pi(hx_j + ky_j + lz_j))} \quad (23)$$

The Unit cell volumes  $V_i$  are derived from the lattice parameters of the phases  $i$ , respectively for ferrite and austenite, given in chapter 3.8 Crystallography.

$L$  represents the Lorentz factor of the Debye-Scherrer geometry [Debye1916], as it is used in all X-ray diffraction experiments. For the Lorentz factor at least four different formulas are given in specialist literature, e.g. [Spiess2009] [He2009], but all result in the same values, Hence, the briefest version is given in equation (24) only.

$$L(\theta) = \frac{\cos \theta}{\sin^2(2\theta)} \quad (24)$$

The polarization of the conventional 1D detector experiments is considered by the polarization factor  $P$ , calculated by equation (25) with  $p=0.5$ , respectively non polarized radiation, because no monochromator is used in these experiments.

$$P(\theta, p) = 1 - p + p \cdot \cos^2(2\theta) \quad (25)$$

The polarization effect in 2D detector synchrotron experiments has been considered and corrected during the integration with Fit2D [Hammersley1997] by a  $p$  value of 0.99. Hence, the polarization factor  $P$  becomes 1 ( $p=0$ ) for the reference intensity calculation.

The American Society for Testing and Materials standard E975 [ASTM-E975] does not suggest copper, cobalt or any type of synchrotron x-radiation and provides no reliable corresponding reference intensity ratios that are available elsewhere and are summarized in table 5. The detailed information can be found in appendix A.

The accuracy of phase fractions determined by reference intensity ratio method is given with a total error of 0.01-0.02 and with a lower detection limit of 0.02. [Spieß2009][ASTM-E975]



Table 5: Summary of the reference intensity ratios used

Source	E	$R_{\alpha(110)}$	$R_{\alpha(200)}$	$R_{\alpha(211)}$	$R_{\gamma(111)}$	$R_{\gamma(200)}$	$R_{\gamma(220)}$
Copper	8.05 keV	1	0.14	0.25	0.74	0.34	0.18
Cobalt	6.92 keV	1	0.13	0.27	0.74	0.33	0.17
Petra III	100 keV	1	0.16	0.31	0.73	0.35	0.22

#### 4.5. Tensile Testing

As a matter of fact mechanical properties of martensitic TRIP assisted steels are highly important to determine they are worth further development. Therefore, an experimental setup for the application of the quite challenging Quenching and Partitioning heat treatment is developed. To realize mechanical testing, the samples should possess a reasonable size. On the one hand, the samples should be big enough to ensure reliable testing results and on the other hand small enough to ensure homogeneous heat treatment within the entire sample. The rod with 9 mm diameter and 160 mm length, shown in figure 26 a), is the optimum sample dimension found for this study.

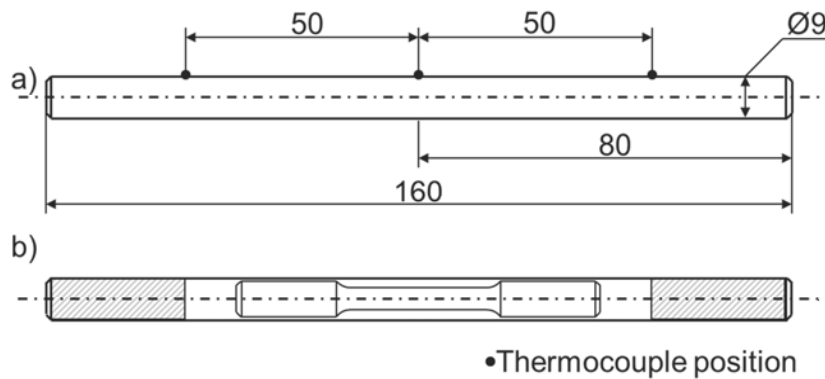


Figure 26: Drawings of a) sample for inductive heat treatment, black dots represent thermocouple measuring points and b) the position of final tensile test samples within the rod

In addition, an appropriate heat treatment concept is necessary to perform the complex Quenching and Partitioning heat treatment. For austenitization and partitioning under controlled conditions, an inductive heat treatment system is used. As temperature gradients are usual over the coil length, the temperatures at the tensile sample are monitored using three thermocouples, one in the middle of the rod and one on each side at a distance of 50 mm from the middle point. According to the experiment shown in figure 27, the maximum variation in the austenitization temperature in the sampling length amounts to 50 °K while the maximum difference during partitioning at 400 °C is only 25 K. Quenching is performed in a salt bath adjusted to the desired temperatures; such that the temperature gradient is minimized.

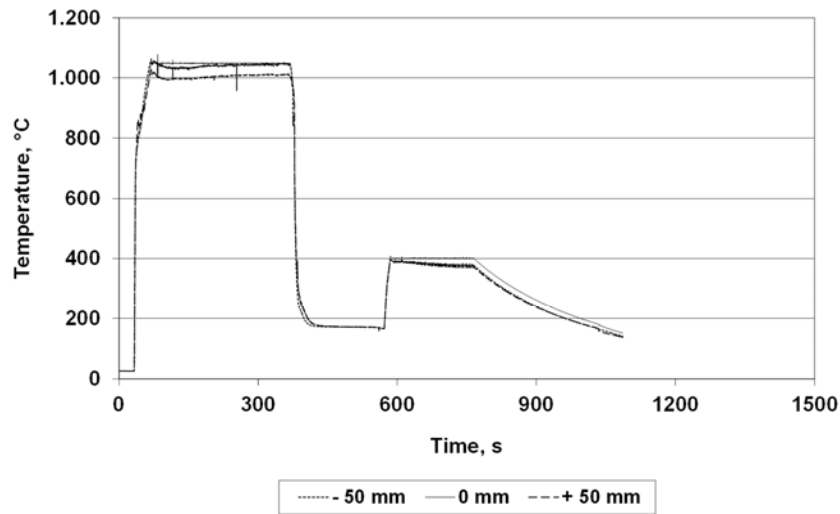


Figure 27: Experimental setup ensuring temperature gradients below 50 °C during austenitization and below 25 °C during partitioning within the sampling region

A servo-hydraulic INOVA TESTING SYSTEMS testing machine by with force capacity of 200 kN is used for tensile testing. The proportional sample geometry with 5 mm diameter and 25 mm gauge length is presented in figure 28. All tensile tests are performed at ambient temperature and according to international standard 6892, cf. [ISO6892]. The elongation is monitored with 25 mm clip-on extensometer until the sample fails.

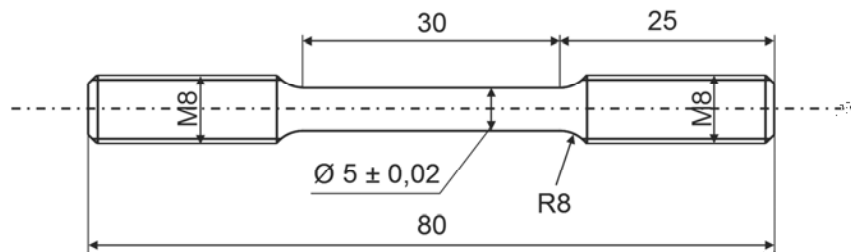


Figure 28: Proportional sample geometry with 5 mm diameter for tensile testing according to international standards

In rare cases, necking and failure of the samples occur outside the gauge length creating a sudden stop of the extensometer strain data in the stress-strain curves. In general, the comparison of stress-strain curves above uniform elongation is risky. Total elongation values, measured manually after fracture should be used here.

The tensile strain hardening exponent is determined by the description in international standard 10275 [ISO10275] in addition to the usual mechanical properties.

#### 4.6. Transmission Electron Microscopy

Light microscopy is not appropriate for the characterization of martensitic TRIP assisted steels, cf. chapter 3.6, thus technologies with higher magnification are

necessary. The micrographs are obtained by a JEOL 200CX operated at 200 kV. For this purpose thin sheets are prepared by mild mechanical thinning down to 0.1 mm, followed by die cutting of 3 mm diameter discs, and electrolytic thinning of discs in the solution of 70% methanol and 30% nitric acid using a STRUERS TENUPOL 5 at 15 V and 170 mA.

The phases are identified using electron diffraction, where 200 kV are used to accelerate the electrons to a total energy of  $E=200$  keV. According to Planck's relation, see equation (15), the corresponding wave length is  $\lambda=0.0062$  nm if  $hc=1.23984193$  keV/nm is used for the product of Planck's constant and the speed of light. The nominal camera length of  $L_n=680$  mm is calibrated using a gold reference sample. The lattice spacing  $d_{(hkl)}$  can be derived by a simplified description of Bragg's Law, cf. [Bragg1915], for small angles given in equation (26), if the distance between two opposing diffraction points  $D$  is measured from the diffraction image. If  $D$  is inserted in mm,  $d_{(hkl)}$  is given in nm, cf. the useful description by John McCaffrey [McCaffrey2005].

$$d_{(hkl)} = \frac{\lambda L}{D} \quad (26)$$

TEM diffraction patterns are indexed using JAVA Electron Microscopy Software (JEMS) kindly provided by its developer Prof. Pierre A. Stadelmann of the Interdisciplinary Centre for Electron Microscopy at École Polytechnique Fédérale de Lausanne [Stadelmann1987]. The original diffraction negative size of 88 mm x 63 mm is used to scale the scanned images in digital processing.

All TEM investigations are performed with kind assistance of Prof. Ing. Jozef Janovec and Assoc. Prof. Ing. Mária Dománková at the Slovak Institute of Materials Science, University of Technology in Bratislava.

#### 4.7. X-Ray Diffraction

X-Ray Diffraction measurements are performed on longitudinal sections of the tensile samples with BRUKER AXS D8 ADVANCE diffractometer. Copper radiation, cf. table 6, is used without monochromator. A nickel foil is used as  $k$ -alpha 2 filter. The LYNX-EYE detector in 1D Mode measures  $2\theta$  from  $30^\circ$  to  $130^\circ$  in  $0.02^\circ$  step size and 1 s dwell time per step. The sample rotation is 30 rpm during the measurement. After grinding, the samples are electro polished with STRUERS LECTROPOL with Electrolyte A3 for 120 s, to remove any mechanical artefacts from cutting and grinding causing undesired TRIP effects on the surface.

Table 6: Photon energy and wavelength of used Copper radiation

Source	Energy	Wavelength
Copper anode	8.05 keV	0.15406 nm

Regarding Copper x-radiation, it should be noted that the modern fast 1D energy dispersive Compound Si Strip LYNX-EYE detector, as used in this experiments, is less affected by iron fluorescence at 6.4 and 7.06 keV than conventional detectors. Therefore the discrimination level is set to 0.11 V, what is equivalent to a threshold at

7.7 keV. The separation of diffracted copper X-rays from iron fluorescence ensures adequate signal to noise ratio. The detector technology is described in detail by Josef Kemmer in [Kemmer1985].

In this case, Rietveld refinement with linear background subtraction and offset correction is used to examine the integrated intensities and the lattice parameters from the data. The determination of phase fractions, lattice parameters and carbon content is applied as described for the in-situ experiments in chapter 4.4.

The X-ray diffraction experiments are performed with kind assistance of Prof. Dr. Isabella-Maria Zylla and Dipl.-Ing. (FH) Monika Strickstroock, University of Applied Sciences, Osnabrück.

## 5. Simulation

While austenitization and quenching of low alloyed steels is well understood, less information on the isothermal behavior at low temperatures during the partitioning phase is available. For the design of Quenching and Partitioning heat treatments it is of special interest to retain possible counteracting mechanisms as phase transformation and carbide precipitation of minimal amount and simultaneously achieve full carbon partitioning in the acquisition of homogeneous TRIP behavior.

Initial simulations using well-known valid models are very helpful to find reasonable start parameters and can limit the number of variables thus reducing the necessary number of experiments. In this case, different approaches are used to evaluate reasonable partitioning temperature and corresponding holding time for the material of interest.

The following thermodynamic approaches are used:

- CALculation of PHase Diagrams (CALPHAD),
- calculation of driving forces to estimate the  $T_0$ - and martensite start temperature
- and solid state precipitation of cementite in austenite.

Furthermore, the diffusion of carbon under microstructural aspects of Quenching and Partitioning heat treatment are analyzed by analytical simulations using the theory of Brownian motion:

- planar interface geometry,
- infinite thin plate geometry,
- spherical geometry solutions

and numerical simulations with

- DICTRA under para-equilibrium conditions with mobile interface
- and MATCALC with immobile interface.

As there are no descriptions for transitional carbides in the thermodynamic databases available today, it is impossible to investigate them by means of simulation nowadays.

### 5.1. CALculation of PHase Diagrams (CALPHAD)

MATCALC software is used in version 5.60 (release 1.001) to calculate the orthoequilibrium phase diagram by the CALculation of PHase Diagrams (CALPHAD) approach from thermodynamic databases. [Saunders1998] In this case the MATCALC iron database, version 2.029, created 2014-07-31, assessed in 2014 at TU Wien by Erwin Povoden-Karadeniz is used. The orthoequilibrium condition was first used by Axel Hultgren and is defined by a full thermodynamic equilibrium between the considered phases [Hultgren1947].

The usual stable phases liquid, austenite, ferrite, cementite, aluminum nitride (AlN) and niobium carbon nitride (Nb(C,N)) are considered. Furthermore, because of observation in literature, cf. [Werner1990],  $M_{23}(C,B)_6$  carbides, boron nitrides BN and borides of  $M_2B$  type are also taken into account. The result with the given nominal chemical composition II from table 1 is given in figure 29 as the changes compared to composition I are minute.

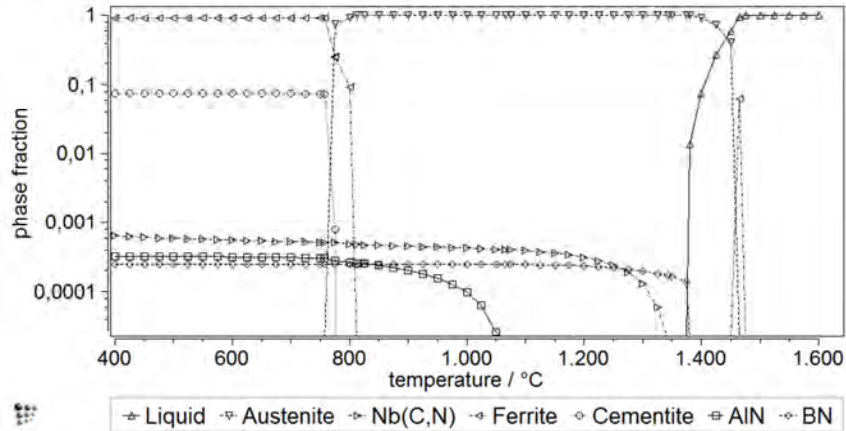


Figure 29: Orthoequilibrium phase diagram of 42SiCrB steel

The comparatively low melting temperature of 1375 °C is caused by the medium carbon content and the boron addition. Boron is enriching within the residual melt during solidification and forms very small amounts of boron nitride (BN) due to the high nitrogen content before reaching the solidus temperature. A contribution of boron to the hardenability of this steel is actually negligible, cf. [Werner1990]. Even without solute boron in austenite the hardening behavior is adequate due to the medium carbon content and considerable chromium additions. Small amounts of niobium carbonitrides and aluminum nitrides are precipitating in austenite as well.  $M_{23}(C,B)_6$  carbides and borides of  $M_2B$  type are calculated to be instable.

The probable formation of stable boron nitride during solidification together with niobium carbonitrides and aluminum nitrides during hot rolling, respectively forging, the niobium, nitrogen and boron content is considered to be negligible for further calculations regarding Quenching and Partitioning heat treatments. Furthermore, the amount of consumed carbon by formation of niobium-carbonitrides is calculated to be only 0.015 wt.%, for this type of medium carbon steels insignificant with regard to the available carbon for partitioning. The simplified chemical composition for the following calculations is given in table 7.

Table 7: Simplified chemical composition

	C	Si	Mn	Cr
I	0.4	2	0.6	1.3

## 5.2. Simulation of the Martensitic Transformation

Since the free Gibbs energies are available for low alloyed steels from thermodynamic databases, the calculation of driving forces for phase transformations is an industry standard. In figure 30 a) the free Gibbs energies from austenite and ferrite of given simplified nominal composition, cf. table 7, are shown and the difference, respectively the driving force, is derived in figure 30 b). The use of the nominal composition implicates no diffusion at all, what is quite reasonable for martensitic transformations, which are diffusionless by definition. The driving force offset is set to 1700 J/mol to be in good agreement with the martensite start temperature of 42SiCrB steel.

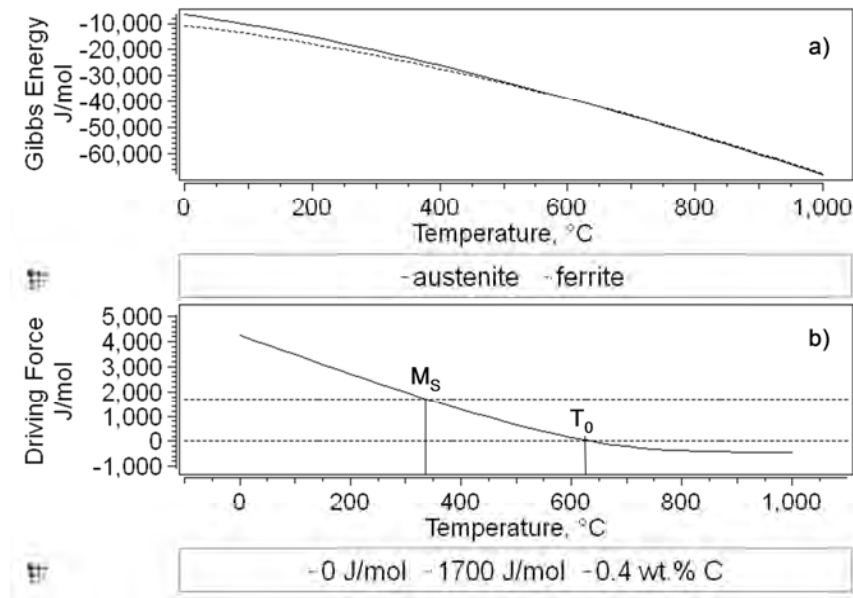


Figure 30: a) Gibbs Energy of austenite and ferrite phase containing 0.4 wt.% C, 2 wt.% Si, 1.3 wt.% Cr, 0.6 wt.% Mn calculated by MATCALC using thermodynamic databases b) the driving force for phase transformation calculated as the difference in Gibbs energy

The driving force, also calculated from thermodynamic databases using MATCALC, shown in figure 31, confirms the effect of carbon on the martensite start temperature  $M_s$  and shows the same effect on the  $T_0$  temperature. Approximately 1.5 wt.% of solute carbon in austenite is necessary to stabilize austenite to room temperature for the 42SiCrB steel of this study.

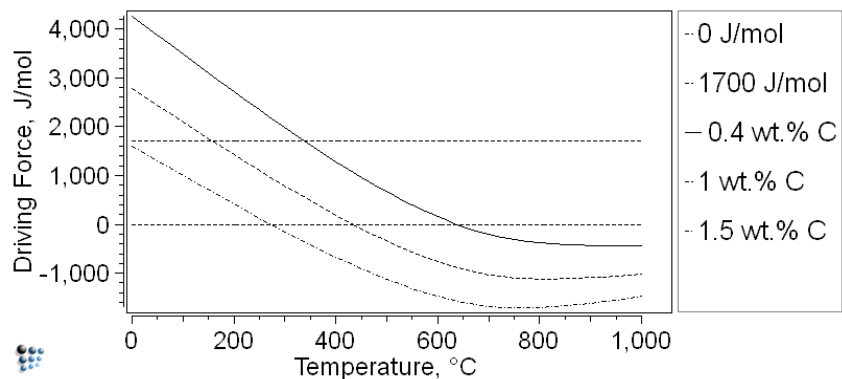


Figure 31: Effect of Carbon content on the Driving Force for martensitic phase transformation calculated with MATCALC using a nominal composition of 2.0 wt.% Si, 1.3 wt.% Cr, 0.6wt.% Mn low alloyed steel

### 5.3. Cementite Precipitation in Austenite

Ernst Kozeschnik and Harshad K. D. H. Bhadeshia already studied the „influence of silicon on cementite precipitation in steels“, as already mentioned in chapter 3.5. They

developed a numerical approach for solid state precipitation of cementite in steels that may be useful to appraise the capability of the given alloy to suppress cementite formation at different partitioning temperatures.

Numerical calculations are performed with the chemistry of 42SiCrB steel from table 7 by analogy with their approach for ortho- and paraequilibrium conditions.

The paraequilibrium, also introduced by Alex Hultgren [Hultgren1947], is characterized by three conditions in detail; cf. the review of Mats Hillert and John Ågren [Hillert2004]:

- substitutional alloying element to iron ratio is equal in both phases,
- equal chemical potential of carbon in both phases and
- a migrating interface.

The austenite dislocation density is estimated to be  $10^{12} \text{ m}^{-2}$ . The resulting time temperature precipitation diagram for cementite nucleating at dislocations in austenite is presented in figure 32.

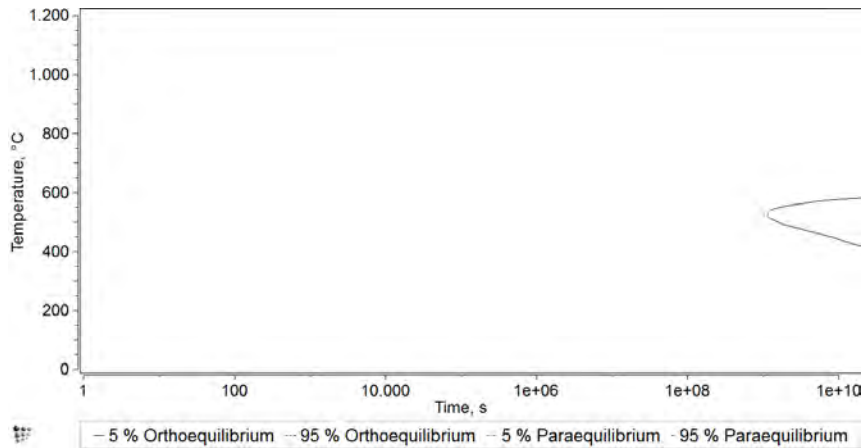


Figure 32: Calculated time temperature precipitation diagram of cementite in 2.0 wt.% Si, 1.3 wt.% Cr, 0.6 wt.% Mn and 0.4 wt.% C austenite. The lines denote the required times to precipitate the given percentage of the final cementite amount with an assigned temperature

It is apparent from the calculations that cementite is extremely unlikely to form in austenite within this composition, taking up to approximately 30 years ( $10^9 \text{ s}$ ). Furthermore, no paraequilibrium cementite is formed during reasonable heat treatment times, using the nominal composition. It should be noted that because of the relative low carbon content the driving forces, cf. figure 33, of paraequilibrium cementite are minimal.



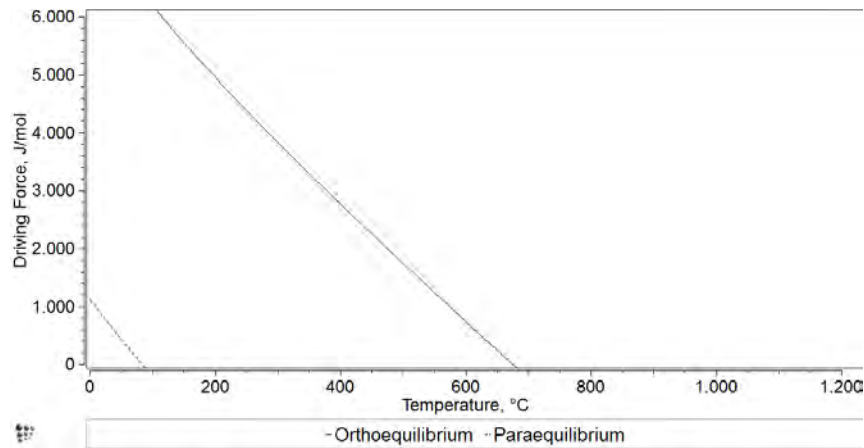


Figure 33: Driving force of cementite precipitation in 2.0 wt.% Si, 1.3 wt.% Cr, 0.6 wt.% Mn austenite with 0.4 wt.% of C for ortho- and paraequilibrium conditions

To ensure cementite is reliably suppressed a substantially higher carbon content of the austenite, due to the carbon diffusion throughout the partitioning phase, must be taken into account. Increasing carbon content raises the driving force for paraequilibrium cementite precipitation dramatically, as shown in figure 34.

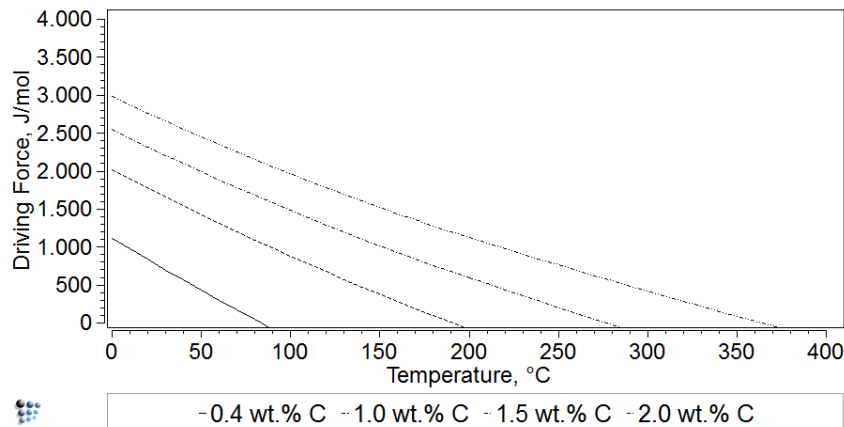


Figure 34: Change in driving force for cementite precipitation due to carbon partitioning in 2.0 wt.% Si, 1.3 wt.% Cr, 0.6 wt.% Mn steel with 0.4, 1.0, 1.5 and 2.0 wt.% C under paraequilibrium condition

The resulting time-temperature-precipitation diagram for 2.0 wt.% of carbon is plotted in figure 35. The simulation shows that cementite precipitation in carbon enriched retained austenite is to be expected at temperatures above 600 °C and additionally at low temperatures between 200 °C and 300 °C, if reasonable heat treatment times of 3 h maximum (10,000 s) are considered. In other words, the  $42\text{SiCrB}$  steel offers a wide range of possibilities for successful carbon partitioning without counteracting cementite formation.

The source codes of the MATCALC scripts used for the calculations in this chapter are given in Appendix B and C.

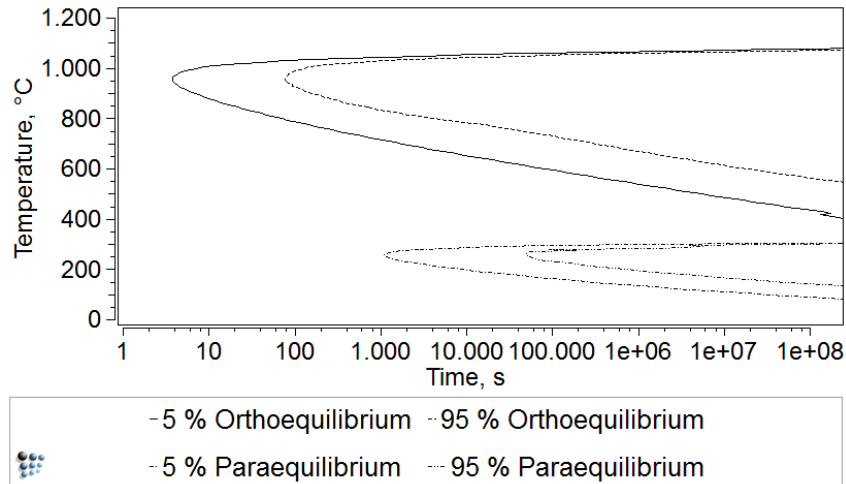


Figure 35: Calculated time temperature precipitation diagram of cementite in 2.0 wt.% Si, 1.3 wt.% Cr, 0.6 wt.% Mn and 2.0 wt.% C austenite. The lines denote the necessary times to precipitate the given percentage of the final cementite amount at a given temperature

#### 5.4. Stability of Retained Austenite in Absence of Cementite

As long as the cementite formation is considered to be suppressed by the high silicon addition, the system is reduced to ferrite, for martensite, and austenite only. This offers the opportunity to analyze the equilibrium after Quenching, therefore in paraequilibrium, although this is a wide extrapolation of the experimentally validated thermodynamic data. The resulting Fe-C phase diagram is drawn in figure 36 and it shows an extended ferrite and austenite region at low temperatures.

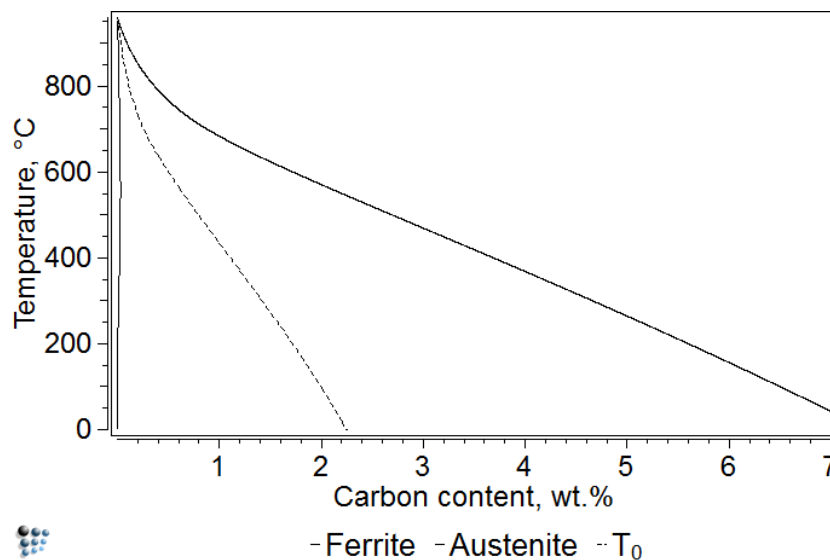


Figure 36: Paraequilibrium Fe-C phase diagram in the iron rich corner of 2.0 wt.% Si, 1.3 wt.% Cr, 0.6 wt.% Mn steel with suppressed cementite formation; the dashed line represents the T<sub>0</sub>-Temperature

If paraequilibrium is considered to be valid for the alloy detailed in this study, the final phase fraction of retained austenite is directly and only dependent on the partitioning temperature. The resulting phase fractions for  $42\text{SiCrB}$  steel under paraequilibrium and suppressed carbide formation are given in figure 37. Reasonable phase fractions of austenite, e.g. 0.07 at room temperature and 0.23 at 600 °C are stable as long as cementite has not formed. It has been suggested that nearly all of the available carbon is diffusing into the austenite and reaches partitioning temperatures below 550 °C carbon levels exceed 2.2 wt.%. This amount represents the  $T_0$ -Temperature at room temperature, and ultimately leads to chemically stable retained austenite and to a loss in transformation induced plasticity (TRIP).

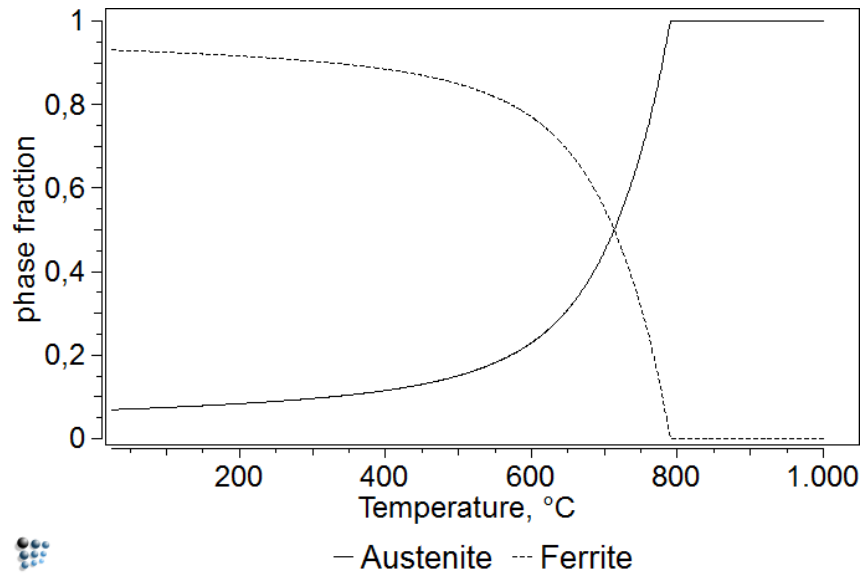


Figure 37: Phase fraction of austenite and ferrite vs. temperature calculated for paraequilibrium of 0.4 wt.% C, 2.0 wt.% Si, 1.6 wt.% Cr and 0.6 wt.% Mn steel if cementite precipitation is suppressed

### 5.5. Microstructural Aspects of Quenching and Partitioning

For the simulations of carbon partitioning in martensitic TRIP assisted steels adequate information about the microstructure is essential. Referring to the description of the martensite structure described in chapter 3.6, principally retained austenite can be observed at any interface between martensite lath, blocks, packages or the prior austenite grain boundary. In figure 38, the microstructural situation after interrupted quenching to a martensite phase fraction of approximately 0.7 is taken from Koseki's in-situ video to analyze the retained austenite structures.

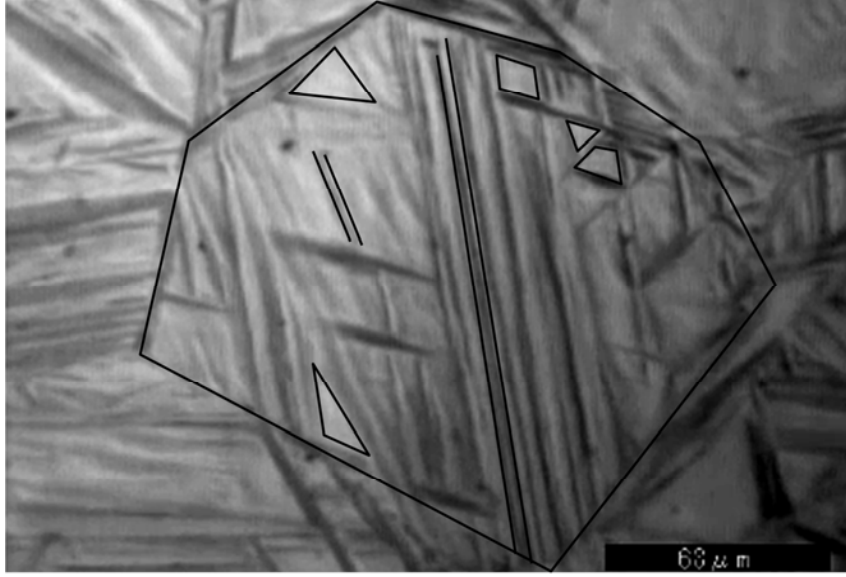


Figure 38: Proposed structure of martensitic TRIP assisted steels. Polygons and lines suggest the areas and shape of retained austenite. The background image is taken from [Koseki2011]

It follows that retained austenite, surrounded by martensite packets, is polyhedra-shaped caused by the significant misorientation between the packets. By means of two-dimensional microscopy, the retained austenite isles appear as convex polygons. Between the laths and blocks, the retained austenite remains as thin foils appearing as thin lines in a two-dimensional view. Very similar structures are described by X. D. Wang et al. for Quenching-Partitioning-Tempering microstructures. [Wang2011].

To obtain reasonable sizes of the retained austenite isles for this simulation the description of the number of martensite plates per grain, cf. equation (27) taken from Hong-Seok Yang and Harshad K. D. H. Bhadeshia [Yang2009], is used.

$$N^{\alpha} = \exp\left\{-\frac{\ln(1 - V^{\alpha})}{m}\right\} - 1 \quad (27)$$

$N^{\alpha}$  is the Number of martensite laths per grain in dependence of the martensite phase fraction  $V^{\alpha}$  and the martensite plate aspect ratio  $m$ . The number of retained austenite compartments is given by the assumption that every new martensite lath divides a compartment and creates thus an additional one:

$$N^{\gamma} = N^{\alpha} + 1 \quad (28)$$

Combined with the average austenite grain volume  $V_0$  the average volume of retaining austenite compartments  $V_{\text{retained}}^{\gamma}$  is easily derived by:

$$V_{\text{retained}}^{\gamma} = \frac{V_0 V^{\gamma}}{N^{\gamma}} \quad (29)$$

From the equations above it is evident that the average retained austenite dimensions are dependent on the prior austenite grain size, the retained austenite volume fraction

and the corresponding quenching temperature and the aspect ratio of the martensite lath or plates  $m$ .

Assuming a spherical shape of the initial austenite grains, with an average volume  $V_0$  and polyhedra-shaped retained austenite isles, also simplified by a sphere, the average diameter of the retained austenite isles can be calculated using aspect ratio of  $m=0.1$ , an average prior austenite grain diameter of  $20\ \mu\text{m}$  and the austenite phase fraction determined by the Koistinen-Marburger equation with the values of  $42\text{SiCrB}$  steel taken from table 2. The result is plotted together with the amount of retained austenite obtained by the Constrained Carbon Equilibrium model in figure 39.

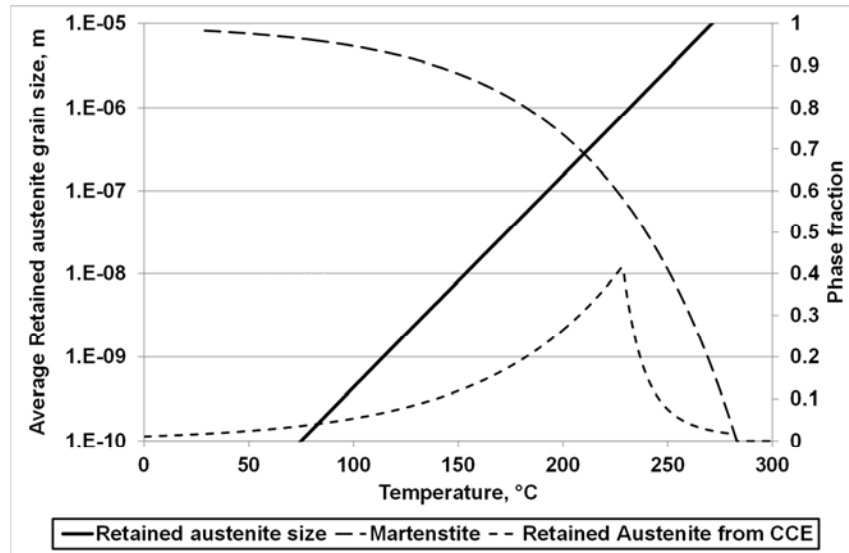


Figure 39: Dependence of the average size of retained austenite from quenching temperature and the corresponding retained austenite volume fraction calculated by CCE model

The calculated average size of the retained austenite reaches up to  $1\ \mu\text{m}$  size at the highest retained austenite volume at  $225\ ^\circ\text{C}$ , ranging down to atomistic dimensions at very low quenching temperatures. This is consistent with that up to 20% of retained austenite is sometimes invisible to light optical microscopy in martensitic steels [Hougardy1990], implying that the size of austenite is in average smaller than  $1\ \mu\text{m}$ , which is the maximum light optical microscopy resolution.

Nevertheless, larger isles of retained austenite are likely to be observed as the considerations above calculate average values. To predict partitioning times ensuring full partitioning a conservative approach is necessary, hence, in the following simulations up to  $2\ \mu\text{m}$  big isles are considered as worst case scenario for  $42\text{SiCrB}$  steel.

## 5.6. Diffusivity of Carbon

Carbon diffusivity in austenite is well known in carburization of case hardened steels at high temperatures. Because the temperature dependence of diffusion processes is well described by the Arrhenius equation, it is feasible to use an extrapolation to low temperatures as well, i.e. the results will give the correct order of magnitude.

All the following simulations, analytic and numeric, use the same carbon diffusivity in austenite assessment of John Ågren, given in equations (30) and (31). [Ågren1986] The coefficient  $x_C$  is represents the molar fraction of carbon and  $T$  is the absolute temperature in K.

$$D = 4.53 \cdot 10^{-7} \left\{ 1 + y_C (1 - y_C) \cdot 8339.9 \cdot T^{-1} \right\} \cdot e^{\left\{ (-T^{-1} - 2.221 \cdot 10^{-4}) (17767 - 26436 \cdot y_C) \right\}} \quad (30)$$

$$y_C = \frac{x_C}{1 - x_C} \quad (31)$$

In figure 40, the diffusion coefficient assessment of John Ågren is plotted versus reciprocal logarithmic Temperature and different carbon contents ranging from 0-2 wt.%. It is very important to recognize the present carbon influence on its own diffusion: e. g. 1 wt.% higher carbon content increases the diffusion coefficient by one order of magnitude.

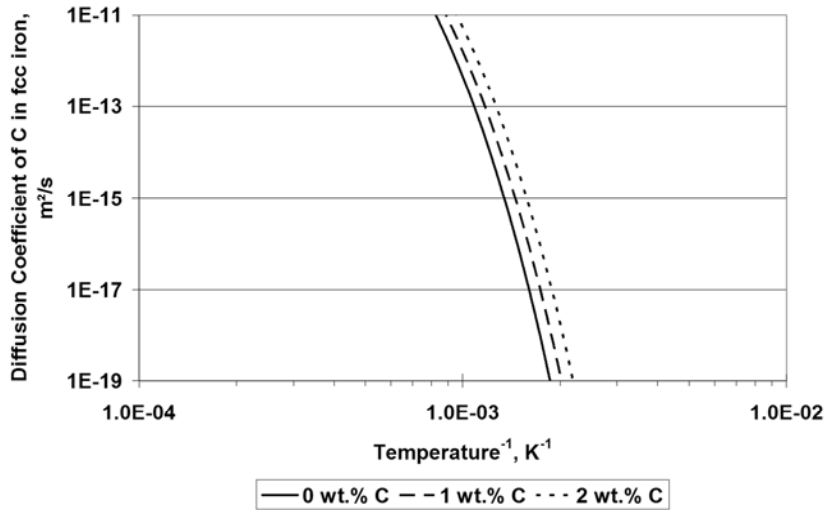


Figure 40: Diffusion Coefficient of Carbon in austenite versus logarithmic reciprocal Temperature for carbon contents of 0 wt.%, 1 wt.% and 2 wt.% and Temperatures between 100 °C and 1000 °C

If the carbon concentration varies locally, as it does usually within carbon diffusion problems, it is difficult to find a representative diffusion coefficient for analytical calculations. Therefore, John Crank proposed a mean diffusion coefficient [Crank1979] to consider this effect.

$$\bar{D} = \frac{1}{c_{\max} - c_{\min}} \int_{c_{\min}}^{c_{\max}} D(c) dc \quad (32)$$

To use this equation by the means of Quenching and Partitioning the maximum carbon content  $c_{\max}$  in austenite can be calculated under Constrained Carbon Equilibrium conditions from equation (2), if the phase fraction of retained austenite is recognized. In figure 41, the effect of the retained austenite volume fraction on the mean diffusion coefficient is displayed. Keeping in mind, that the necessary time for partitioning is linear dependent on the diffusion coefficient, it is evident that the small

volume fractions of retained austenite can enhance the kinetics by orders of magnitude.

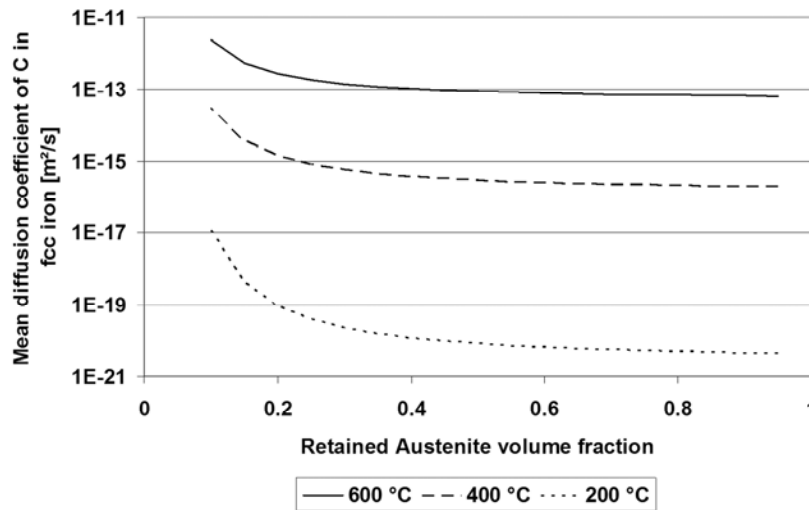


Figure 41: Mean carbon diffusion coefficient in austenite in dependence of the retained austenite volume fraction calculated under Constrained Carbon Equilibrium conditions

The diffusion of carbon in ferrite and martensite is not considered in these analytical calculations, because at the same temperature, the diffusion of carbon in ferrite is 100 times faster and thus carbon diffusion in austenite is the dominant effect by means of partitioning time. Nevertheless, it is of course considered in the numerical simulations; the corresponding parameters are taken from Björn Jönsson [Joensson1994].

## 5.7. Analytical Simulation of Carbon Partitioning

Analytical calculations are preferred in many cases, because with marginal effort ideal solutions are obtained and physical interactions and the influence of variables are obvious from the derived equations. We use different solutions of Adolf Eugen Fick's 2<sup>nd</sup> law of diffusion [Fick1855] to describe the fundamental dependencies under particular boundary conditions. The following boundary conditions are used for all analytical approaches:

- constant diffusion coefficients,
- uniform initial distribution of nominal carbon content (0.42 wt.%),
- constant interface carbon content
- and an immobile interface.

### 5.7.1. Random Walk

A fundamental approach to describe diffusion analytically is the theory of Brownian motion and its mathematical description by random walk. Albert Einstein [Einstein1905] and Marian von Smoluchowski [Smoluchowski1906] found independently the following dependence of the root mean squared displacement of random walkers, the diffusion coefficient and time:

$$x_{\text{RMS}} = \sqrt{2Dt} \quad (33)$$

The root mean square value of displacement of random walkers, denoted with  $x_{\text{RMS}}$ , is proportional to the square root of diffusion coefficient  $D$  and the square root of time  $t$ . By the means of Quenching and Partitioning heat treatments it is recognizable, that the time for partitioning is proportional to the squared austenite dimension, i.e. if the size of austenitic zones is known the necessary time for partitioning can be approximated. In view on the fact that the carbon diffusivity is known, as previously described, we can calculate individual intervals for effecting differently sized zones of austenite at given temperatures if the retained austenite volume fraction and the corresponding diffusivity are given.

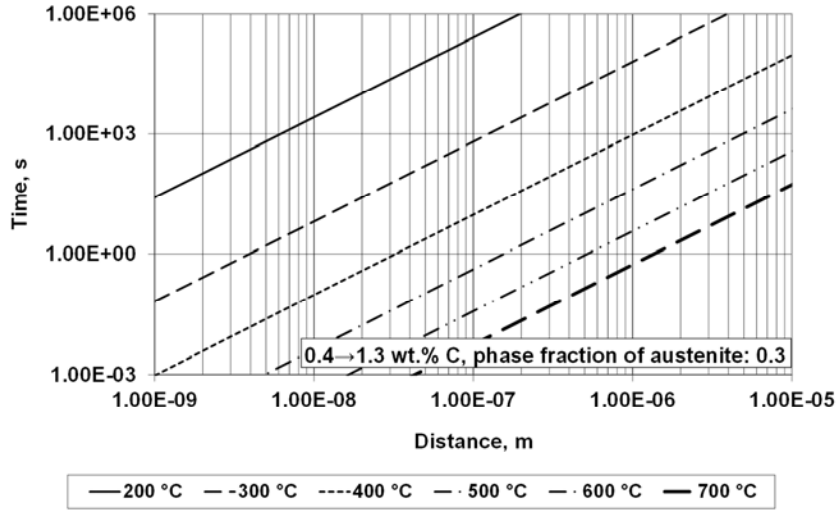


Figure 42: Approximation of necessary diffusion time to affect differently sized austenitic zones at a given temperature in dependence of the temperature calculated for 0.4→1.3wt.% Carbon, respectively retained austenite phase fraction of 0.3, using the Einstein- Smoluchowski equation

As shown in figure 42, at 200 °C austenitic zones in the size of a few nanometers are affected by carbon partitioning within a few minutes, while it is possible to perform carbon partitioning at 300 °C within seconds in this dimension. Above 400 °C it should be possible to enrich zones in the size of micrometers in a few minutes.

### 5.7.2. Analytical Solution for planar Interface

The analytical Solution of Adolf Eugen Fick's 2<sup>nd</sup> law of diffusion for infinite half-space with given boundary conditions developed by C. E. Van Orstrand and F. P. Dewey, [VanOrstrand1915] leads to the following expressions taken from John Crank [Crank1979] using the Gaussian error function erf():

$$\frac{(c_c - c_{c,\text{Interface}})}{(c_{c0} - c_{c,\text{Interface}})} = \text{erf}\left(\frac{x}{2\sqrt{Dt}}\right) \quad (34)$$



$$c_C = (c_{C,Interface} - c_{C0}) \cdot \operatorname{erf}\left(\frac{x}{2\sqrt{Dt}}\right) + c_{C0} \quad (35)$$

$$t = \frac{x^2}{4D} \left( \operatorname{inverf} \left( \frac{c_C - c_{C,Interface}}{c_{C0} - c_{C,Interface}} \right) \right)^{-2} \quad (36)$$

Using  $c_C = \frac{c_{C,Interface} - c_{C0}}{2}$  with a simple approximation for the Gaussian error function  $\operatorname{erf}(0.5) \approx 0.5$ , i.e. defining the point of half carbon balancing range  $\bar{x}$ , the approximation of this solution, widely used in carburization processes [Gegner2006], is derived:

$$t = \frac{\bar{x}^2}{D} \quad (37)$$

$$\bar{x} = \sqrt{Dt} \quad (38)$$

The difference to the solution of Einstein-Smoluchowski is caused by the unequal definitions of mean diffusion. This solution and the already calculated one of Einstein-Smoluchowski are quite similar. The factor of two in time does not change the results in general.

### 5.7.3. Analytical Solution for infinite thin Plate

John Crank [Crank1979] delivers further analytical solutions for other geometrical boundary conditions, e. g. the infinite thin plate, describing the situation of retained austenite between parallel martensite blocks very well. The solution of course is analytical, but it is helpful to find the limit of the infinite series by numeric help. Unfortunately, it is not possible to solve the equation analytically for the time  $t$ , but with today computing capacity the equation is calculated very fast.

The carbon concentration profile of the infinite thin plate is given by:

$$c_C = c_{C,Interface} + \frac{4(c_{C0} - c_{C,Interface})}{\pi} \sum_{n=0}^{\infty} \frac{1}{2n-1} \sin \frac{(2n+1)\pi x}{l} \exp \left[ -(2n+1)^2 \pi^2 \frac{Dt}{l^2} \right] \quad (39)$$

Using the mean diffusion coefficient and for example a 2  $\mu\text{m}$  thin foil of retained austenite, embedded in martensite blocks, the carbon distribution within the plate can be calculated, as shown in figure 43 for 200 °C and figure 44 for 400 °C.

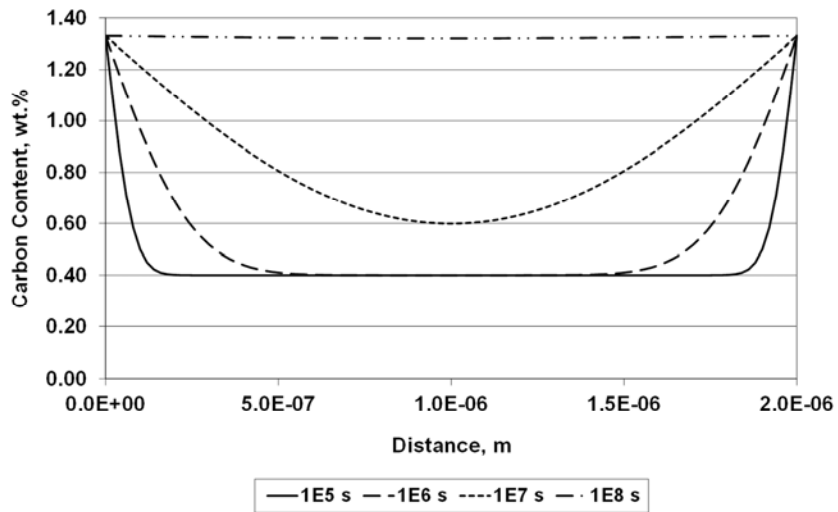


Figure 43: Carbon partitioning to 2  $\mu\text{m}$  infinite thin plate at 200  $^{\circ}\text{C}$

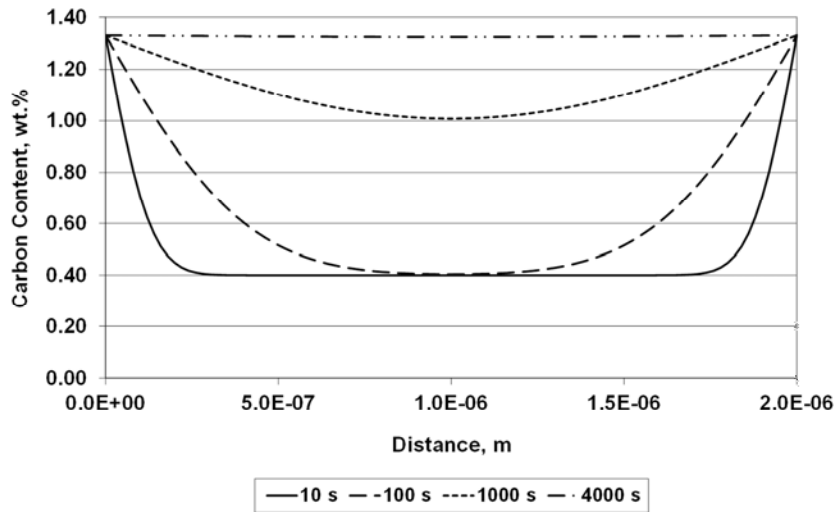


Figure 44: Carbon partitioning to 2  $\mu\text{m}$  infinite thin plate at 400  $^{\circ}\text{C}$

Furthermore, the investigation of the necessary time to perform full partitioning is possible by focusing on the center of the thin plate. These results are plotted in figure 45, showing carbon content of the center versus time. The time for full partitioning at given temperature is available for direct reading; 3,000 s at 400  $^{\circ}\text{C}$  and about  $1\text{e}^8$  s at 200  $^{\circ}\text{C}$ .

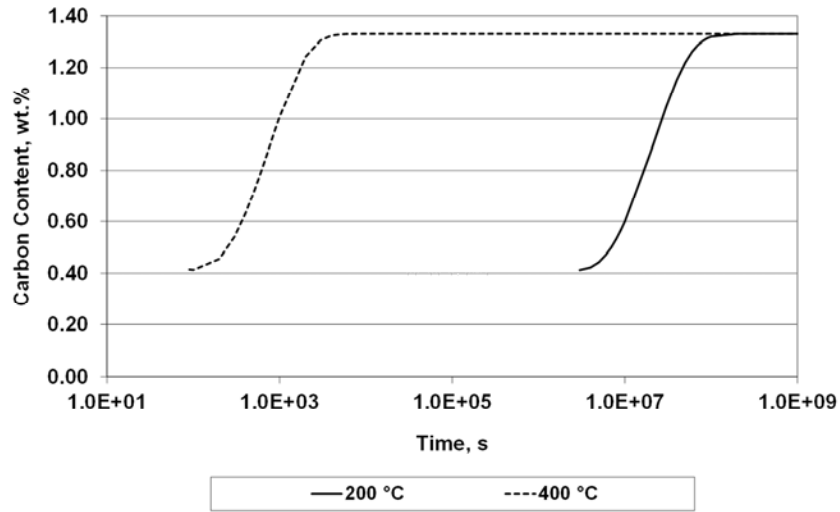


Figure 45: Carbon content of the center plane of the 2  $\mu\text{m}$  thin retained austenite film between martensite blocks in dependence of partitioning time, calculated analytically with mean diffusion coefficient at 200 °C and 400 °C

#### 5.7.4. Analytical Solution for spherical Interface

The model of the infinite thin plate is pragmatic in small layered structures of retained austenite, but it must be considered as invalid for micrometer sized austenite isles between martensite blocks. These isles are usually surrounded by the flat surfaces of martensite packets and therefore shaped like polyhedra. We use a spherical geometry to describe these polyhedra, as this is the best approximation, where analytical solutions are available.

The solution for the spherical geometry is given by John Crank [Crank1979] as:

$$c_C = c_{C, \text{Interface}} + \frac{2a(c_{C, \text{Interface}} - c_{C0})}{\pi r} \sum_{n=0}^{\infty} \frac{(-1)^n}{n} \sin \frac{n r \pi}{a} \exp \left[ -n^2 \pi^2 \frac{D t}{a^2} \right] \quad (40)$$

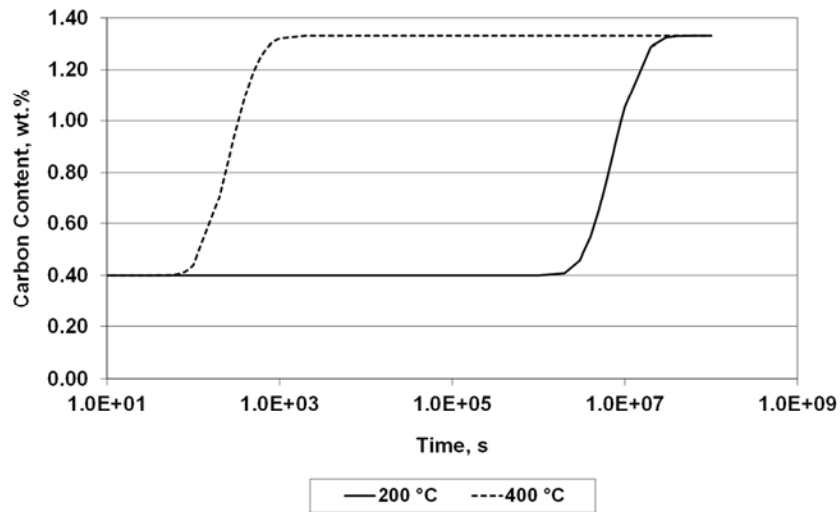


Figure 46: Analytical Carbon Partitioning Simulation in the center of the spherical geometry with two micrometers diameter at 200 °C and 400 °C for retained austenite volume fraction of 0.3

Figure 46 is calculated with the same parameters of the infinite thin plate investigated in the previous chapter, but with spherical geometry. It shows three times faster kinetics for 200 °C and 400 °C as well. The spherical geometry offers better boundary conditions for diffusion processes. Due to the fact that a sphere offers 3 times more effective surface per volume than a cube element in a plane sheet, provided that sphere diameter equals sheet thickness, the results are consistent.

For the two micrometer sized austenitic sphere in martensitic matrix the calculation results are shown in figure 47 at 200 °C and in figure 48 at 400 °C.

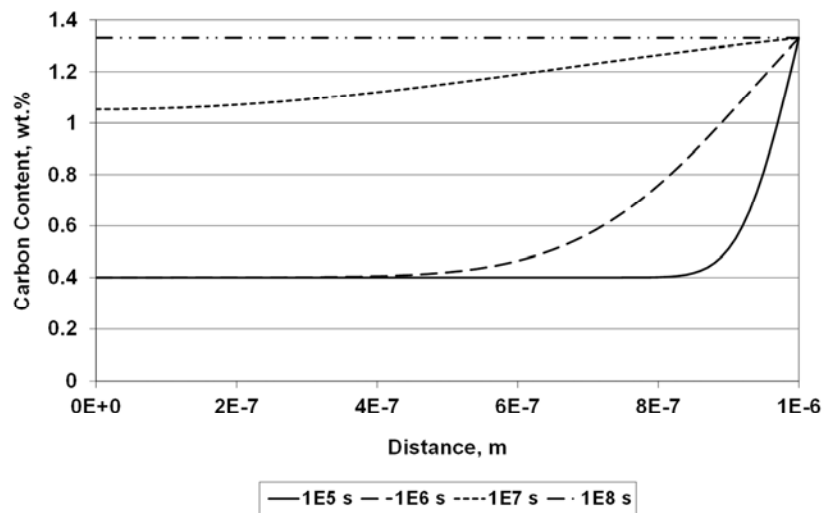


Figure 47: Analytical carbon Partitioning in two micrometer austenite sphere at 200 °C for retained austenite volume fraction of 0.3

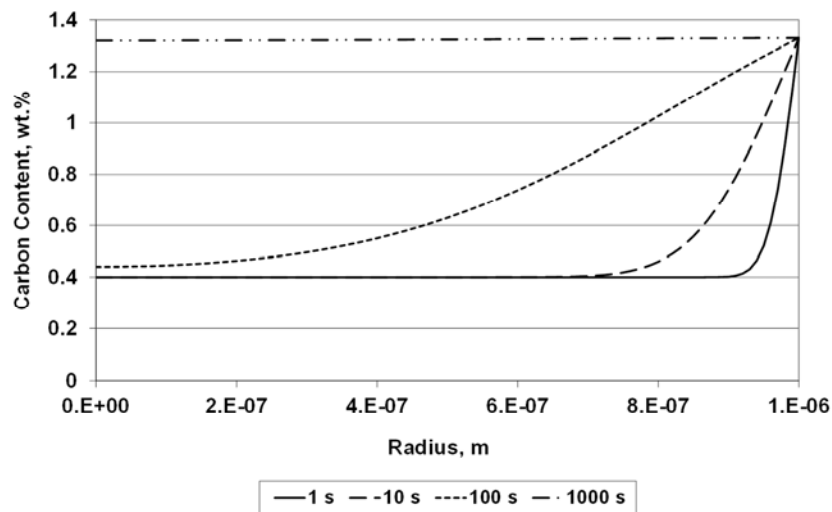


Figure 48: Analytical carbon Partitioning in two micrometer austenite sphere at 400 °C for retained austenite volume fraction of 0.3

According to this calculation, the Partitioning heat treatment lasts years at 200 °C to stabilize two micrometer-sized retained austenite. If the temperature is increased by 200 °C only 15 minutes are necessary. This is an applicable time for means of industrial use.

## 5.8. Numerical Simulation of Carbon Partitioning

The fundamental advantage of numerical simulations is to solve problems where no analytical solutions are available. Additionally, it is possible to reduce the number of necessary assumptions and hence, the simulations should become more realistic. In this case of numerical carbon partitioning simulation, the calculations are compared to the analytical simulations enhanced by:

- local carbon diffusion coefficients,
- dynamic carbon content at the interface
- and optional mobile interfaces.

The uniform initial distribution of nominal carbon content (0.42 wt.%) is still necessary, but this is a valid assumption after full austenitization and rapid quenching, as it is performed in the experiments of this study.

In general, there are also fundamental differences between the analytical solutions of Adolf Eugen Fick's first law of diffusion [Fick1855] and the up to date physical definition for diffusion. In Fick's phenomenological first law, given in equation (41), the flux of atoms is only dependent on the diffusion coefficient  $D$  and the gradient of concentration.

$$J = -D\nabla c \quad (41)$$

Today, the description of the flux is dependent on the gradient of the chemical potential  $\mu$  and the mobility  $B$ , as shown in equation (42).

$$J_i = c_i B_i \nabla \mu_i \quad (42)$$

The index “i” denotes the main advantage of this description of diffusion that it considers multi component systems and the interaction between its elements. [Kozeschnik2012]

Two different multi component diffusion software packages using CALPHAD-type thermodynamic and mobility databases are used to perform carbon partitioning simulations: DICTRA and MATCALC.

### 5.8.1. DICTRA Simulation with mobile Interface

The Abbreviation DICTRA shortens “Diffusion Controlled phase TRAnsformation”, what describes the general purpose of the software package. The calculation of multi component diffusion in and between phases is a main part of DICTRA. A general Description of DICTRA is given in [Andersson2002].

The calculations are performed with kind assistance of Prof. Dr. rer. nat. Gerhard Inden. DICTRA in version 27.0 (released 2013-06-27) and the TCS Steel Mobility Database Version 2.0 (2011-12-09) are used.

All DICTRA simulations are calculated under a paraequilibrium condition, i.e. all substitutional atoms are considered immobile, what is reasonable assumption for low alloyed steels at temperatures below 600 °C, because the diffusion of substitutional atoms is very slow compared to the interstitial carbon atoms this study is interested in. Mats Hillert and John Ågren recently reviewed the definitions [Hillert2004] of ortho- and paraequilibrium, which is characterized by three conditions in detail:

- substitutional alloying element to iron ratio is equal in both phases,
- equal chemical potential of carbon in both phases and
- migrating interface.

Martensite is described in the following calculations as ferrite with enhanced diffusion mobility of solute elements; respectively a best practice factor of 45 is used, cf. [Dmitrieva2011]. The material composition is Fe-0.4 wt.% C, 1 wt.% Cr, 1 wt.% Mn, 0.5 wt.% Mo and 2 wt.% Si. The retained austenite elements are modelled as spheres, see figure 49.

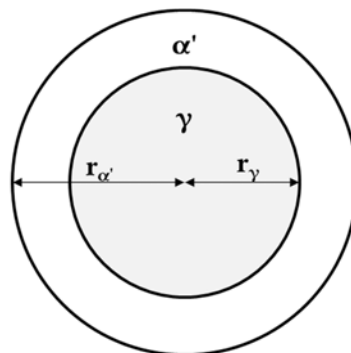


Figure 49: Two-dimensional view of the model used for the DICTRA calculations

In chapter 5.5 it is suggested that micrometer sized retained austenite isles must be considered in martensitic TRIP steels. Hence, the radius for the austenite sphere is set to  $r_\gamma=1 \mu\text{m}$ . Since the initial volume fraction of austenite after quenching is set to 0.3 the radius of the martensitic matrix sphere results to  $r_\alpha=1.5 \mu\text{m}$ . The calculations are carried out on two temperatures: 200 °C and 400 °C.

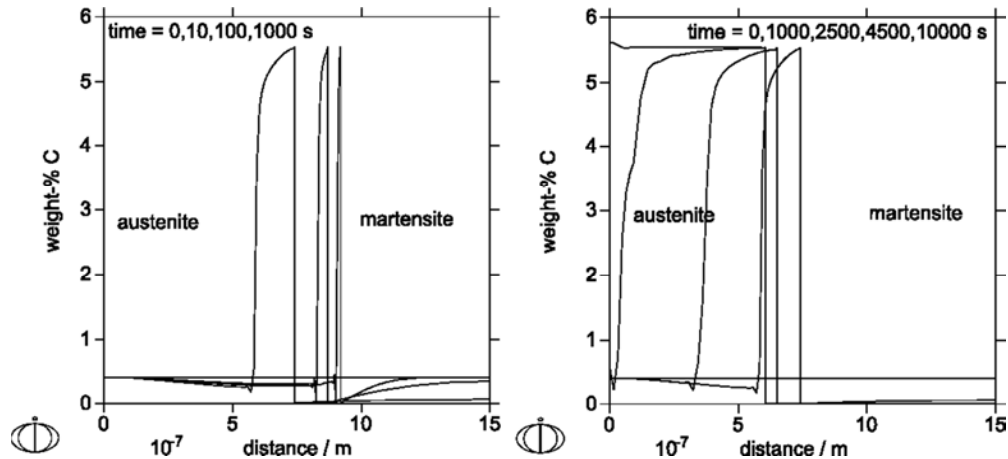


Figure 50: Carbon redistribution at 200 °C, 0.3 initial volume fraction of austenite, isothermal 200 °C spherical geometry, paraequilibrium, times up to 1000 s left and above 1000 s right

As shown in figure 51, the diffusion of carbon at 200 °C result is an enormous increase of carbon at the interface. Until 1000 s are passed by, carbon diffuses from martensite to austenite, afterwards the carbon levels within the austenite only. This process is completed after 5,000 s.

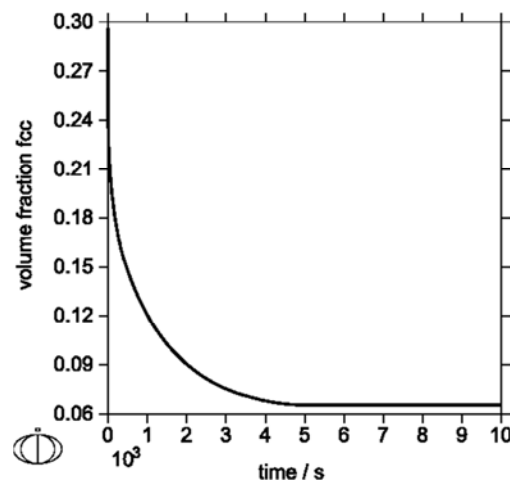


Figure 51: Evolution of austenite phase fraction vs. time during partitioning at 200 °C under paraequilibrium conditions

Furthermore, the volume fraction of retained austenite is shrinking dramatically within the first seconds, as shown in figure 51, because in this case less carbon is available to stabilize as much austenite.

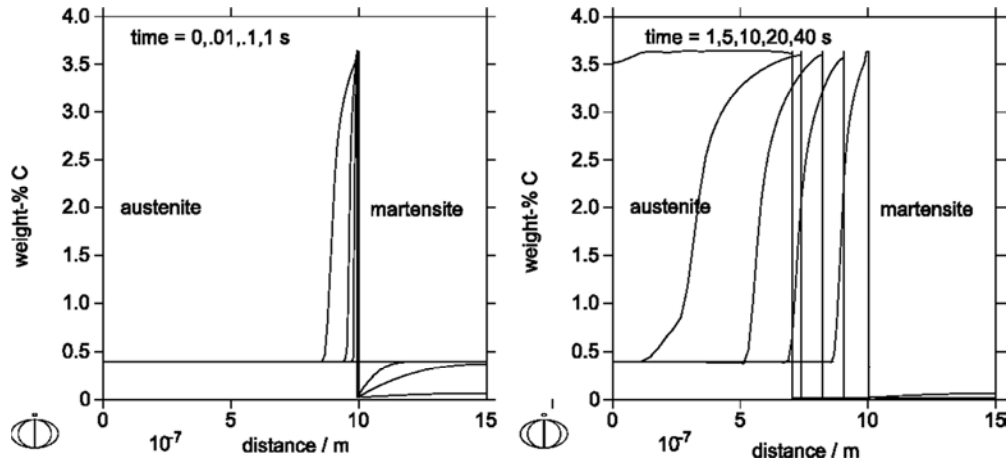


Figure 52: Carbon redistribution at 400 °C with 0.3 initial volume fractions of austenite, spherical geometry and paraequilibrium

In general, results at 400 °C, shown in figure 52 and figure 53, appear to be the same compared to 200 °C, although with much faster kinetics. Additionally, the amount of stabilized retained austenite is increased slightly to 0.1, according to the equilibrium considerations in chapter 5.4. For a very short time of 1 s, growth of austenite is observed.

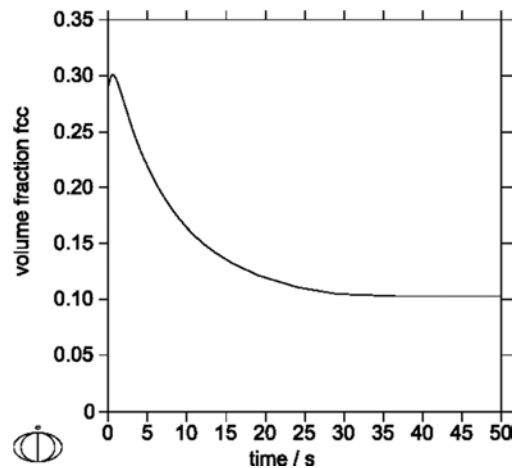


Figure 53: Evolution of austenite phase fraction vs. time during partitioning at 400 °C under paraequilibrium conditions

### 5.8.2. MATCALC Diffusional Simulation with stationary Interface

MATCALC was basically addressed to the simulation of precipitation kinetics in steel. During 20 years of continuous development, MATCALC emerged to a software suite dealing additionally with phase equilibria, diffusion, phase transformations and Monte Carlo simulation. [Svoboda2004][Kozeschnik2004]

In this case, MATCALC version 5.60 (release 1.001), TU Wien, 2014 by Ernst Kozeschnik is used together with the MATCALC iron database, version 2.029, created 2014-07-31 and the MATCALC mobility diffusion steel database, version v2.006, created 2014-03-10, both assessed in 2014 at TU Wien by Erwin Povoden-Karadeniz.



All diffusional calculations are performed with orthoequilibrium conditions, but constrained by suppressed interface migration on a planar model, depicted in figure 54 representing film type retained austenite between martensite laths or blocks.

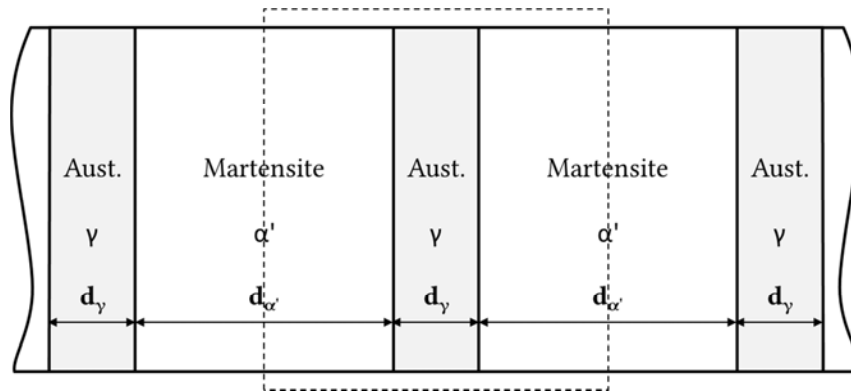


Figure 54: Two-dimensional view of the planar model used for the MATCALC calculations. The dashed line represents the simulated section

The martensite and austenite areas are discretized by 170 planar cells of equal size connected by immobile interfaces, representing austenite thickness  $d_\gamma$  of  $2\ \mu\text{m}$  and  $4.8\ \mu\text{m}$  martensite thickness  $d_{\alpha'}$ , respectively constant austenite phase fraction of 0.3. Planar geometry is chosen because sphered geometries are not available in MATCALC today, but it was already mentioned in chapter 5.7.4, that spheres are partitioned three times faster than plates. Martensite is described in the following calculations as ferrite; no diffusional enhancement is used as it makes no significant difference as the austenite phase diffusion is the limiting factor, cf. chapter 5.6. The considered simplified nominal composition is taken from table 7. The corresponding template of the MATCALC script source code is given in appendix D and the result of the simulations at  $200\ ^\circ\text{C}$  are shown in figure 55 and figure 56.

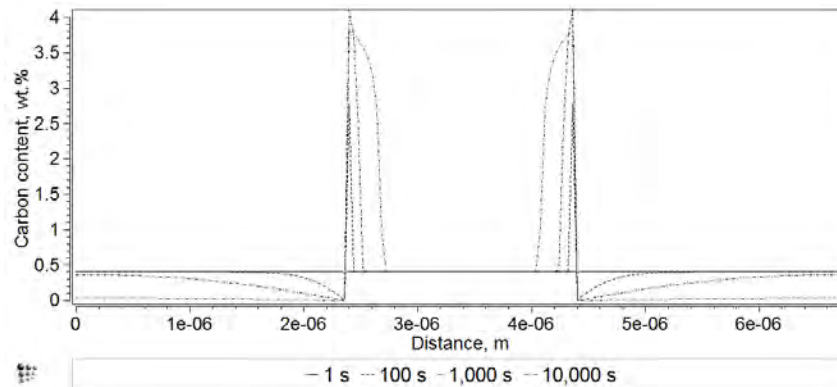


Figure 55: Numeric MATCALC carbon partitioning simulation for  $2\ \mu\text{m}$  film between martensite at  $200\ ^\circ\text{C}$

The very high carbon pile up at the interface of 4 wt.% is distinctive, but is explainable by the high difference in carbon diffusivity between austenite and martensite. The whole martensite is depleted from carbon within 10,000 s, afterwards the simulation is characterized by carbon redistribution within the austenite only.

For longer partitioning than 10,000 s, the ongoing simulation at 200 °C is carried out on a reduced model with reduced number of planar cells, that is 34, to keep the necessary time comfortable. Figure 56 shows the results for high partitioning times up to 2,500,000 s, respectively 29 days, which are necessary for full carbon partitioning.

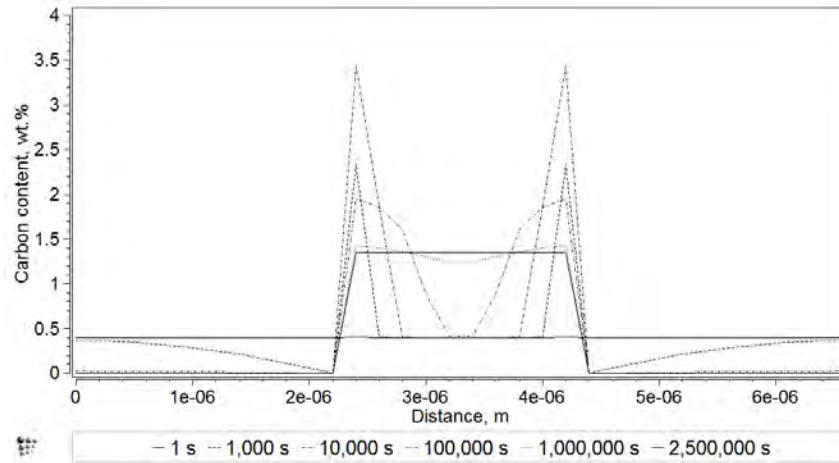


Figure 56: Numeric MATCALC carbon partitioning simulation for 2  $\mu\text{m}$  austenite film between martensite at 200°C for 2,500,000 s

In figure 57, the results for 400 °C partitioning are presented. In this case the pile up of carbon at the interface reaches 3 wt.%. The martensite is depleted in carbon within 100 s and finally, after 1,000 s the carbon is well-balanced within the austenite.

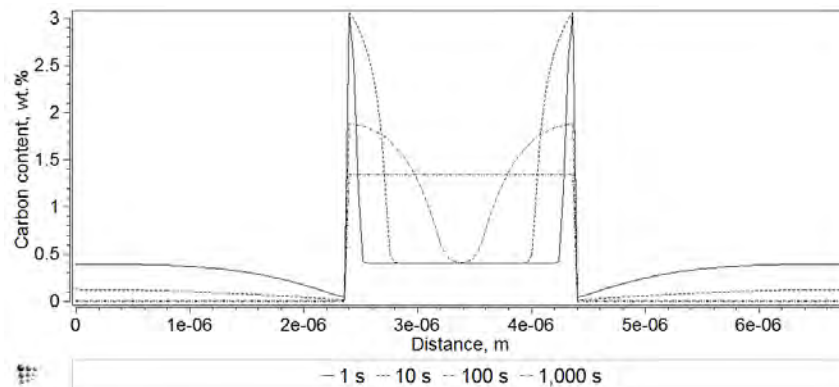


Figure 57: Numeric MATCALC carbon partitioning simulation for 2  $\mu\text{m}$  film between martensite at 400°C

## 6. Results

The results from dilatometry, in-situ X-ray diffraction, transmission electron microscopy and tensile testing are shown in this chapter. Detailed experimental descriptions are already given in chapter 4.

### 6.1. Phase Transformation Diagrams

Every dilatometric investigation presented here starts with the experimental combination of time, temperature and the change in length. It is followed by calculations to get information about the phase transformations causing the change in length, if applicable. Since the initial length of all dilatometer samples in this study is  $l_0=10$  mm the change in length is compared by absolute values.

As plots showing temperature and dilatation versus time are not very meaningful in continuous experiments, we plot the change in length over temperature instead. The very high sampling rate, set to 1,000 data points per segment, guarantees sustainable data and allows to plot lines instead of data points for better graphical representations. For  $42\text{SiCrB}$  steel three characteristic cooling curves are selected to present a varied picture beside one heating curve.

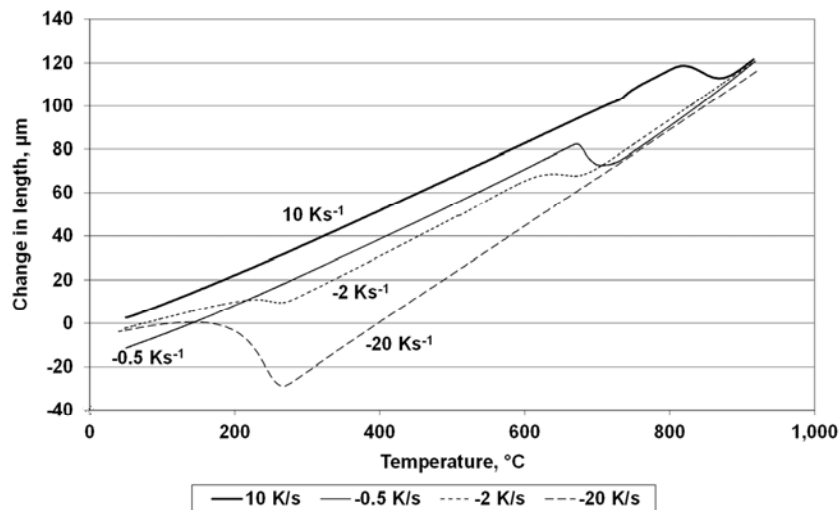


Figure 58: Change in length versus temperature for continuous heating with  $10\text{ Ks}^{-1}$  and continuous cooling with  $0.5\text{ Ks}^{-1}$ ,  $2\text{ Ks}^{-1}$  and  $20\text{ Ks}^{-1}$  of  $42\text{SiCrB}$  steel

Up to cooling rates of  $40\text{ Ks}^{-1}$ , we achieved a stable linear behavior if only thermal expansion is present. This indicates homogeneous temperatures within the sample volume. As long as temperature remains homogeneous in the sample the change in length is not affected by temperature gradients.

The distinctive unexpected change in the heating dilatation curve at  $730\text{ °C}$  is caused by the nature of inductive heating of steel. At the Curie point, the permanent magnetism changes to induced magnetism. The effect is so intense that the automatic temperature regulation struggles.

Due to the nature of  $42\text{SiCrB}$  steel, only three characteristic curve styles are observed. At low cooling rates, a ferritic/pearlitic phase transformation and at fast cooling rates an athermal martensitic reaction is noted. In between, represented by  $2\text{ Ks}^{-1}$  cooling rate both reactions are combined, while the bainitic reaction is nearly suppressed.

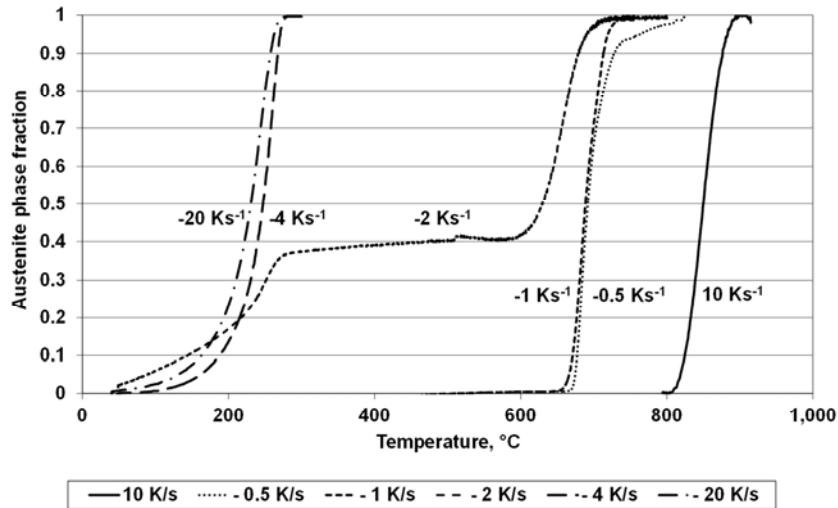


Figure 59: Calculated austenite phase fraction from dilatometric data plotted for heating and different cooling rates

Using the dilatation data, the phase fraction of austenite is calculated using equation (13), cf. chapter 0. The results are shown in figure 59 and the final phase fractions are listed in table 8. As the ferrite and pearlite phase transformations are superimposed, the sum for both is given by dilatometry only.

Table 8: Phase fractions after continuous cooling estimated by dilatometry

	$20\text{ Ks}^{-1}$	$10\text{ Ks}^{-1}$	$4\text{ Ks}^{-1}$	$2\text{ Ks}^{-1}$	$1\text{ Ks}^{-1}$	$0.5\text{ Ks}^{-1}$
Ferrite	0	0	0	0.6	1	1
Pearlite						
Bainite	0	0	0	0.05	0	0
Martensite	1	1	1	0.35	0	0

Furthermore, the diagram data is used to find temperatures representing the start and finish of the phase transformations, respectively phase fractions of 0.01 and 0.99. The phase transformation temperatures during heating  $A_{c1}$  and  $A_{c3}$  and the martensite start  $M_s$  and finish  $M_f$  temperature are documented in table 9.

Table 9: Transformation temperatures  $A_{c1}$ ,  $A_{c2}$  and  $A_{c3}$  for  $10 \text{ Ks}^{-1}$  heating and  $M_s$  and  $M_f$  for  $10 \text{ Ks}^{-1}$ ,  $20 \text{ Ks}^{-1}$  and  $40 \text{ Ks}^{-1}$  cooling

Experiment	$A_{c1}$	$A_{c2}$	$A_{c3}$	$M_s$	$M_f$
$40 \text{ Ks}^{-1}$	810	734	896	258	40
$20 \text{ Ks}^{-1}$	810	735	893	268	61
$10 \text{ Ks}^{-1}$	817	732	903	285	55
Mean	812	734	897	270	52

For comparison metallography is used as well to determine the final phase fractions. The micrographs of all samples are shown in appendix E for better readability. Table 10 contains the estimations of phase fractions from metallography.

Table 10: Phase fractions after continuous cooling estimated by light microscopy

	$20 \text{ Ks}^{-1}$	$10 \text{ Ks}^{-1}$	$4 \text{ Ks}^{-1}$	$2 \text{ Ks}^{-1}$	$1 \text{ Ks}^{-1}$	$0.5 \text{ Ks}^{-1}$
Ferrite	0	0	0.01	0.03	0.03	0.04
Pearlite	0	0	0.05	0.6	0.97	0.96
Bainite	0	0	0.01	0.01	0	0
Martensite	1	1	0.93	0.36	0	0

Overall the phase fractions calculated from dilatometric data and the metallographic observations are in good agreement. Although the dilatometric data of  $4 \text{ Ks}^{-1}$  does not show any phase transformations the presence of ferrite and pearlite is evident from metallography, cf. figure 60. Since metallography distinguishes ferrite and pearlite and is obviously more sensitive at low phase fractions, the corresponding results are used for the CCT diagram.

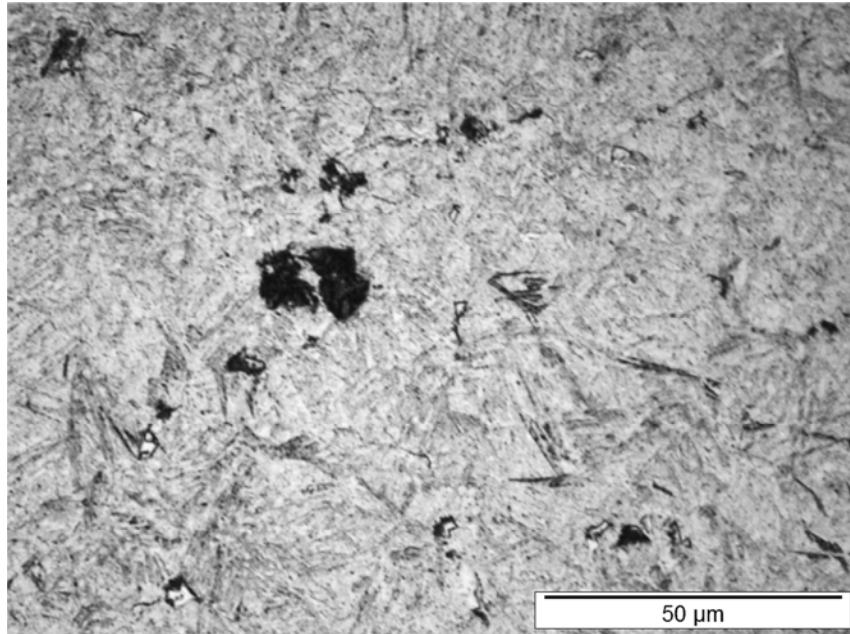


Figure 60: Light optical micrograph of  $42\text{SiCrB}$  steel after continuous quenching at  $4\text{ Ks}^{-1}$ , prepared with Nital etchant. The microstructure consists of martensitic matrix, black pearlite and microscopic white ferrite isles are visible as well

The Continuous Cooling Transformation diagram of  $42\text{SiCrB}$  steel is given in figure 61. Minor data points represent the results of the dilatometric investigation of transformation points and the numbers represent the amount of the present phase estimated from metallography. At the end of each continuous heat treatment curve, the Vicker's hardness is given.

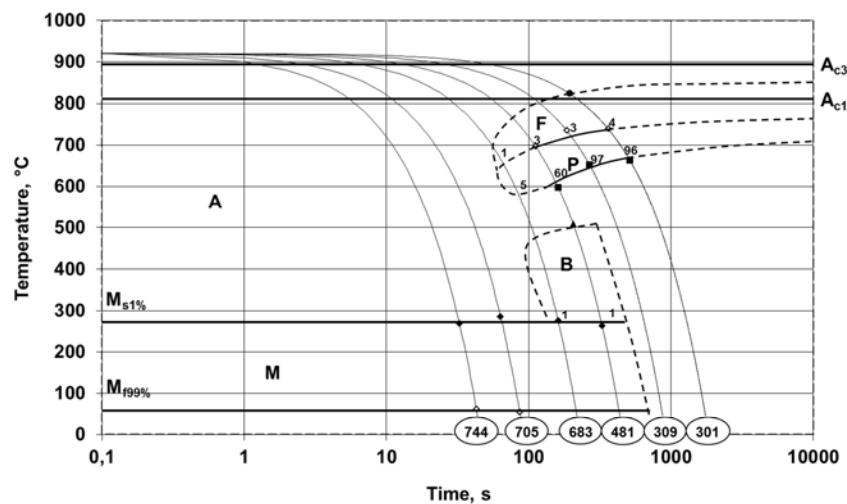


Figure 61: CCT diagram of  $42\text{SiCrB}$  steel with composition of 0.44 wt.% C, 1.9 wt.% Si, 0.64 wt.% Mn, 1.4 wt.% Cr, 0.046 wt.% Nb, 110 ppm N and 20 ppm B for cooling rates from 0.5 to 20  $\text{Ks}^{-1}$ , after austenitization at  $920\text{ }^\circ\text{C}$  for 300 s

Due to the high amount of chromium and carbon, the diffusion controlled phase transformations forming ferrite, pearlite and bainite are retarded remarkably. Cooling rates above  $10 \text{ Ks}^{-1}$  result in a fully martensitic microstructure. Bainite is only observed in very low amounts in the region between approximately 4 and  $2 \text{ Ks}^{-1}$  combined with emerging amounts of pearlite. At lower cooling rates, the  $42\text{SiCrB}$  steel forms a nearly fully pearlitic microstructure.

The changes in length during isothermal heat treatments after austenitization are shown in figure 62. To receive comparable information for the start time of phase transformations time measurement commences when the sample temperature reaches the designated value. The length offset is chosen at a stable state, approximately at 20 s, to remove slight regulation instabilities due to very fast cooling and heating.

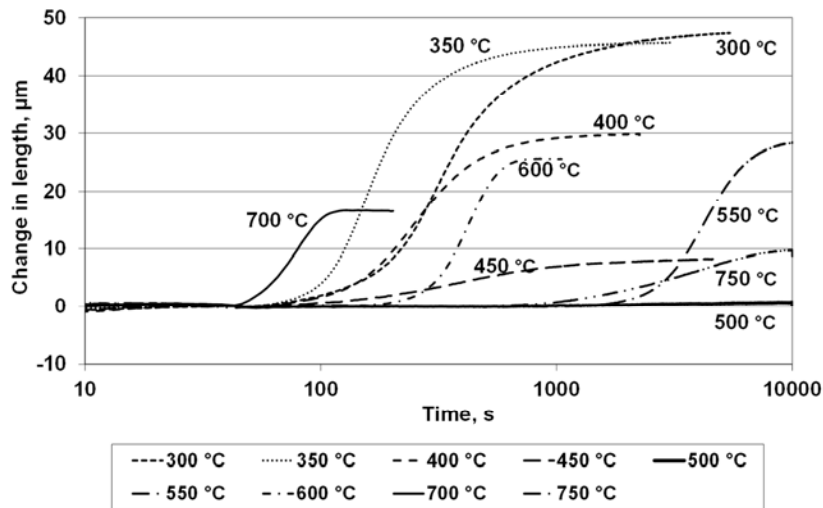


Figure 62: Dilatation versus time during isothermal holding at different temperatures between 300 °C and 750 °C, characterizing the phase transformation behavior of  $42\text{SiCrB}$  steel

In general, the total volume increase during austenite to ferrite phase transformations is temperature dependent. Due to the different thermal expansion coefficients the difference between both becomes larger with decreasing transformation temperature. Except in the range of 450 °C to 550 °C the dilatation curves follow this behavior.

To obtain the phase transformation start and finishing times, the resulting ferrite or bainite phase fractions are calculated in figure 63 from the changes in length, as described by equation (14).

The change in phase fraction is utilized to find reproducible and comparable values for the beginning and end of the isothermal process, respectively 0.05 and 0.95 ferrite or bainite phase fraction.

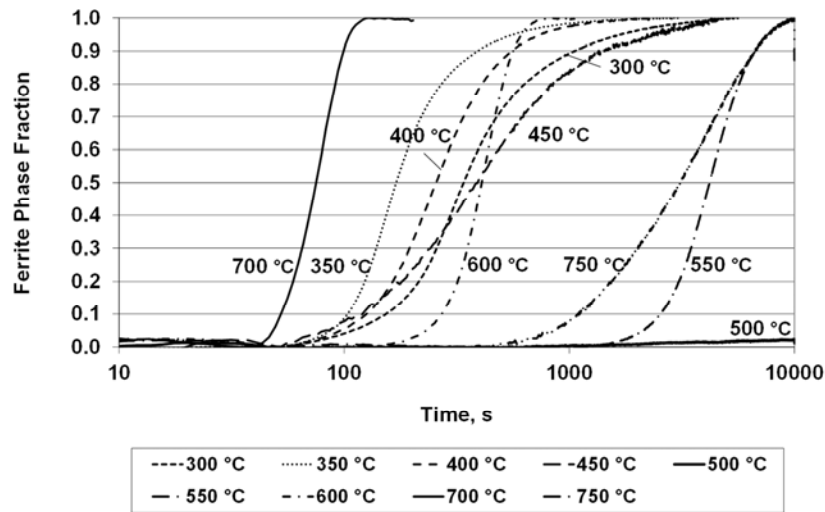


Figure 63: Transformed phase fraction vs. time during isothermal heat treatment after full austenitization at 950 °C for 300 s

Figure 64 summarizes the isothermal transformation behavior of 42SiCrB steel.  $A_{C1}$ ,  $A_{C3}$  and  $M_s$  Temperature are taken according to the definition from continuous experiments. Similar to the continuous cooling transformation diagram the ferrite, pearlite and bainite reactions are retarded distinctly by alloying elements. Nevertheless, the fastest condition for a ferrite/pearlite microstructure is around 700 °C and for the bainitic phase transformation at 400 °C. At higher temperatures, the necessary undercooling for the nucleation is missing while at lower temperatures the growth is limited by lower diffusion, which forms the typical C-shape curves. In between, an incomplete phase transformation phenomenon is observed.

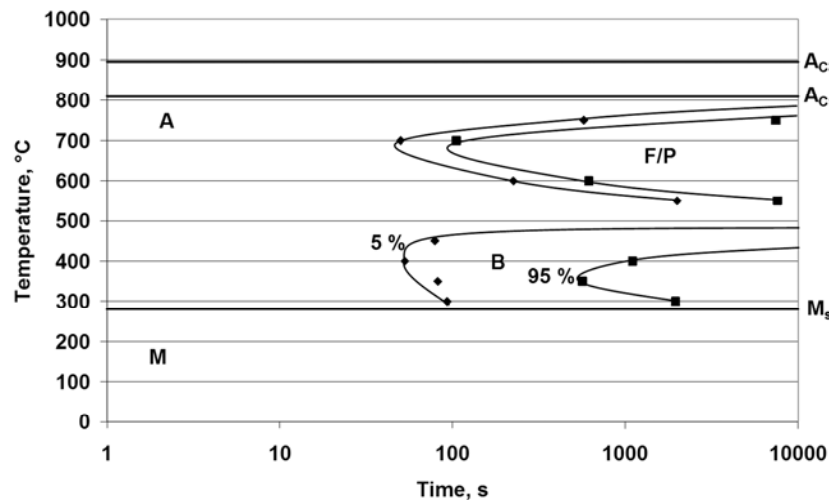


Figure 64: TTT diagram of 42SiCrB steel with composition of 0.44 wt.% C, 1.9 wt.% Si, 0.64 wt.% Mn, 1.4 wt.% Cr, 0.046 wt.% Nb, 110 ppm N and 20 ppm B for temperatures between 300 and 750 °C after austenitization at 920 °C for 300 s



## 6.2. Dilatometry of Quenching and Partitioning

The dilatometric response of  $42\text{SiCrB}$  steel during One-step and Two-step Quenching and Partitioning at different quenching temperatures, partitioning temperatures and partitioning times is presented next. Furthermore the dilatations caused by tempering of the martensitic matrix are measured at the end of this chapter.

### 6.2.1. One-step Quenching and Partitioning

Since we focus on the behavior during Quenching and Partitioning and not in austenitization of the following plots commences if martensite start temperature is achieved. If the reader is interested in preceded data please take a look to figure 58, it is always the same in this study.

As the partitioning time is varied at  $200\text{ }^\circ\text{C}$  between  $100\text{ s}$  and  $30,000\text{ s}$ , cf. figure 65, the isothermal lengthening of the sample is observed and increases with partitioning time. Furthermore, a second subsequent athermal martensitic phase transformation is observed by an additional increase in length. The corresponding second martensite start temperature is lowered with increasing the holding time, but the lengthening effect is also reduced. At  $30,000\text{ s}$ , no secondary martensite formation above room temperature is observed.

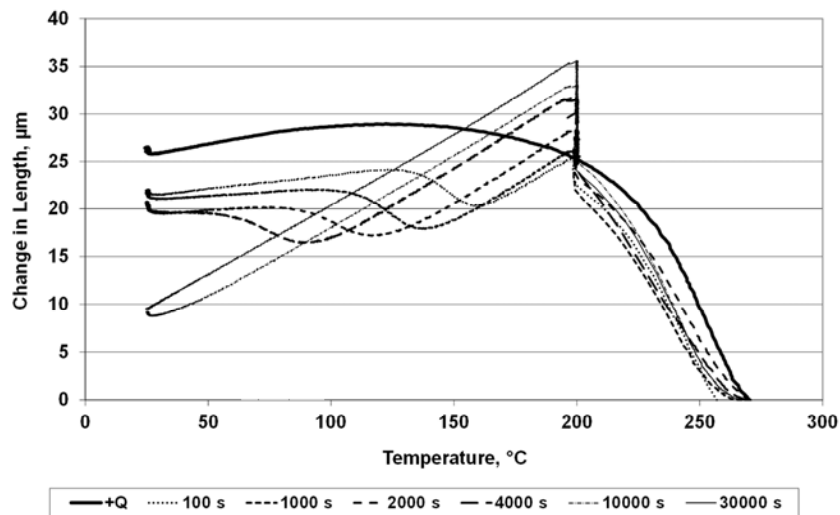


Figure 65: Change in length during one-step Quenching and Partitioning at  $200\text{ }^\circ\text{C}$  of  $42\text{SiCrB}$  steel for partitioning times from  $100\text{ s}$  to  $30,000\text{ s}$  compared to full quenching (+Q)

The dilatometric response of  $42\text{SiCrB}$  steel during One-step Quenching and Partitioning at different quenching temperatures is presented in figure 66 for a constant partitioning time of  $1,000\text{ s}$ . During isothermal partitioning, the sample length is increasing as well. The effect is reduced as the quenching and partitioning temperature are also reduced. The second martensite start temperature is decreasing with decreasing quenching and partitioning temperature, except at the highest temperature of  $225\text{ }^\circ\text{C}$ .

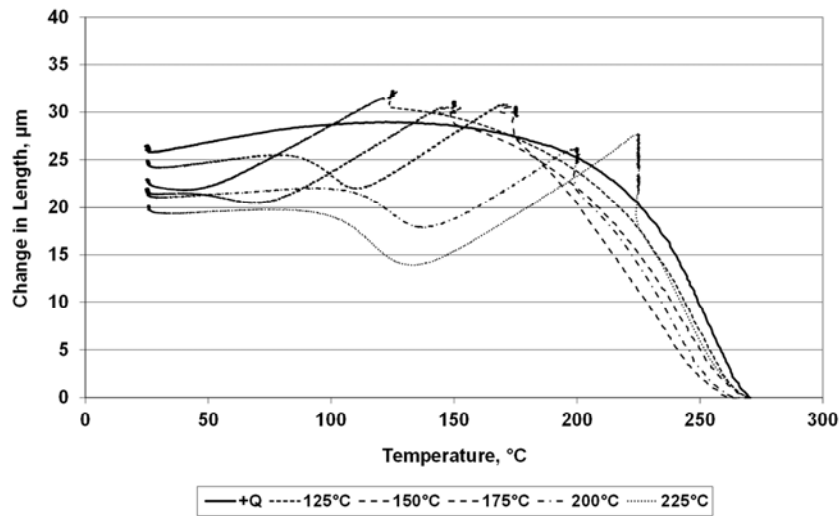


Figure 66: Dilatometric response of  $42\text{SiCrB}$  steel on one-step Quenching and Partitioning at temperatures ranging from 125  $^{\circ}\text{C}$  to 225  $^{\circ}\text{C}$  for 1,000 s compared to full quenching (+Q)

Figure 67 shows the change in length vs. time in One-step Quenching and Partitioning experiments ranging from 175  $^{\circ}\text{C}$  to 275  $^{\circ}\text{C}$  and the bainitic reaction at 300  $^{\circ}\text{C}$  taken from the preceding TTT experiments for comparison.

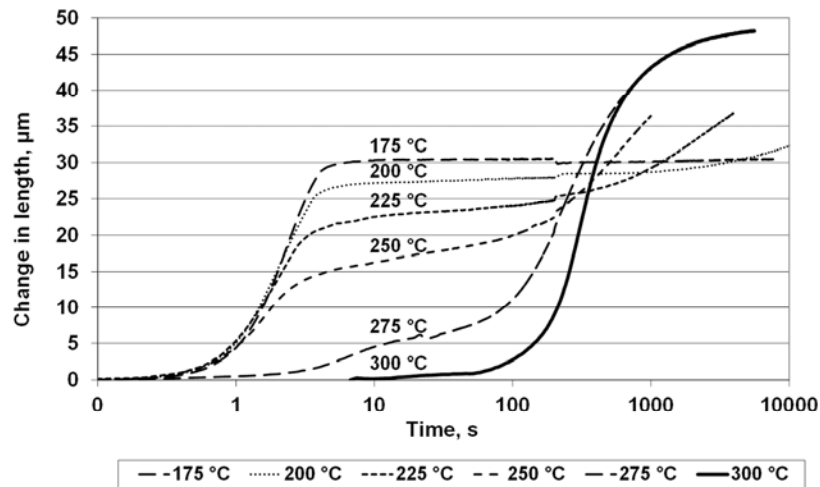


Figure 67: Change in length vs. time during one-step Quenching and Partitioning at temperatures between 175  $^{\circ}\text{C}$  and 275  $^{\circ}\text{C}$  compared to bainitic reaction at 300  $^{\circ}\text{C}$

While the nearly fully martensitic phase transformation at 175  $^{\circ}\text{C}$  and the fully bainitic phase transformation at 300  $^{\circ}\text{C}$  are characterized by one sigmoidal-shaped curve, the temperatures in between appear to be a compound, pieced together from both reactions. At low temperatures, the martensitic phase transformation is dominant while with increasing temperatures bainite gains control. Especially at 275  $^{\circ}\text{C}$ , the double sigmoidal curve is evident. Athermal martensite formation stops after 20 s and

afterwards a bainitic phase transformation below  $M_s$ , with very similar kinetics to the 300 °C curve is observed.

### 6.2.2. Two-step Quenching and Partitioning

The results of the dilatometric two-step Quenching and Partitioning heat treatments are presented next. Increasing the partitioning temperature in 50 K steps from 300 °C to 600 °C, after Quenching to 170 °C, results in various response of the length, as shown in figure 68.

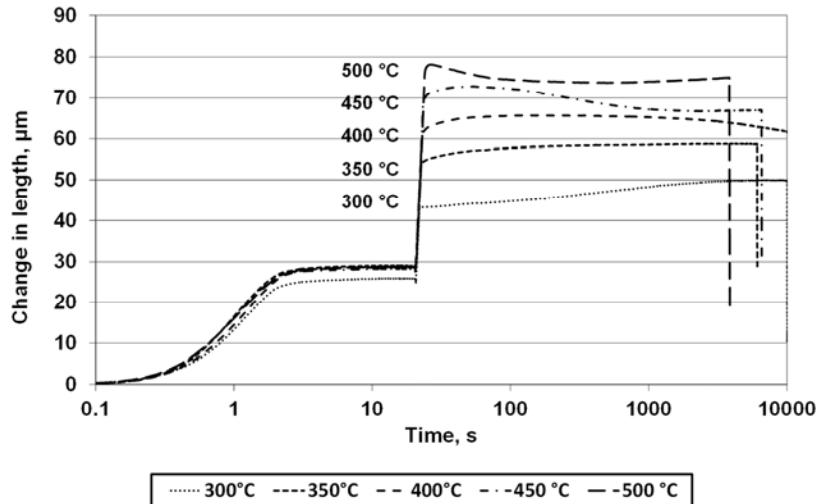


Figure 68: Influence of partitioning temperature on the change in length over time during two-step Quenching and Partitioning after quenching to 170 °C

At 300 °C partitioning temperature, a sigmoidal-shaped curve is observed. The total increase in length is about 7 μm and achieved after a long time period of 5,000 s. Between 350 °C and 500 °C the length increases by up to 5 μm starting directly in the beginning of the partitioning phase. The maximum is achieved after 1,000 s at 350 °C, 100 s at 400 °C, 30 s at 450 °C and 2 s at 500 °C, in other words faster with an increasing temperature. In the cases of 400 °C and 450 °C and 500 °C a decrease in length after reaching the maximum is observed. At 400 °C 3 μm are lost after 10,000 s when the experiment ends. In the case of 450 °C and 500 °C 6 μm are lost and the reaction stops during the experimental time. It takes 2,100 s in the first and 450 s in the second case.

Furthermore, the quenching temperature is varied at constant partitioning temperature of 400 °C and combined with sub-zero experiments to analyze the low temperature stability of the retained austenite. In Figure 69, the results are compared to full quenching and it is evident, that no secondary martensite forms after quenching down to -100 °C; neither at 230 °C nor at 170 °C quenching temperature. During partitioning at 400 °C, after quenching to 170 °C, 3 μm lengthening is observed, after quenching to 230 °C about 10 μm.

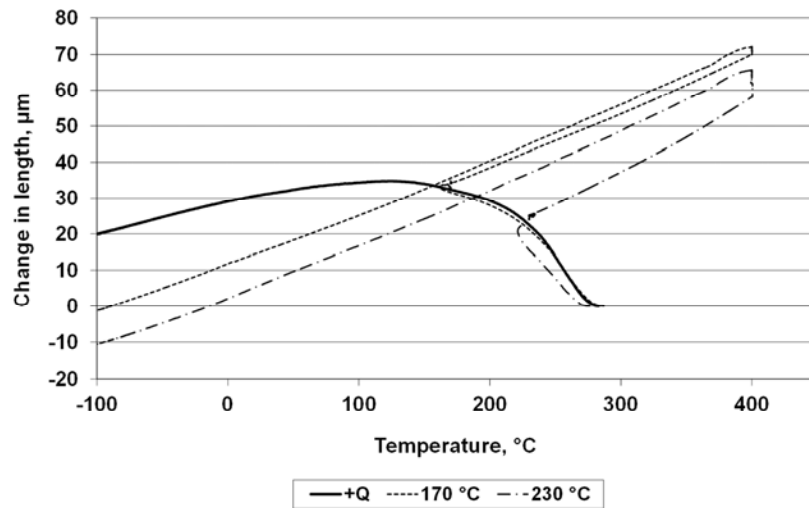


Figure 69: Dilatometric response of two-step Quenching and Partitioning in sub-zero experiments compared with full quenching (+Q)

### 6.2.3. Tempering of Martensite

The changes in length associated with continuous tempering of martensite are displayed in figure 70.

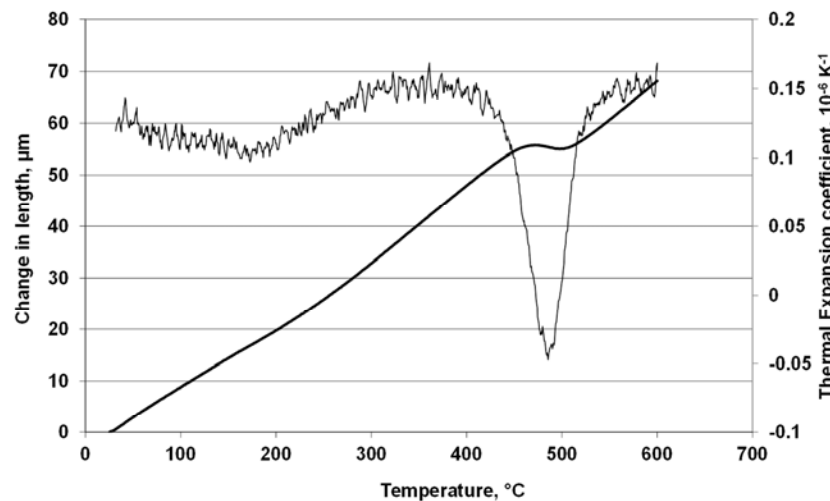


Figure 70: Change in length of  $42\text{SiCrB}$  steel caused by slow heating at  $1\text{ K s}^{-1}$ , respectively tempering at various temperatures

The behavior of  $42\text{SiCrB}$  steel during tempering is common by use of the means of conventional three stages tempering of martensite. Experiments by Eduard Houdremont with plain carbon steels show a small contraction between  $100\text{ °C}$  and  $200\text{ °C}$  caused by precipitation of carbon from martensite, also known as 1<sup>st</sup> stage of tempering. This is followed by lengthening due to decomposition of retained austenite into ferrite and cementite in the 2<sup>nd</sup> stage of tempering between  $200\text{ °C}$  and  $300\text{ °C}$ . Finally, in the 3<sup>rd</sup> stage of tempering shrinking is observed again while cementite

forms. The intensity of these effects is found to increase with carbon content. [Houdremont1956]

All three stages are observed during the tempering of  $42\text{SiCrB}$  steel as well. The corresponding temperature ranges of the 2<sup>nd</sup> and 3<sup>rd</sup> stage are shifted by approximately 100 °C to higher temperatures. This may be caused by faster heating or due to the high amounts of silicon affecting the stability of retained austenite and the cementite precipitation kinetics, as already described in chapter 5.3. As the heating rate is not published in the work of Eduard Houdremont its influence is an additional admissible hypothesis.

### 6.3. In-Situ X-Ray Diffraction

Already mentioned in chapter 7.1 the change in length is ambiguous. This is the reason to take a closer look to the behavior during partitioning. The results of in-situ X-ray diffraction during one- and two-step Quenching and Partitioning experiments are shown in this chapter. For comparison, a Quenching and Tempering heat treatment is investigated as well.

Black horizontal lines in the overview graph represent diffraction intensities for the considered diffraction angles versus time. The corresponding heat treatment is given on the secondary axis. The intensities of all experiments are plotted on a decadic logarithmic scale.

Furthermore, the in-situ experiments are analyzed by means of the peak positions and intensities to measure retained austenite volume fraction, lattice parameters and carbon content of the austenite, as described in chapter 4.4.

#### 6.3.1. One-step Quenching and Partitioning

The first experiment is shown in figure 71. It shows one-step Quenching and Partitioning at 200 °C of  $42\text{SiCrB}$  steel examined by 100 keV synchrotron in-situ X-ray diffraction.

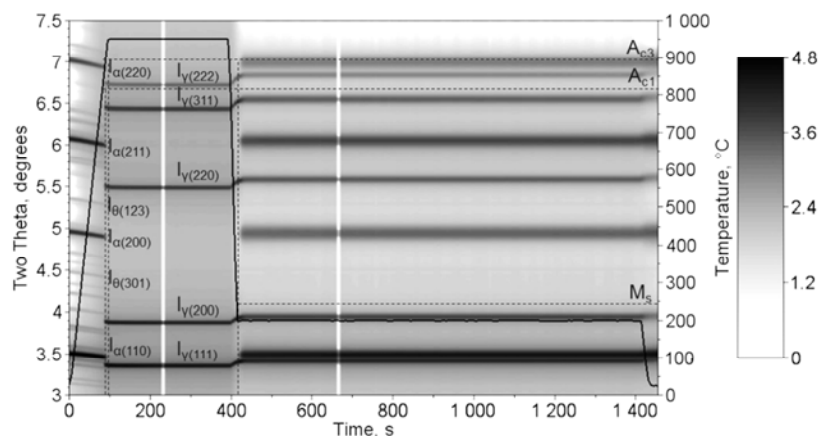


Figure 71: In-situ X-ray diffraction experiments on  $42\text{SiCrB}$  steel during One-step Quenching and Partitioning. Intensities are plotted in decadic logarithm. Partitioning is carried out at 200 °C

The graphically determined  $Ac_1$  and  $Ac_3$  temperatures are in relevant agreement to the dilatometric measurements given in table 9, respectively  $812^\circ\text{C}$  and  $897^\circ\text{C}$ , and the dilatation data measured simultaneously, cf. figure 72. In the case of the PETRA III measurements combined with the BÄHR DIL 805 dilatometer the martensite start temperature is near to the value of  $256^\circ\text{C}$ , determined by dilatometry. This ensures that the real sample temperature is described by the thermocouple data throughout the heat treatment.

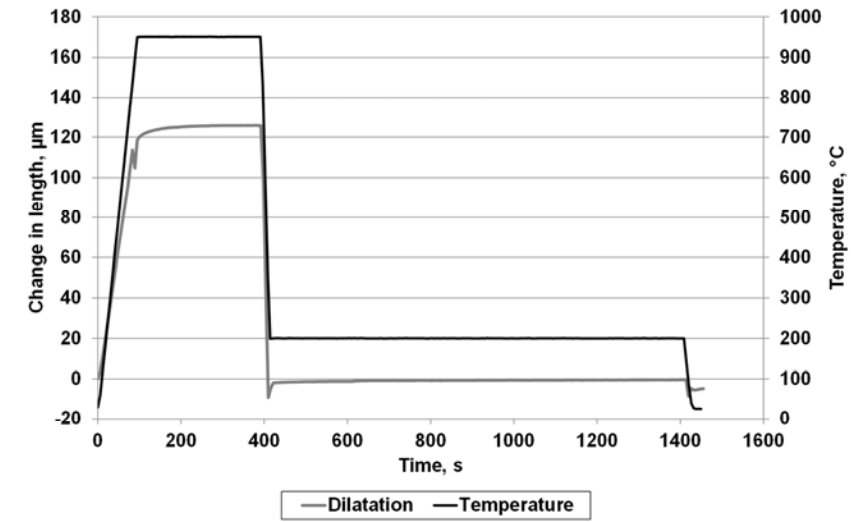


Figure 72: Dilatation during one-step Quenching and Partitioning at  $200^\circ\text{C}$  measured simultaneously with in-situ X-ray diffraction

Sharp cementite intensities from the initial microstructure are visible before austenitization in the synchrotron experiments in figure 71. The cementite intensities  $I_{0(301)}$  at  $4.474^\circ$  and  $I_{0(123)}$  at  $5.348^\circ$  lines are designated for better readability only, because in total 92 cementite intensities exist in this  $2\Theta$  range for 100 keV synchrotron radiation, respectively 0,0124 nm wavelength. The corresponding data is calculated using POWDER CELL software [Kraus1996] [Kraus2000] to ensure the peaks belong to cementite. Furthermore, very weak cementite intensities are present during and after austenitization as well. The designated cementite intensities are slightly visible between the dominant austenite and ferrite intensities. It is apparent from the synchrotron experiments that cementite is not dissolved completely during the austenitization.

At  $10\text{ Ks}^{-1}$  heating rate the transformation of ferrite to austenite lasts below 10 s, since there is only one XRD image present in the two phase region at a sampling time of 3 s. The difference in the austenite volume fraction determined by dilatometry compared to XRD is smaller than 5% in this case.

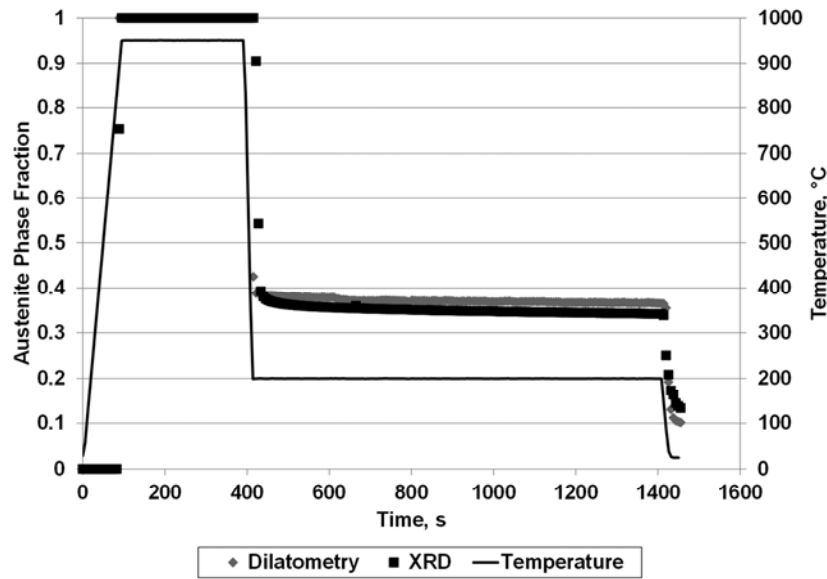


Figure 73: Change in the austenite phase fraction during One-step Quenching and Partitioning heat treatment of  $42\text{SiCrB}$  steel determined by dilatometry and in-situ XRD. Partitioning is carried out at  $200\text{ }^{\circ}\text{C}$

During the quenching a martensitic transformation is observed consuming 60 % of the austenite immediately, cf. figure 73. Afterwards, the slight decrease of 5 % in the austenite volume fraction during the partitioning phase at  $200\text{ }^{\circ}\text{C}$  indicates that bainite formation occurs during the one-step partitioning phase as well.

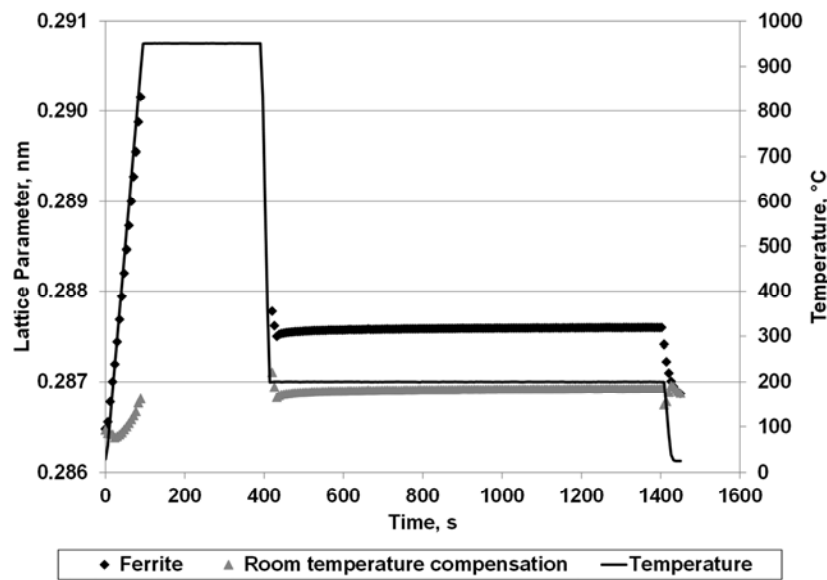


Figure 74: Change in the ferrite lattice parameter during One-step Quenching and Partitioning heat treatment of  $42\text{SiCrB}$  steel determined by XRD

The ferrite lattice parameter, analyzed in figure 74, is directly related to the temperature profile. The martensite lattice parameter after quenching is 0.005 nm higher than the lattice parameter of ferrite. During the partitioning phase no changes are observed.

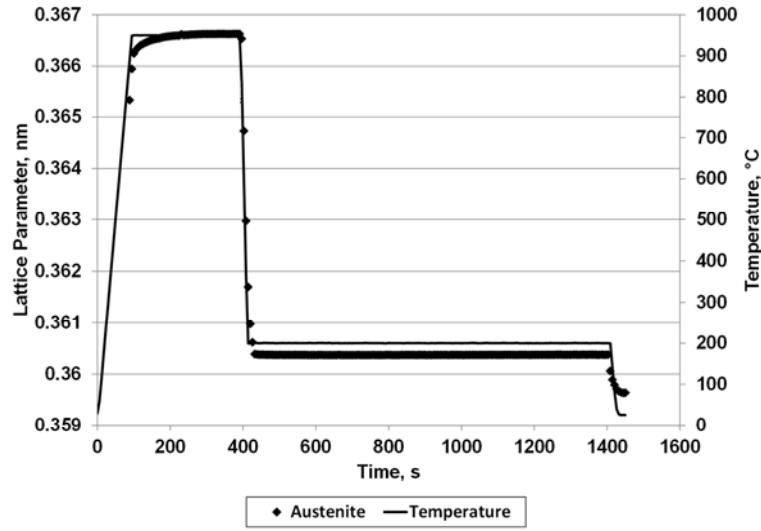


Figure 75: Change in the austenite lattice parameter during One-step Quenching and Partitioning heat treatment of  $42\text{SiCrB}$  steel determined by XRD

In general, the austenite lattice parameter, cf. figure 75, is directly proportional to the temperature. At second glance, two anomalous changes can be observed. At first, the length is increasing during the austenitization phase while the temperature is constant. Secondly, the lattice parameter conspicuously decreases less than expected during the final quenching to room temperature when additional martensite forms.

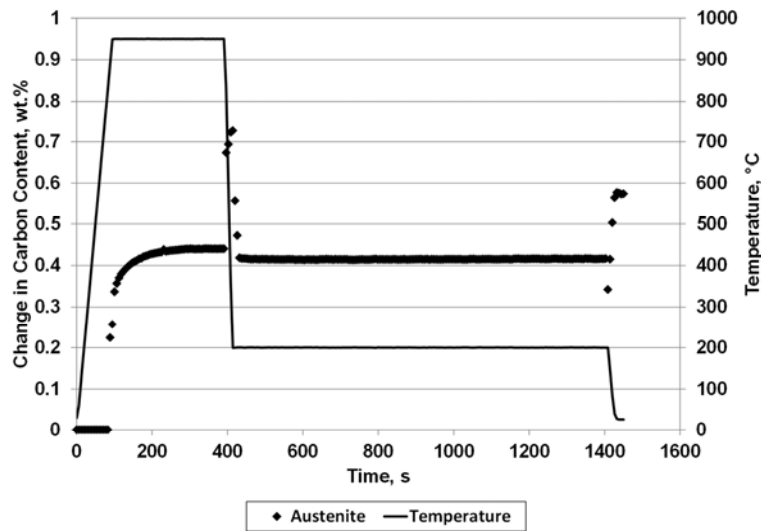


Figure 76: Change in austenite carbon concentration during One-step Quenching and Partitioning of  $42\text{SiCrB}$  steel derived from lattice parameter and temperature



The dissolution of cementite from the ferritic/pearlitic initial microstructure during the austenitization phase between 100 s and 400 s in figure 76 is clearly detailed. Even if the qualitative confirmation of cementite after austenitization has been determined, cf. the weak cementite intensities in figure 71, the asymptotic convergence to the horizontal line indicates a nearly full dissolution of carbon in the austenite.

The increase in solute carbon has an impact on the lattice parameter; a change in length in the dilatometry is observable as well. This means the dissolution of cementite can be observed by dilatometric investigations.

In contrast to our expectations, no significant carbon partitioning is observed in the XRD data during the isothermal holding phase, lasting 1,000 s, in one-step Quenching and Partitioning at 200 °C.

### 6.3.2. Two-step Quenching and Partitioning

The following two-step Quenching and Partitioning in-situ experiments are carried out on the SEIFERT SUN XRD fast in-situ X-ray diffractometer. Two different partitioning temperatures, precisely 400 °C and 475 °C are taken into account after quenching to 170°C.

The results of 400 °C partitioning are presented in figure 77. The two white horizontal stripes from two-theta 62° to 65° and 79° to 83° are blind zones between the three METEOR1D detector panels, which are positioned to the areas with significant intensities.

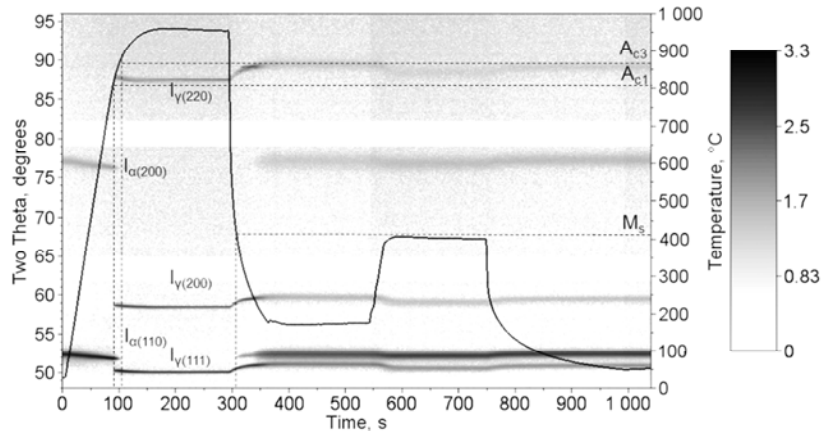


Figure 77: Overview of in-situ X-ray diffraction experiments on  $42\text{SiCrB}$  steel during Two-step Quenching and Partitioning heat treatment. Intensities are plotted in decadic logarithm. Partitioning is carried out at 400 °C

The graphically determined  $A_{c1}$  and  $A_{c3}$  temperatures of the fast-in-situ experiment on two-step Quenching and Partitioning shown in figure 77 correspond to the dilatometric measurements given in table 9. This ensures that the real sample temperature is accurately described by the thermocouple data during isothermal phases within the heat treatment. Compared to PETRA III results it is clear the graphically determined martensite start temperature is about 150 °C higher than

expected from the dilatometric results. This indicates the authentic surface temperature, where the XRD measurement takes place, is much lower during quenching compared to the thermocouple data.

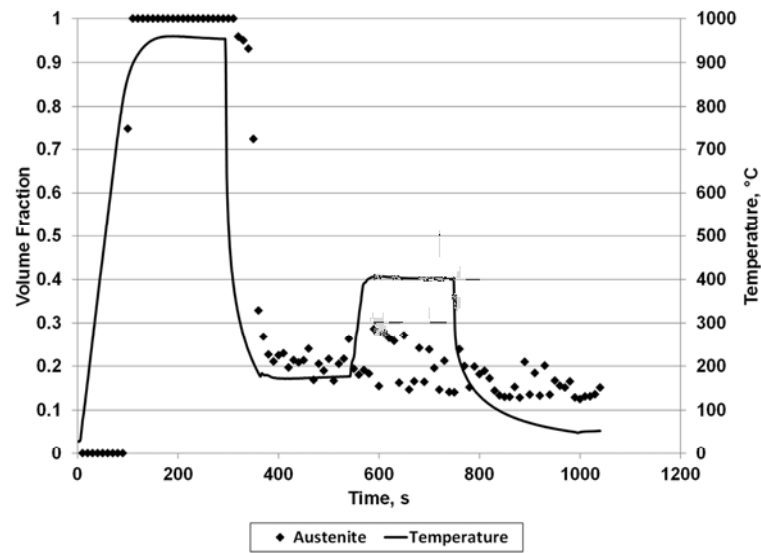


Figure 78: Change in the austenite phase fraction during Two-step Quenching and Partitioning heat treatment of  $42\text{SiCrB}$  steel determined by dilatometry and in-situ XRD. Partitioning is carried out at  $400\text{ }^{\circ}\text{C}$

The amount of retained austenite is more stable after two-step Quenching and Partitioning, cf. figure 78, compared to the one-step experiment, although at least 5 % is lost after Partitioning and cooling to room temperature.

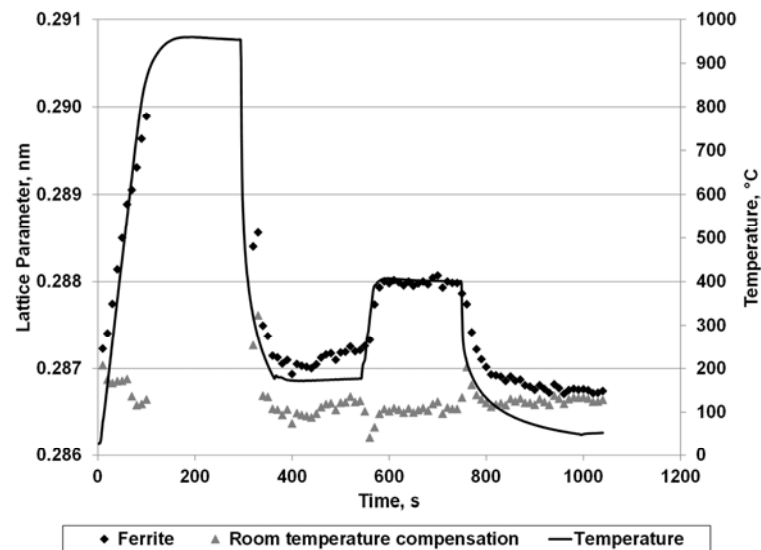


Figure 79: Ferrite lattice parameter during Two-step Quenching and Partitioning heat treatment of  $42\text{SiCrB}$  steel determined by XRD. Additionally, the corresponding room temperature lattice parameter is calculated. Partitioning is carried out at  $400\text{ }^{\circ}\text{C}$

The ferrite lattice parameter during the two-step Quenching and Partitioning heat treatment is determined from the X-ray intensities and shown in figure 79. Furthermore, temperature compensation is applied to the data to check for exceptional behavior, but the martensite lattice parameter remains constant at room temperature.

The associated austenite lattice parameter is determined and presented in figure 80. Similar to the One-step Quenching and Partitioning in-situ results the lattice parameter changes proportionally to the temperature in general. In detail, there is a disproportional higher increase in the lattice parameter within the ramp up from quenching at 170 °C to partitioning temperature of 400 °C and during cooling to room temperature.

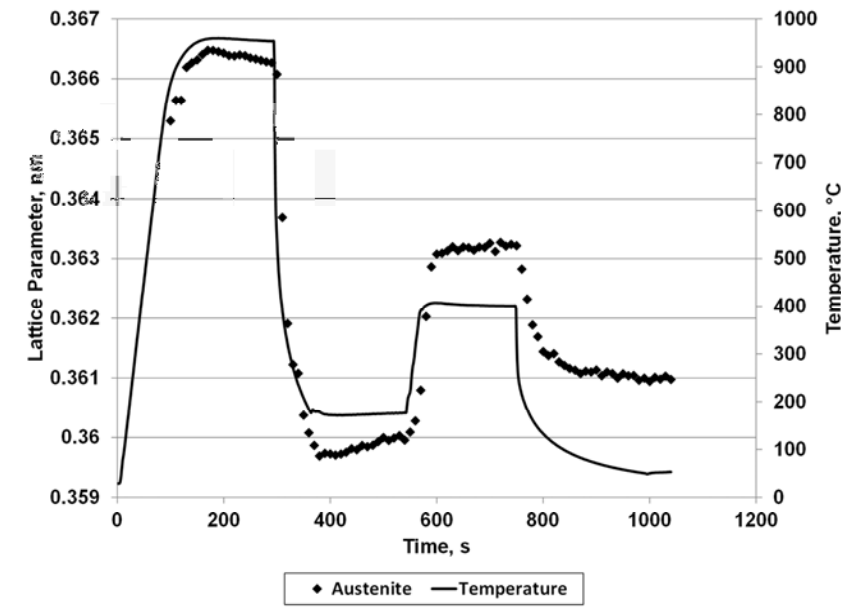


Figure 80: Change in the austenite lattice parameter during Two-step Quenching and Partitioning heat treatment of 42SiCrB steel determined by XRD. Partitioning is carried out at 400 °C

The large increase of the lattice parameter during reheating to partitioning temperature results in significant increase of the carbon content in the austenite, as shown in figure 81, obtained from the relationship described by Ichiro Seki and Kazuhiro Nagata [Sekiz005]. During the isothermal partitioning phase itself, only a slight increase of the carbon concentration is observed. Finally, during quenching to room temperature the calculated carbon content of austenite increases unexpectedly again.

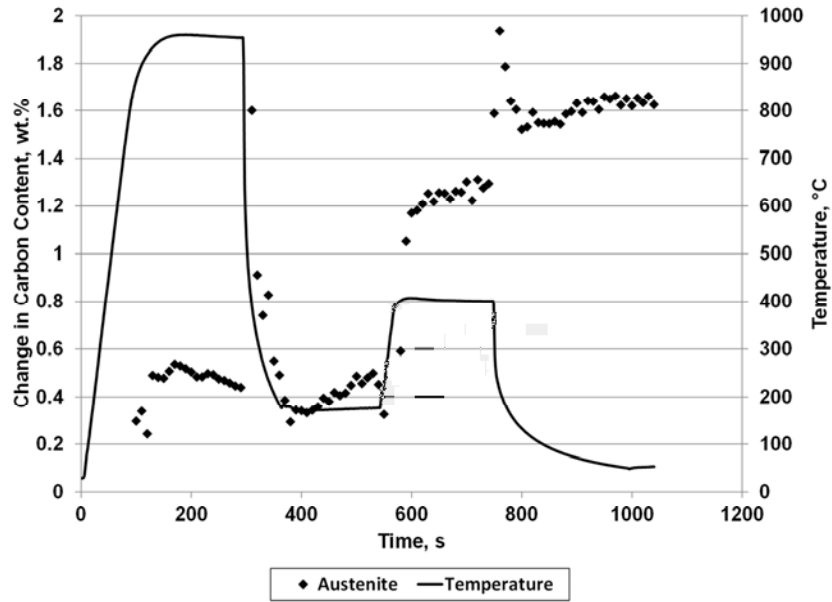


Figure 81: Change in austenite carbon concentration during two-step Quenching and Partitioning of  $42\text{SiCrB}$  steel derived from lattice parameter and temperature. Partitioning is carried out at  $400\text{ }^\circ\text{C}$

In the second part of this chapter, the results of  $475\text{ }^\circ\text{C}$  partitioning after quenching to  $170\text{ }^\circ\text{C}$  are presented. It begins with the overview in figure 82. The results for  $475\text{ }^\circ\text{C}$  partitioning are in general very similar to the first two-step experiment.

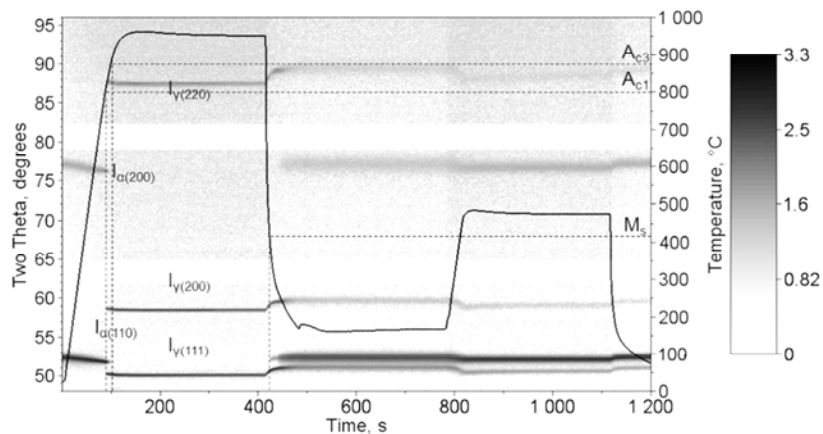


Figure 82: Overview of in-situ X-ray diffraction experiments on  $42\text{SiCrB}$  steel during Two-step Quenching and Partitioning heat treatment. Intensities are plotted in decadic logarithm. Partitioning is carried out at  $475\text{ }^\circ\text{C}$

Although there are differences present if the intensities are investigated more in detail, e.g. in the austenite volume fraction as shown in figure 83. It is clear that the retained austenite is decreasing by 0.1 during the partitioning. The ferrite lattice parameter is only proportional to the temperature, as shown in figure 84.

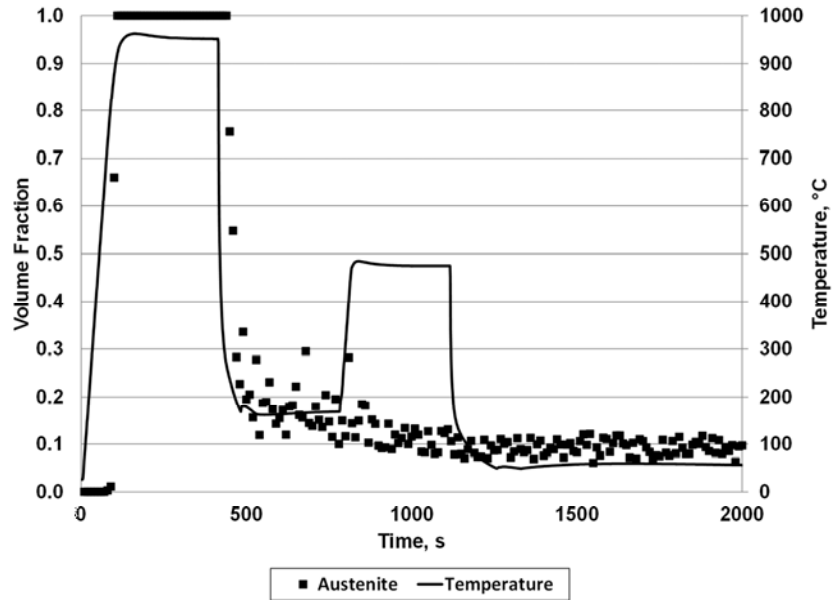


Figure 83: Changes in the austenite phase fraction during two-step Quenching and Partitioning heat treatment of  $42\text{SiCrB}$  steel determined by XRD. Partitioning is carried out at  $475\text{ }^{\circ}\text{C}$

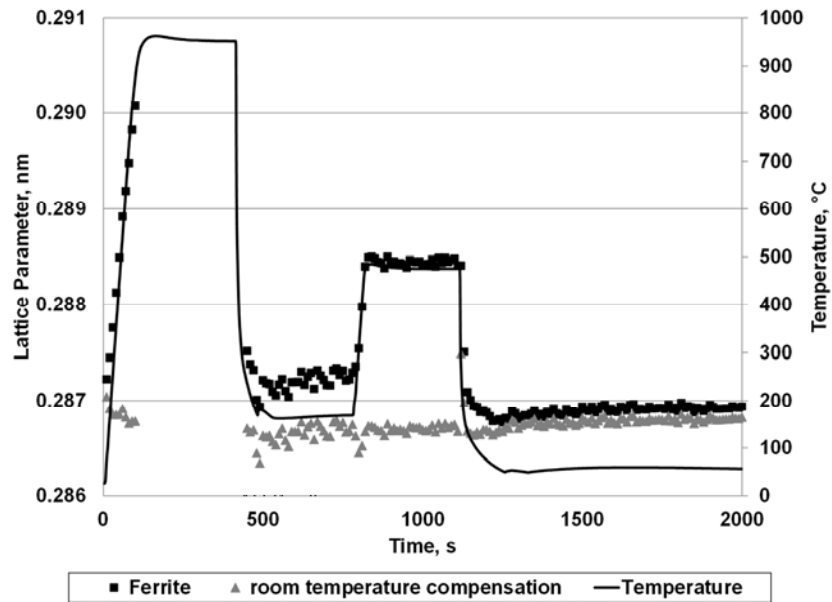


Figure 84: Ferrite lattice parameter during Two-step Quenching and Partitioning heat treatment of  $42\text{SiCrB}$  steel determined by XRD. Additionally, the corresponding room temperature lattice parameter is calculated. Partitioning is carried out at  $475\text{ }^{\circ}\text{C}$

The austenite lattice parameter and the corresponding austenite carbon content plotted in figure 85 and figure 86 perform differently. In both related cases, a disproportionate increase of the lattice parameter and thus for the carbon content during reheating to partitioning temperature is noted. In contrast to the partitioning

at 400 °C the lattice parameter and the carbon content start to decrease continuously when the partitioning temperature of 475 °C is achieved. Similar to the 400 °C experiment a slight increase is observed again during cooling to room temperature after 300 s partitioning or decarburization of austenite.

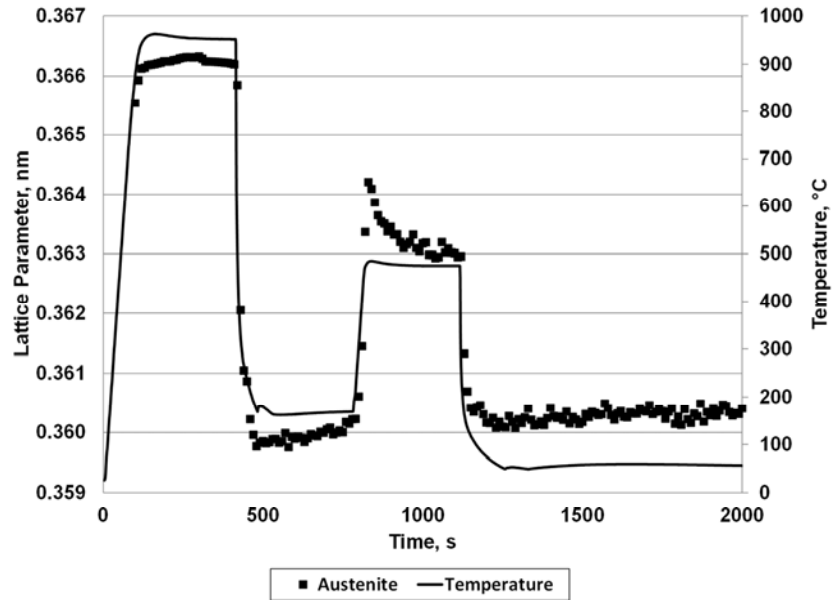


Figure 85: Change in the austenite lattice parameter during Two-step Quenching and Partitioning heat treatment of  $4_2\text{SiCrB}$  steel determined by XRD. Partitioning is carried out at 475 °C

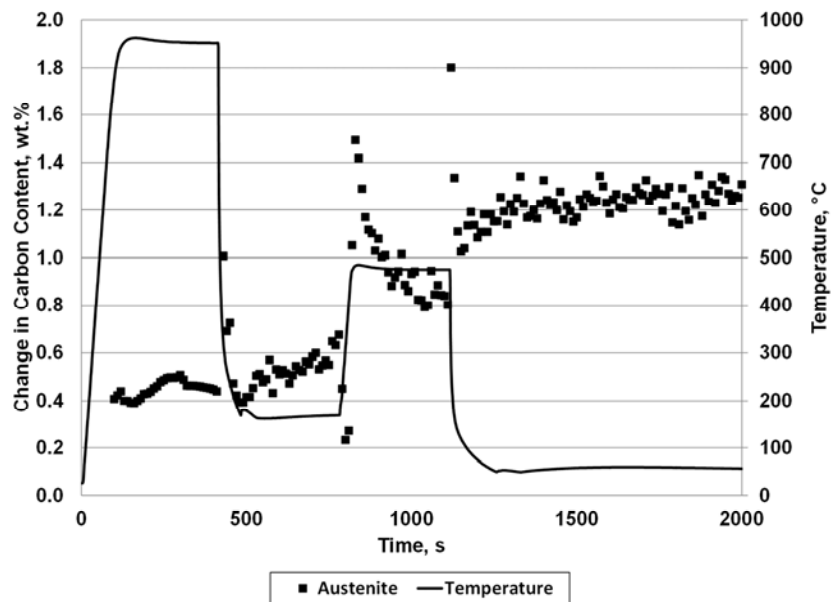


Figure 86: Change in austenite carbon concentration during two-step Quenching and Partitioning of  $4_2\text{SiCrB}$  steel derived from lattice parameter and temperature. The partitioning is carried out at 475 °C

### 6.3.3. Quenching and Tempering

Conclusively,  $42\text{SiCrB}$  steel is quenched to room temperature before tempering at  $475\text{ }^\circ\text{C}$  is carried out. The response of the SEIFERT SUN XRD fast in-situ X-ray diffractometer is given in figure 87.

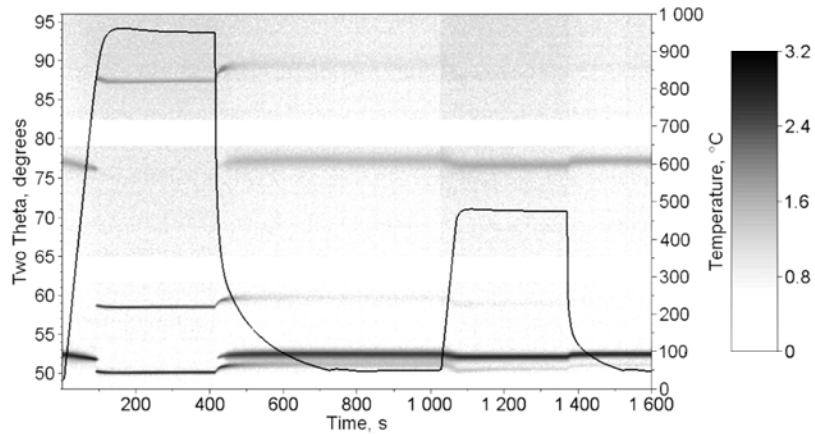


Figure 87: Overview of in-situ X-ray diffraction experiment on  $42\text{SiCrB}$  steel during Quenching and Tempering heat treatment. Intensities are plotted in decadic logarithm

After quenching to room temperature, 0.1 phase fraction of austenite is still retained, as depicted by the X-ray phase analysis in figure 88. During tempering, this austenite decomposes further and nearly no austenite is retained.

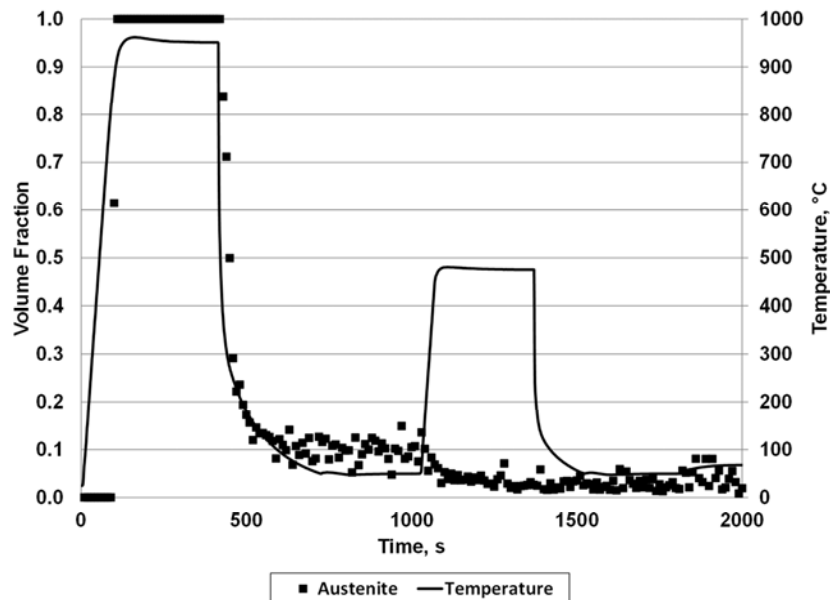


Figure 88: Change in the austenite phase fraction during Quenching and Tempering heat treatment of  $42\text{SiCrB}$  steel determined by XRD

Similar to all the in-situ X-ray diffraction experiments, the measured ferrite lattice parameter, cf. figure 89, is affected by thermal expansion exclusively.

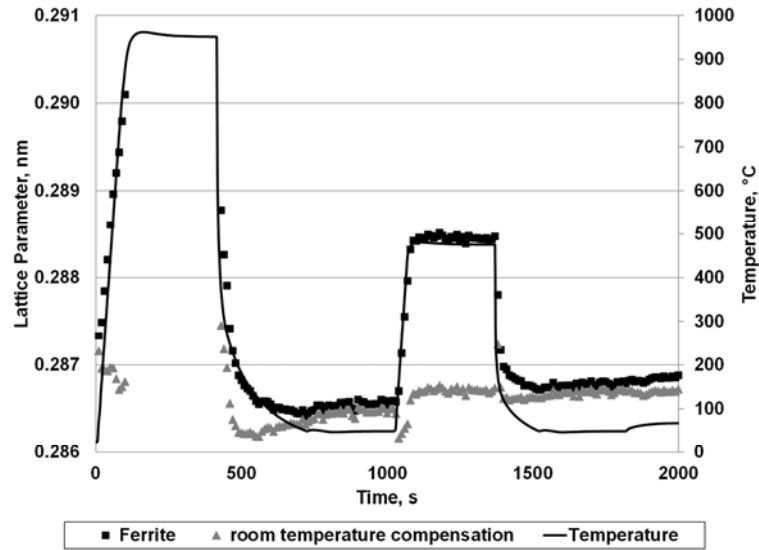


Figure 89: Ferrite lattice parameter during Quenching and Tempering heat treatment of  $4_2\text{SiCrB}$  steel determined by XRD. Additionally, the corresponding room temperature lattice parameter is also calculated

The measurement of the austenite lattice parameter becomes quite difficult if nearly no austenite is present. The very small austenite intensities lead to bad signal to noise ratio and it is difficult to determine the exact peak position. Accordingly, the following results in figure 90 and figure 91 show big scatter. Nevertheless, similar to the two-step Quenching and Partitioning experiments the austenite carbon content of the austenite increases rapidly and decreases with ongoing tempering.

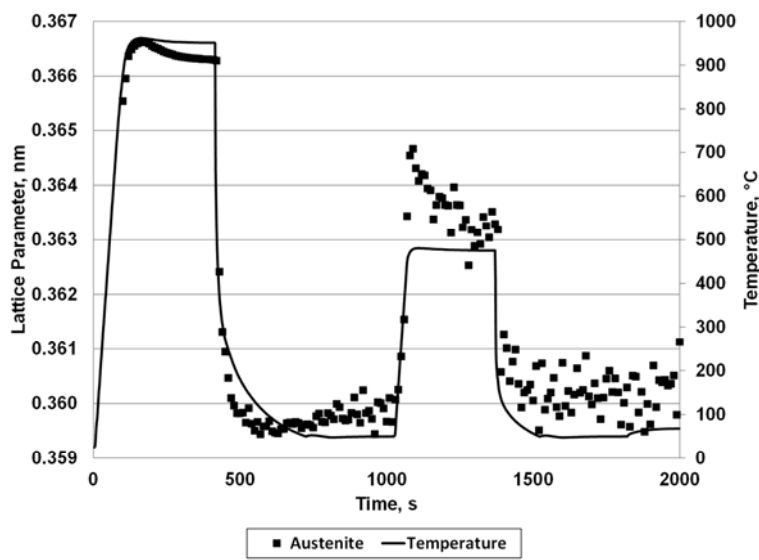


Figure 90: Change in the austenite lattice parameter during Quenching and Tempering heat treatment of  $4_2\text{SiCrB}$  steel determined by XRD



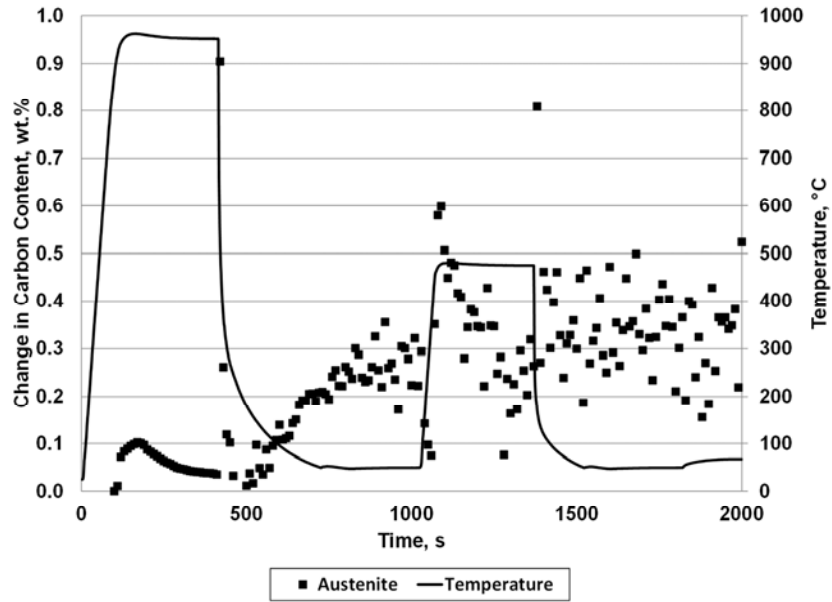


Figure 91: Change in austenite carbon concentration during Quenching and Tempering of  $42\text{SiCrB}$  steel derived from lattice parameter and temperature

## 6.4. Mechanical Properties

In the following section the results of tensile testing are presented. Various two-step Quenching and Partitioning heat treatments are evaluated as well as Quenching and Tempering at different temperatures for comparison purposes.

### 6.4.1. Two-step Quenching and Partitioning

In this case the partitioning temperature is set to  $475\text{ }^{\circ}\text{C}$  and partitioning time to 180 s. The quenching temperature is varied to find optimal temperatures regarding mechanical properties. In detail, the Constrained Carbon Equilibrium (CCE) model, cf. chapter 3.4 and in particular chapter 4.3.1, is used to predict a reasonable range of interest to keep the number of experiments manageable. This ranges from  $160\text{ }^{\circ}\text{C}$  to  $210\text{ }^{\circ}\text{C}$ . The measured temperatures versus time are presented in figure 92.

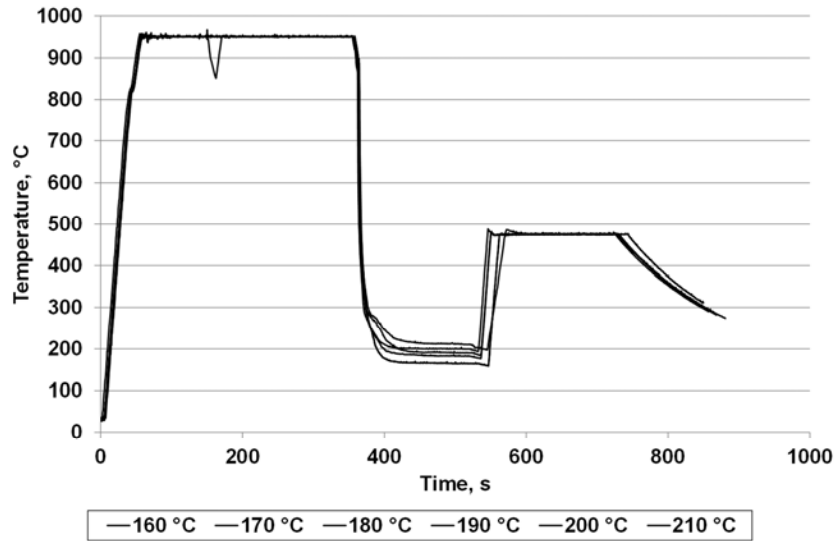


Figure 92: Thermocouple recordings of the two-step Quenching and Partitioning heat treatments

Although six different quenching temperatures are tested, only three stress-strain curves are drawn in figure 93. This is necessary for better legibility as the curves are very similar.

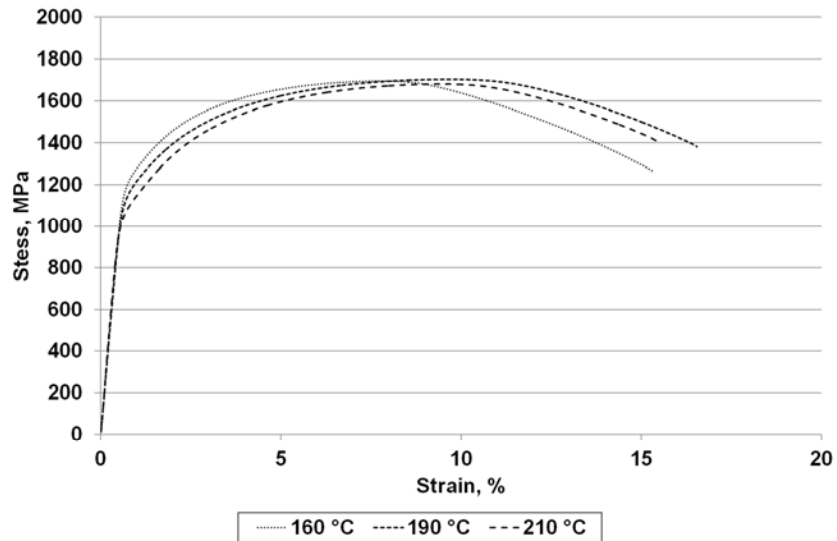


Figure 93: Selected stress strain curves of  $42\text{SiCrB}$  steel after two-step Quenching and Partitioning heat treatment

From the curves and the characteristic values, cf. table 11, it is clear that yield strength decreases from 1,200 MPa to 1,050 MPa with increasing quenching temperature, while tensile strength stays constant at 1,700 MPa. This results in decreasing yield ratio as well.

Table 11: Tensile testing results of 42SiCrB steel after two-step Quenching and Partitioning heat treatment

QT	R <sub>p0,2</sub>	R <sub>m</sub>	A <sub>g</sub>	A <sub>5</sub>	Z	R <sub>p0,2</sub> · A <sub>5</sub>	R <sub>m</sub> · A <sub>5</sub>
°C	MPa	MPa	%	%	%	MPa%	MPa%
210	1072	1681	9	16	41	17400	27200
200	1062	1704	9	16	46	17200	27600
190	1161	1703	9	16	44	18600	27300
180	1132	1709	8	16	44	17700	26700
170	1182	1689	6	13	39	15900	22700
160	1232	1695	7	15	49	18900	26000

Overall, the steel features very high uniform elongation and extraordinary high performance measured by the product of tensile strength and total elongation. 27,000 MPa% are achieved.

#### 6.4.2. Quenching and Tempering

Additionally, state-of-the-art Quenching and Tempering, the standard heat treatment for low alloyed steel in the high strength level is demonstrated to compare the results. Austenitization is performed at 950 °C for 30 s, subsequent samples are quenched in water. Tempering is carried out in 100 K steps from 200 °C to 700 °C for 120 s. The graphs of the tensile tests are shown in figure 94.

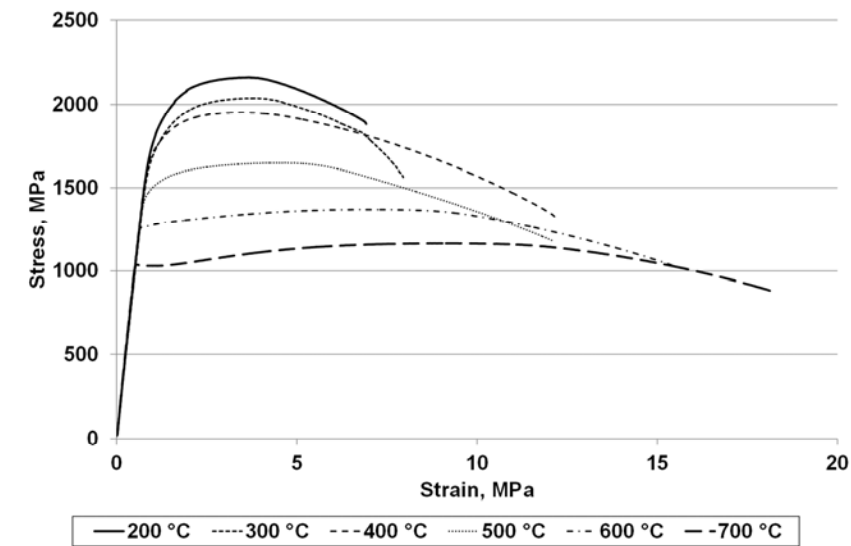


Figure 94: Tensile testing results of 42SiCrB steel after Quenching and Tempering heat treatment

The determined characteristic values according to international standard [ISO6892] are given in table 12.

Table 12: Tensile testing results of 42SiCrB steel after Quenching and Tempering heat treatment

T	R <sub>p0,2</sub>	R <sub>m</sub>	A <sub>g</sub>	A <sub>5</sub>	Z	R <sub>p0,2</sub> · A <sub>5</sub>	R <sub>m</sub> · A <sub>5</sub>
°C	MPa	MPa	%	%	%	MPa%	MPa%
200	1731	2352	3	5	8	7962	10821
300	1736	2038	3	13	54	22426	26329
400	1724	1952	3	13	54	21927	24824
500	1485	1650	4	13	50	19011	21116
600	1268	1371	6	17	48	20952	22653
700	1052	1178	7	19	51	19518	21867

The results of tensile testing after tempering at different temperatures are summed up in an annealing diagram, cf. figure 95. According to the findings of John Hollomon and Leonard Jaffe [Hollomon1945], the mechanical properties of low-alloyed steels obey linear dependence of tempering temperature, if the holding time remains constant. The expected linear behavior is represented by the dashed lines.

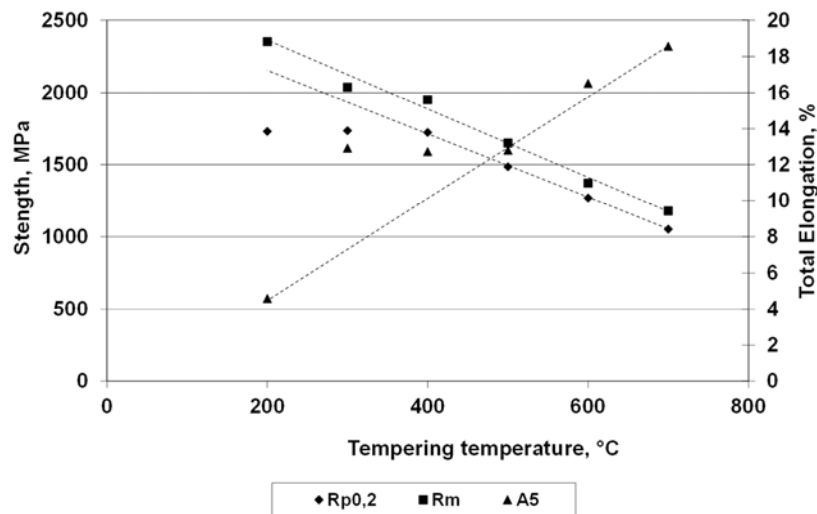


Figure 95: Annealing diagram of 42SiCrB steel, austenitization at 950 °C for 30 s and subsequent quenching in water. Dashed lines represent expected linear behavior according to Hollomon-Jaffe

## 6.5. Transmission Electron Microscopy

The microstructures obtained by Quenching and Partitioning are of recent interest, as they are important for the mechanical properties. Furthermore, the simulations dealing with necessary partitioning temperature and time also need sufficient information about the dimensions of interest. The non-deformed head part of the two-step Quenching and Partitioning tensile test sample of 160 °C partitioning temperature

is used as sample material. The two-step sample is characterized by a lath type martensite matrix mainly, as shown in figure 96.

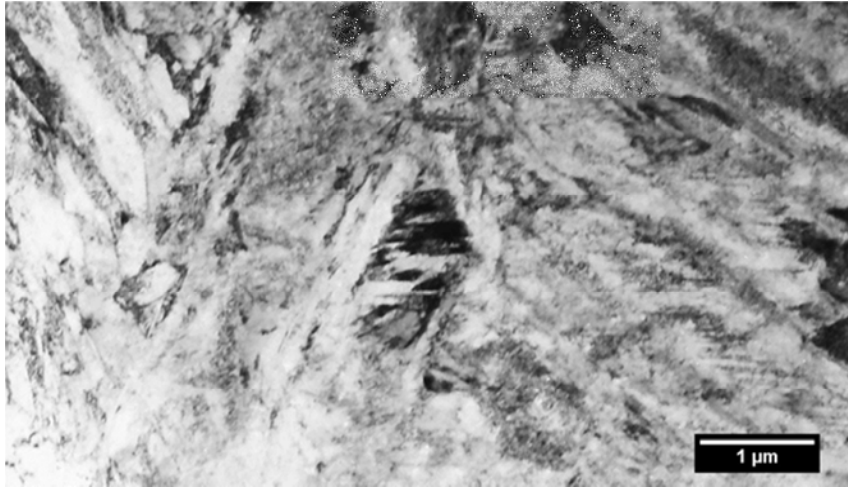


Figure 96: Bright field TEM image of  $42\text{SiCrB}$  steel after two-step Quenching and Partitioning heat treatment,  $160\text{ }^{\circ}\text{C}$  quenching and  $475\text{ }^{\circ}\text{C}$  partitioning temperature

As discussed in chapter 5.5, the expected size of retained austenite is in the range from nanometers to micrometers. This is the rationale for the use of low magnification in Transmission Electron Microscopy. Dark field Transmission Electron Microscopy combines information about shape and size with undisputable phase identification. Hence, the sample is investigated using dark field imaging on (200) diffraction spots of austenite, cf. figure 97. The corresponding TEM diffraction patterns and the corresponding indexation with JAVA Electron Microscopy Software (JEMS) are located in appendix F for better readability.

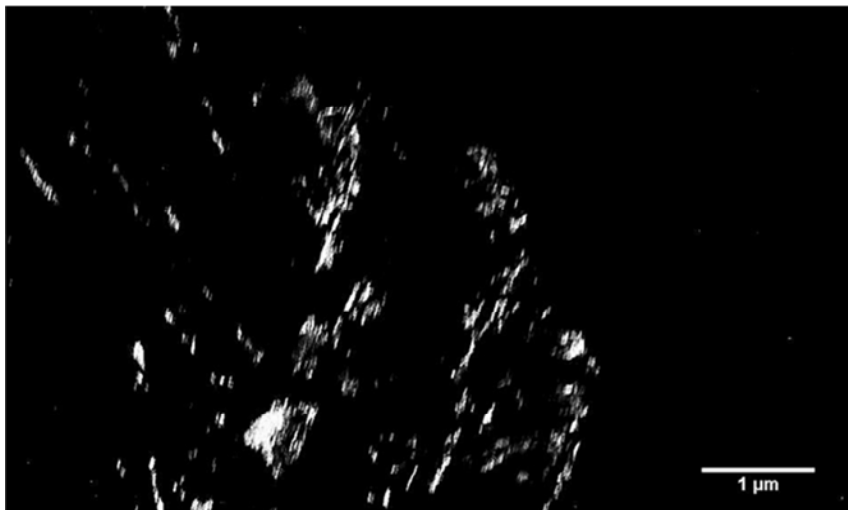


Figure 97: (200) austenite dark field TEM image of  $42\text{SiCrB}$  steel after two-step Quenching and Partitioning heat treatment with  $160\text{ }^{\circ}\text{C}$  quenching and  $475\text{ }^{\circ}\text{C}$  partitioning temperature

The dark field image shows residual austenite belonging to one prior austenite grain, as their crystallographic structure is clearly identical. Film type and isle type retained austenite are observed. The largest retained austenite area sizes at least  $0.5 \mu\text{m}$ , but nanometer sized areas are present as well. The retained austenite structures appear to be chopped.

## 6.6. X-Ray Diffraction

The samples taken from the threaded head of the tensile test samples, cf. chapter 6.4 are analyzed regarding their retained austenite volume fraction in comparison to the predictions of constrained carbon equilibrium model, respectively the shark fin-shaped dependence of retained austenite from quenching temperature.

The two-step Quenching and Partitioning samples are investigated using BRUKER AXS D8 ADVANCE X-ray diffractometer and copper anode. Two parts of the tensile test samples are investigated: the threaded part without plastic deformation and the strained gauge length. It is observable from the X-ray diffraction patterns, shown in figure 98, that the retained austenite stabilized by two-step Quenching and Partitioning transforms to martensite due to plastic deformation.

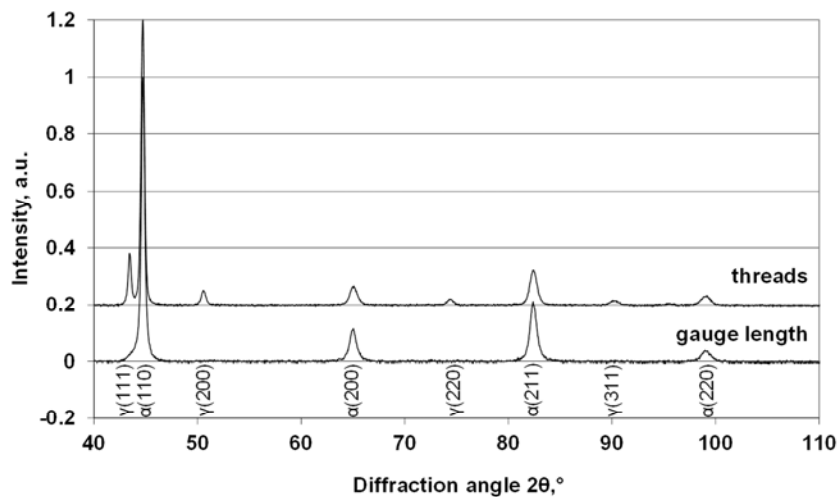


Figure 98: Normalized X-ray intensities vs. diffraction angle of tensile sample quenched to  $190 \text{ }^\circ\text{C}$  and partitioned at  $475 \text{ }^\circ\text{C}$

Figure 99 sums up the results of X-ray diffraction with the samples of different quenching temperatures. An approximately linear increasing trend is observed for the retained austenite volume fraction ranging from 0.18 at  $170 \text{ }^\circ\text{C}$  to 0.21 at  $210 \text{ }^\circ\text{C}$  in the thread part of the tensile samples; whereas in the gauge length actually no austenite is detectable by means of X-ray diffraction.

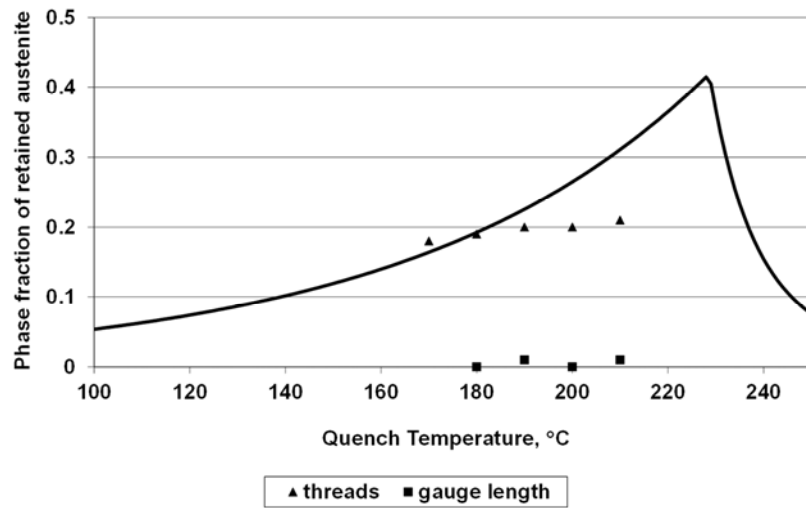


Figure 99: Retained austenite volume fraction vs. quenching temperature for  $42\text{SiCrB}$  steel tensile samples after two-step Quenching and Partitioning with subsequent partitioning at  $475\text{ }^\circ\text{C}$

## 7. Discussion

The validation of the manifold simulations around Quenching and Partitioning heat treatments are the focus of this chapter. Notably, carbon partitioning, cementite precipitation and bainite formation are discussed. Finally, consequences for the design of Quenching and Partitioning heat treatments are deduced from the experiments and the mechanical properties are reviewed as well.

### 7.1. Change in Length during Quenching and Partitioning

Before the dilatation in Quenching and Partitioning experiments is discussed the potentially contributing mechanisms are identified and the qualitative and quantitative contribution is calculated next. In general, the volume and length of a cube transforming from austenite to ferrite can be related to the lattice parameters if the total number of atoms is kept constant, see equation (43) taken from Manabu Takahashi and Harshad K. D. H. Bhadeshia [Takahashi1989]. The important factor of two represents the relation of the number of atoms per unit cell, respectively four iron atoms in face centered and two atoms in body centered cubic structure.

$$\frac{V_{\alpha}}{V_{\gamma}} = \frac{2a_{\alpha}^3}{a_{\gamma}^3} = \frac{(l_0 + \Delta l)^3}{l_0^3} \quad (43)$$

To calculate the change in length for a full phase transformation equation (43) is solved to the change in length (44).

$$\Delta l = \left( \sqrt[3]{2 \frac{a_{\alpha}}{a_{\gamma}}} - 1 \right) l_0 \quad (44)$$

Using ASTM E975 [ASTM-E975] lattice parameters for ferrite  $a_{\alpha}=0,28664$  nm, austenite  $a_{\gamma}=0,36$  nm and a sample length of  $l_0=10$  mm results in  $\Delta l = 32 \mu\text{m}$  for a full phase transformation at room temperature. In context to changes in length during the partitioning phase the value has to be multiplied by the austenite volume fraction. According to the CCE model the retained austenite volume fraction could reach up to 0.4, i.e. if all austenite decomposes to ferrite during partitioning the sample lengthening amounts about  $13 \mu\text{m}$ .

Following the principle of equation (43) with a change in the lattice parameter  $\Delta a$  and without a change in the cell structure, i.e. without the factor of two in this case, we can also determine the resulting change in length of a sample by using equation (45):

$$\frac{V_{\text{partitioned}}}{V_0} = \frac{(a_0 + \Delta a)^3}{a_0^3} = \frac{(l_0 + \Delta l)^3}{l_0^3} \quad (45)$$

Taking carbon partitioning and its effect on the lattice parameter into account by the definition of the linear relative carbon impact parameter  $k$ , cf. equation (46), the change in length due to carbon partitioning of a single-phase sample is described by equation (47).



$$k = \frac{\Delta a}{a_0 \cdot \Delta c_C} \quad (46)$$

$$\Delta l = \left( \frac{a_0 + \Delta a}{a_0} - 1 \right) \cdot l_0 = \frac{\Delta a}{a_0} \cdot l_0 = k \cdot \Delta c_C \cdot l_0 \quad (47)$$

If austenite carburization is considered, a change of 0.0017 nm in the austenite lattice parameter due to 1 wt.% carbon partitioning delivers the linear relative carbon impact parameter of austenite  $k_Y = 0.0047 \text{ wt.\%C}^{-1}$  for the usual austenite lattice parameter  $a_{Y0} = 0.36 \text{ nm}$ , cf. chapter 3.8.

If the same formula is used to calculate the expansion of martensite with carbon content as described by Kôtarô Honda and Zenji Nishiyama [Honda1932], respectively 0.12% or 0.00034 nm lattice expansion for change in carbon of  $\Delta c_C = 0.4 \text{ wt.\%}$  and  $a_{\alpha'0} = 0.286 \text{ nm}$  the linear relative carbon impact parameter for martensite is achieved to be  $k_{\alpha'} = 0.003 \text{ wt.\%C}^{-1}$ . As Kôtarô Honda and Zenji Nishiyama already mentioned in 1932, the martensite lattice parameter is linearly dependent on the carbon content up to 0.6 or 0.8 wt.% only. Hence, it is not recommended to use the linear relationship above; a constant should be used in this case.

The total change in the length of a dilatometer sample caused by carbon partitioning from martensite to austenite is obtained by superposition of both effects using the corresponding phase fractions:

$$\Delta l_{\text{total}} = k_Y \cdot (c_C^Y - c_C^{\text{alloy}}) \cdot l_0 \cdot V^Y - k_{\alpha'} \cdot c_C^{\text{alloy}} \cdot l_0 \cdot V^{\alpha'} \quad (48)$$

Furthermore, the austenite carbon concentration after full partitioning, cf. equation (2), has to be considered. After simplification the total change in length during carbon partitioning is described by equation (49).

$$\Delta l_{\text{total}} = (k_Y - k_{\alpha'}) \cdot c_C^{\text{alloy}} \cdot l_0 \cdot V^{\alpha'} \quad (49)$$

The change in length due to carbon partitioning from martensite into austenite is directly proportional to the martensite volume fraction and the nominal carbon content.

Using the information from the constrained carbon equilibrium model described in chapter 4.3.1 the lengthening can be determined at any quenching temperature. The results are shown in figure 100.

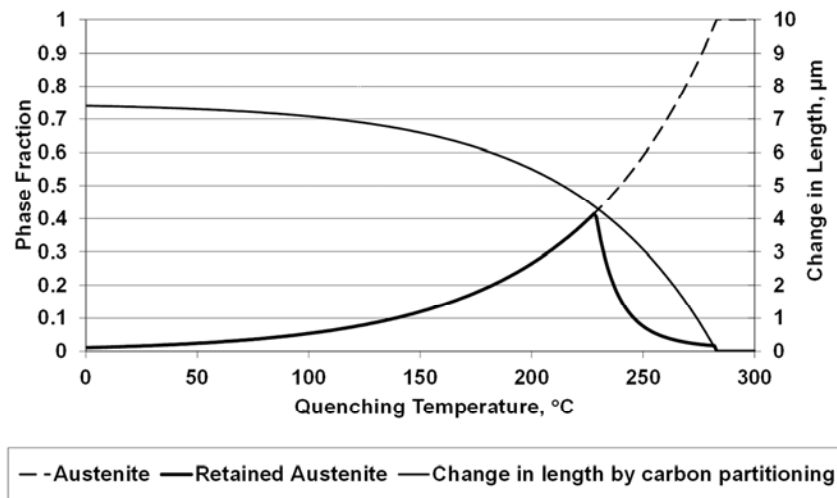


Figure 100: Change in length of a 10 mm dilatometer sample from  $42\text{SiCrB}$  steel due to full carbon partitioning according to the constrained carbon equilibrium model

According to the calculation  $42\text{SiCrB}$  steel samples can reach about  $7\ \mu\text{m}$  lengthening due to carbon partitioning in dilatometric experiments. With increasing quenching temperature, the increase in length is reduced and vanishes at martensite start temperature.

Further plausible mechanisms acting during partitioning and associated dilatometric response are already consolidated by Emmanuel De Moor et. al. [DeMoor2008a]. To obtain practical information about the order of magnitude of the mechanisms the list is extended in table 13. Furthermore experimental data is taken from Fe-1.18 wt.%C steel tempering experiments by Eric Mittemeijer and Ignacy Wierszyllowski [Mittemeijer1991] to rate the effects of carbide formation.

With regard to transition carbide formation the expansion suggested by Emmanuel De Moor et. al. [DeMoor2008a] is in conflict to the experimental results of Eric Mittemeijer and Ignacy Wierszyllowski [Mittemeijer1991]. As all carbide formations are connected with diminishing density it is often considered that the sample elongates. Furthermore, cementite formation is often associated with austenite decomposition, what causes additional errors. As cementite has the lowest density of the considered iron carbides it is used for the following calculation in an extreme case. According to the equilibrium Fe-C phase diagram, the maximum amount of cementite is 0.066 for 0.44 wt.% of carbon obtained by lever rule. Using the density of cementite  $\rho_0=7.69\ \text{gcm}^{-3}$  and the density of ferrite  $\rho_\alpha=7.87\ \text{gcm}^{-3}$  the resulting lengthening of the 10 mm sample is about  $5\ \mu\text{m}$ . If the carbon decrease in the martensite or austenite matrix is considered as well, according to the above made assumptions, it is noted that the sample has to shrink concurrently. Shrinkage is  $20\ \mu\text{m}$  for carbon depletion from austenite and  $13\ \mu\text{m}$  from martensite using equation (47). Considering the maximum volume fraction of retained austenite, i.e. 0.4, the maximum contraction of austenite has to be reduced to  $6\ \mu\text{m}$  in the austenite case. For cementite formation within the martensite  $8\ \mu\text{m}$  contraction remains.

Table 13: Possible mechanisms affecting the length of a 10 mm sample during partitioning of 42SiCrB steel

Mechanism	Direction	Change in length of 42SiCrB steel ( $l_0=10\text{mm}$ )
C partitioning from martensite to austenite	Expansion	0-7 $\mu\text{m}$
Austenite decomposition to martensite or ferrite $\gamma \rightarrow \alpha' / \alpha$	Expansion	0-13 $\mu\text{m}$
Carbide formation in austenite $\gamma \rightarrow \theta$	Contraction	0-6 $\mu\text{m}$
Carbide formation in martensite $\alpha' \rightarrow \varepsilon / \eta \rightarrow \theta$	Contraction	0-8 $\mu\text{m}$

Finally, it is concluded that it is not possible to distinguish between all mechanisms acting if only dilatometric data is available. Markedly if the sample length increases during partitioning, it is still questionable if carbon partitioning or phase transformation occurs. If very high lengthening occurs, more to the point above 7  $\mu\text{m}$ , phase transformation is present. If the sample is shrinking during the partitioning phase, carbide formation is very likely; nevertheless the exact type of carbide is ambiguous.

## 7.2. Carbon Partitioning

As it is present aim of this study to predict reasonable times for full carbon partitioning between martensite and austenite it is essential to measure the carbon partitioning to validate the performed simulations. Since the carbon diffusion takes place in atomistic scales, only indirect measurement is possible. In this case, the strong influence of the solute carbon on the austenite lattice parameter is used to track the diffusion. The qualitative influence is well known and even the quantitative effect is already given in literature, even though with some uncertainty.

Before making conclusions, the accuracy and precision of lattice parameter analysis with X-ray diffraction requires further analysis. Chiefly, because the experimental setup is definitely not optimized for lattice parameter analysis; i.e. using high diffraction angles and long exposure times. To achieve information about the accuracy, measured lattice parameters of austenite at 950 °C and ferrite lattice parameters at room temperature are determined from the in-situ experiments and compared to literature values, cf. table 14.

Table 14: Lattice parameters of austenite at 950 °C and ferrite at room temperature measured by in-situ X-ray diffraction compared to literature data \*[Sekiz005] \*\*[ASTM-E975]

Source	PETRA III	SEIFERT SUN	SEIFERT SUN	SEIFERT SUN	Expected Value	Maximum Deviation
Units	Nm	Nm	Nm	Nm	nm	Nm
$a_{(200)\gamma}$ 950 °C	0,3666	0,3663	0,3663	0,3662	0,3659*	0,0007
$a_{(200)\alpha}$ 25 °C	0,2864	0,2870	0,2872	0,2870	0,2866**	0,0006

The accuracy of the in-situ X-ray diffraction experiments is conservatively approximated to be  $\pm 0.001$  nm. The precision is approximated conservatively as well by use of the standard deviation of the temperature corrected ferrite lattice parameter, which is nearly constant. It is calculated to  $\pm 0.0002$  nm in maximum, i.e. the precision of the in-situ experiments is at least five times better than the accuracy. This factor implies that the accuracy of the carbon content is about  $\pm 0.6$  wt.% and the minimum detectable change of carbon in austenite amounts  $\pm 0.12$  wt.% only. Nevertheless, this is adequate to characterize carbon partitioning qualitatively.

Further discussion analyzes the influence of carbon partitioning and the counteracting mechanisms on the change in length during dilatometry, predicted by the calculations in chapter 7.1. For this reason, three sets of dilatometer and corresponding in-situ X-ray diffraction data are compared below.

First, the absorption of carbon from dissolving carbides during austenitization is observed by lengthening and increasing austenite carbon content, derived from the corresponding lattice parameter, in the dilatometric and the fast in-situ experiments. The relevant data from the austenitization of the PETRA III synchrotron experiment is presented in figure 101.

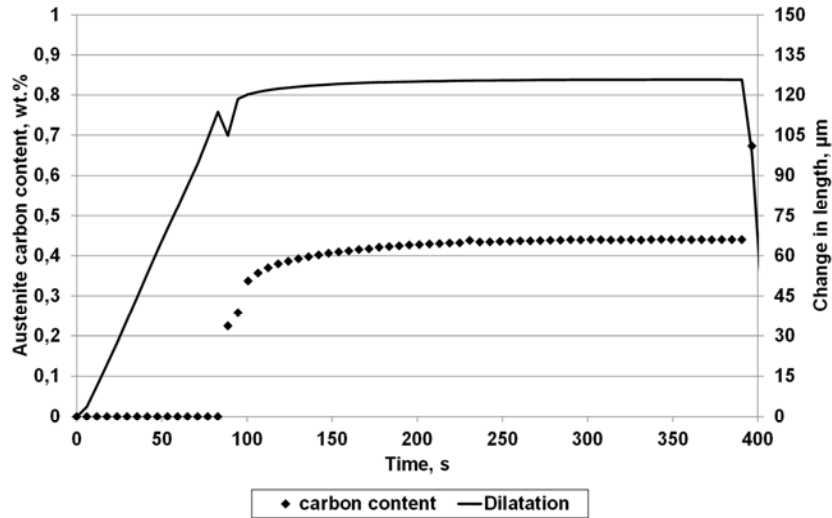


Figure 101: Comparison of the austenite carbon content, measured by X-ray diffraction, with the simultaneous change in length during austenitization of  $42\text{SiCrB}$  steel at  $950\text{ }^{\circ}\text{C}$

Dilatometry and X-ray diffraction consistently confirm that the ferrite to austenite phase transformation is already completed after 10 s. Subsequently, lengthening is observed as well as an increase of the austenite carbon content. It is remarkably that both curves run parallel to each other, indicating that the linear dependence of the lattice parameter on the austenite carbon content is measurable by dilatometry as well.

The carbon partitioning from martensite to austenite is analyzed next using the data from the two-step quenching and partitioning experiments. The linear relationship between the austenite carbon content and the lengthening can be also observed in figure 102.

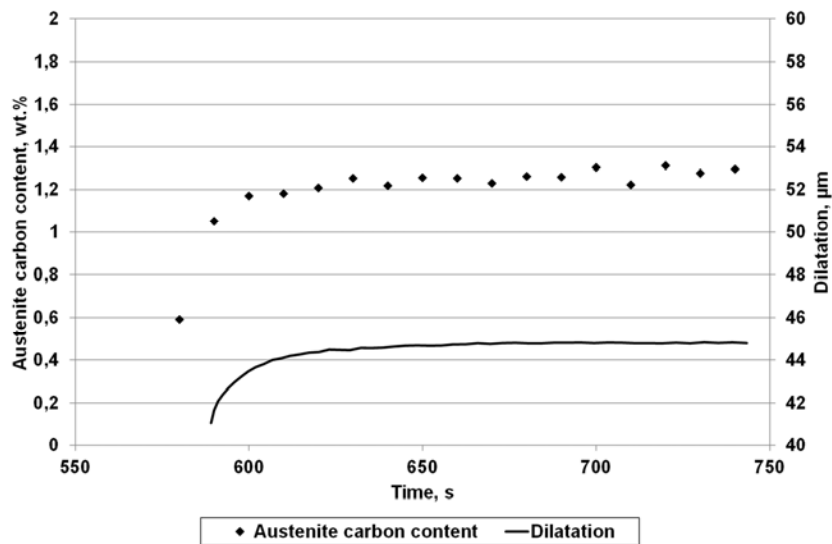


Figure 102: Dilatometry and austenite carbon content at  $400\text{ }^{\circ}\text{C}$  partitioning

At 400 °C partitioning, 4  $\mu\text{m}$  lengthening is observed after the partitioning temperature is reached. As 6  $\mu\text{m}$  are predicted by equation (49) the results are in good agreement. Even if 2  $\mu\text{m}$  are contributed by the 5 % of bainite measured by X-ray diffraction, cf. the results in chapter 6.3.2.

Unfortunately, no dilatometric data is available for partitioning at 475 °C, rather a qualitative comparison data is taken from the 500 °C two-step experiment. The curves are presented in figure 103. The linear dependence of the lengthening and the austenite carbon content are still present, but the curve looks significantly different. In the first seconds of the partitioning phase lengthening is observed, followed by ongoing shrinking over the time, while the austenite carbon content is increasing and decreasing simultaneously. In contrast to the experiment with partitioning at 400 °C cementite precipitation is present as well. It is remarkable that cementite formation occurs obviously from austenite, as at this temperature the carbon diffusion is significantly faster than the precipitation kinetics. This is furthermore important for the simulations of cementite precipitation in steel in general.

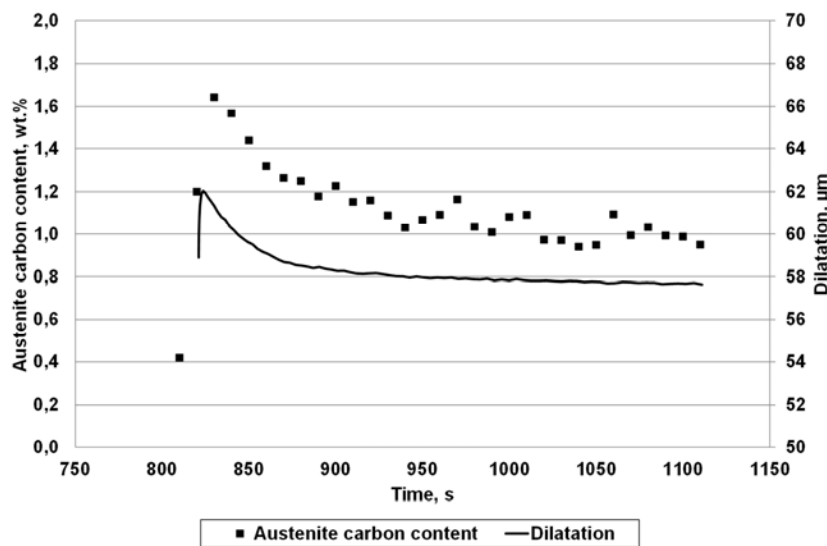


Figure 103: Dilatometry at 500 °C and X-ray austenite carbon content at 475 °C partitioning

The hypothesis that the carbon partitioning is measurable by dilatometry is new. Hence these results are compared with others next. Similar dilatometric measurements can be found in the work of Dorien De Knijf et al. The lengthening during partitioning is suggested to result from of “bainite, martensite to austenite interface migration or isothermal growth of martensite” [DeKnijf2012]. Partitioning itself is not discussed. Emmanuel De Moor et al. [DeMoor2008a] show similar results for the dilatometric response of two-step experiments with 0.24 wt.% C, 1.61 wt.% Mn, 1.45 wt.% Si, 0.30 wt.% Al steel as well, cf. Figure 68; Though he assumes “overall contraction of the sample during partitioning”, because of the martensite shrinking. However, the calculations in chapter 7.1 point obviously the other way.

Finally, backed up by the in-situ X-ray diffraction results, the lengthening of steel samples due to carbon partitioning is linearly dependent on the carbon content, as suggested in this thesis. Accordingly, the carbon partitioning from martensite to

austenite is measurable by means of dilatometry. Nevertheless, if the counteracting mechanism bainite formation is present as well it is difficult to distinguish between. Cementite formation from austenite is affecting the sample length as well, but in the opposite direction.

By this consideration, it is feasible to compare both experiments with the calculated times for carbon partitioning from chapter 5 with the experimental data. Due to the linear dependence, equivalent results are enforced for the partitioning time in both experiments: approximately 60 s. It is very important that this time is not for full partitioning, respectively the full balance of carbon within the austenite. It is the time for the transport from martensite to austenite only, since neither X-ray diffraction not dilatometry can measure local differences in the austenite carbon content. Only bulk information is accessible. In table 15 the necessary times for both situations: full carbon balance in austenite and escape of carbon from martensite are taken from chapter 5, more in detail from the analytic description of random walk and from the numerical simulations with mobile interface (DICTRA) and with stationary interface (MATCALC).

Table 15: Comparison of the predicted necessary carbon partitioning times and the experimental results

	Time for full carbon balance in austenite		Time for the escape of carbon from martensite	
	200 °C	400 °C	200 °C	400 °C
Random walk	> 10 <sup>6</sup> s	1,000 s	-	-
DICTRA prediction mobile interface	10,000 s	40 s	1,000 s	5 s
MATCALC prediction stationary interface	> 10 <sup>6</sup> s	1,000 s	10,000 s	100 s
Dilatometry and in-situ X-ray diffraction	-	-	>1,000 s	60 s

Demonstrated by the one-step in-situ experiment no significant carbon partitioning is observed at 200 °C within 1,000 s, rather the minimum detectable change of carbon in the austenite amounts 0.12 wt.%. Hence, the reduction of the second martensite start temperature by 100 °C, documented by the one-step experiments of chapter 6.2, can still be caused by carbon partitioning, as it is suggested from the simulations. A stabilization of austenite by 20 °C due to isothermal holding below martensite start temperature is already observed by E.R. Morgan and T. Ko in 1952 [Morgan1953], but carbon partitioning as reason for this unexpected behavior is not considered to be a

valid explanation, because the effect is observed at temperatures below 80 °C. Nevertheless, it is a strong indication that carbon partitioning as well as the additional austenite stabilizing effect are acting.

For quantitative comparison only two values for the time carbon needs to escape from martensite can be compared at 400 °C: 5 s obtained from numeric simulation with mobile spherical interface using DICTRA software and 100 s obtained from the planar MATCALC simulation using a stationary interface. As 60 s are confirmed experimentally, the stationary interface simulation is in suitable order of magnitude, while the mobile interface is 12 times too fast.

As both software packages use the same diffusion model with valid numeric algorithms and the same carbon mobilities, the cause must be found elsewhere. The mobile interface is excluded as well, as it increases the time for diffusion in martensite, because the interface movement lengthens the diffusion path. Further analysis of the used geometries explains the reason: Due to the constant austenite volume fractions and the same austenite size at the beginning of the simulations, the diffusion path for carbon in martensite is initially 4.725 times smaller in spherical geometry than in planar geometry. This result in a factor of 20 regarding the time, due to the root mean squared displacement of random walkers, cf. equation (33). This factor is reduced over time by the moving interface. The distances defined in the planar model are always larger.

Regarding the time for full partitioning, the simulations with moving interface reveal an additional disadvantage: The final austenite volume fraction is assumed to fulfil paraequilibrium conditions, cf. chapter 5.4. According to the final volume fractions of 0.2, actually obtained by two-step Quenching and Partitioning, this is undervalued and leads accordingly to very short partitioning times. For these reasons, the spherical geometry and mobile interfaces seem to be improper for the simulation of Quenching and Partitioning. Constrained carbon equilibrium conditions deliver more reasonable values in this case.

As the measured lattice parameters are average values of the involved sample volume, local changes, as expected by carbon partitioning, cannot be distinguished.

### 7.3. Counteracting Cementite Precipitation

During experiments at and above 400 °C cementite formation is observed consuming carbon from the austenite encouraging its decomposition. This is confirmed by the in-situ experiments with partitioning at 475 °C, as well for interrupted quenching to 170 °C as for full quenching to room temperature. The dilatometric observations of the tempering behavior of 42SiCrB steel, cf. chapter 6.2.3, support this hypothesis as well. As shrinking of dilatometer samples is related to cementite formation, begin and end of cementite formation can be determined from the two step experiments in figure 68 summed up in the following table.



Table 16: Times for begin and end of cementite precipitation derived from dilatometric two-step Quenching and Partitioning experiments.

	Begin of cementite precipitation	End of cementite precipitation
500 °C	6 s	450 s
450 °C	30 s	2100 s
400 °C	280 s	>10,000 s

The MATCALC simulation of chapter 5.3 does not predict any cementite precipitations from austenite in this temperature range, even for higher carbon contents. This leads to the assessment that the conditions for cementite precipitation after quenching are distinct from the used simulation parameters taken from Ernst Kozeschnik and Harry Bhadeshia for conventional TRIP assisted steel [Kozeschnik2008]. The driving force at 475 °C, cf. figure 104, for paraequilibrium cementite is negative, even for high carbon contents, while that for orthoequilibrium cementite formation is positive.

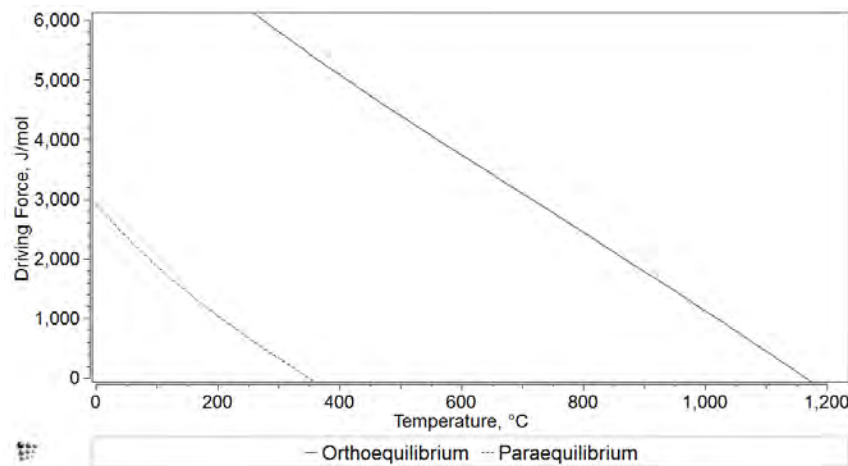


Figure 104: Driving force for cementite precipitation in carbon enriched retained austenite with 2 wt.% carbon

This ensures nucleation, but the growth is delayed by the limited diffusion of the substitutional alloying elements, although cementite formation occurs. This allows only one conclusion: the diffusion must be drastically enhanced. Review of the used parameters suggests that the estimated dislocation density of  $10^{12} \text{ m}^{-2}$  is unrealistic. Since the austenite is surrounded by the high strained martensitic matrix and is affected by its volume expansion and shear during the martensitic phase transformation the dislocation density must be located far away from equilibrium. The dislocation density of martensite is given in the range between  $10^{15} \text{ m}^{-2}$  and  $10^{16} \text{ m}^{-2}$ , but usually the dislocation density of the enclosed retained austenite is not mentioned explicitly. In the following it is assumed, that the dislocation densities of martensite and enclosed retained austenite are equal. The orthoequilibrium cementite precipitation simulation of chapter 5.3 is repeated using  $3 \cdot 10^{15} \text{ m}^{-2}$  as new estimate for the retained austenite dislocation density in the temperature range of interest. The

results are presented in figure 105 and compared to the experimental data obtained by dilatometry from table 16.

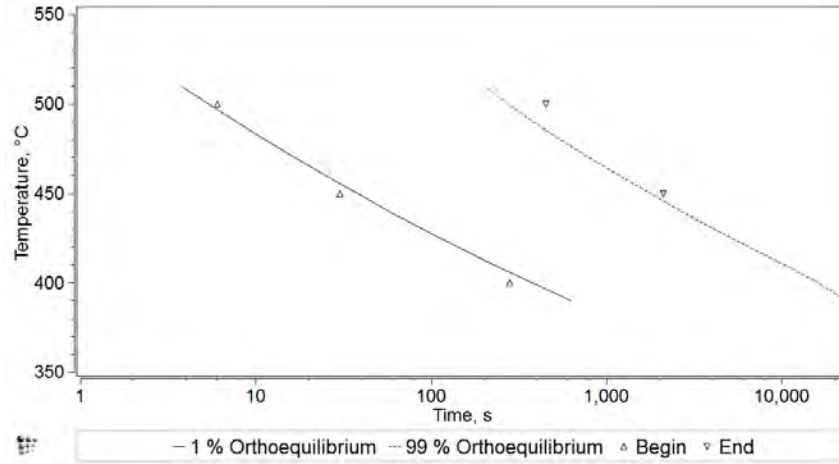


Figure 105: Orthoequilibrium cementite precipitation from carbon enriched retained austenite with high dislocation density compared to dilatometric experiments

The correlation between simulation and experimental data allows some conclusions regarding the design of Quenching and Partitioning heat treatments. In general, cementite precipitation from retained austenite is very likely due to its high carbon content caused by carbon partitioning and its high dislocation density caused by the prior martensitic phase transformation. From this it follows that the available time for partitioning is limited if cementite precipitation should be suppressed completely. Accordingly, the size of the retained austenite should be very small, what can be achieved by low quenching temperatures also reducing the amount of retained austenite in total. Alternatively, cementite precipitation can be disregarded, since the carbon content in the retained austenite is still elevated significantly as shown in the in-situ experiment at 475°C, even with cementite precipitation.

#### 7.4. Counteracting Bainite Formation

According to the empirical formula, given by equation (50), taken from Harry Bhadeshia and Sir Robert Honeycombe [Bhadeshia2006], the bainite start temperature for 42SiCrB steel is determined to be 550 °C, using the chemical composition from table 1.

$$B_S = 830 - 270c_C^{\text{alloy}} - 90c_{\text{Mn}}^{\text{alloy}} - 37c_{\text{Ni}}^{\text{alloy}} - 70c_{\text{Cr}}^{\text{alloy}} - 83c_{\text{Mo}}^{\text{alloy}} \quad (50)$$

Remembering the opposing effects of counteracting mechanisms from chapter 3.5, the bainite formation is taken into account by considering full carbon partitioning into the austenite as well. The bainite start temperature of carbon enriched retained austenite  $B_S^{\text{II}}$  after full partitioning is approximately described by:

$$B_S^{\text{II}} = 830 - 270c_C^{\text{Y}} - 90c_{\text{Mn}}^{\text{alloy}} - 37c_{\text{Ni}}^{\text{alloy}} - 70c_{\text{Cr}}^{\text{alloy}} - 83c_{\text{Mo}}^{\text{alloy}} \quad (51)$$

For the Quenching and Partitioning heat treatment, the recommended minimum partitioning temperature should be above the bainite start temperature of carbon enriched retained austenite  $B_s^{\text{II}}$  to prevent bainite formation, if full carbon partitioning is assumed. If the bainite formation occurs faster than the carbon enrichment, then bainite forms though. The dependence of the minimum partitioning temperature to avoid bainite formation on the quenching temperature and the corresponding retained austenite carbon content is given in figure 106 by combining equation (51) with the Constrained Carbon Equilibrium model, cf. chapter 4.3.1.

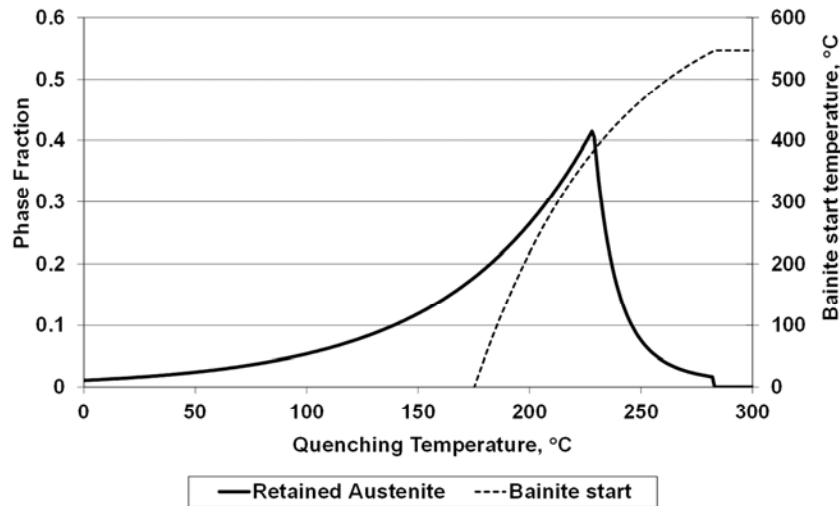


Figure 106: Calculated Bainite start temperature after full partitioning of carbon approximated by empirical models

An isothermal phase transformation is also observed counteracting during the Quenching and Partitioning heat treatments. The corresponding dilatometric results, shown in chapter 6.2, correlate with dilatometric experiments of Sung J. Kim et al. [Kim2008] using two 0.15 wt.% C steels with different Mn and Si additions and Stefan van Bohemen et al. [vanBohemen2008] using plain 0.66 wt.% carbon steel. I agree fully that bainite is the most reasonable explanation for the isothermal change in length. Their arguments, that bainite morphology is observed and that the phase transformation follows bainite kinetics are already strong, nevertheless a thought experiment is added here: If the isothermal TTT diagram, cf. figure 64, is considered and the athermal martensite formation is virtually suppressed, the C-shaped kinetics of bainite imply that its reaction is generally possible at lower temperatures as well. Adding increasing dislocation densities, as discussed above, the enhanced kinetics below the martensite start temperature, cf. figure 67, are reasonable as well. Though isothermal martensite cannot be explicitly excluded, since high local amounts of carbon give rise to the assumption that isothermal martensitic phase transformations are possible, cf. [Borgenstam1997]

The statement above, that too high quenching temperatures do not ensure sufficient bainite suppression is tested by the two-step experiments carried out on the dilatometer as well. Quenching to 170 °C is compared to quenching at 230 °C in figure 69 with subsequent partitioning at 400 °C. The experiment using a low quenching temperature only shows a small increase in length of 3  $\mu\text{m}$  caused by partitioning,

while the sample quenched to 230 °C lengthens 10 μm during partitioning, too excessive for carbon partitioning and therefore witnesses bainite phase transformation. Accordingly, it is possible to avoid bainite formation by lowering the bainite start temperature due to low quenching temperatures and intense carbon partitioning. Furthermore, the partitioning temperature has to be high enough; otherwise the retained austenite is decomposed by bainite faster than carbon partitioning can suppress its formation, as it is the case for one-step Quenching and Partitioning.

## 7.5. Mechanical Properties

Carbon partitioning from martensite to austenite has been previously observed during Quenching and Tempering. It is likely to form a martensitic TRIP assisted steel with low phase fraction of carbon enriched retained austenite by the usual hardening of 42SiCrB steel if the tempering, rather partitioning, is carried out at temperatures ensuring that excessive cementite precipitation does not occur. Since 42SiCrB steel has some amount of retained austenite after direct quenching to room temperature and there are only negligible changes in the austenite phase fraction during tempering up to 400 °C, it can be concluded that the microstructure consists of martensite and austenite only and is actually the desired microstructure of Quenching and Partitioning with very low amount of retained austenite. Hence, low tempered steels are in some way the ancestors of martensitic TRIP assisted steels. This has already been observed in the mechanical properties, as shown in the annealing diagram, see figure 95, by a significant drop in yield strength at 300 °C tempering, while the total elongation increases remarkably.

A two-step Quenching and Partitioning heat treatment produces significantly higher retained austenite volume fractions with remarkably different mechanical properties, which are discussed next. Therefore, the conventional stress-strain behavior of martensitic steel obtained by Quenching and Tempering is compared to the properties of the two-step Quenching and Partitioning tensile test after quenching to 190 °C in figure 107. To explain the differences and the similarities, two different annealing temperatures are selected: 700 °C with the same yield strength and 500 °C with the same tensile strength level.

At the same tensile strength level, respectively tempering at 500 °C, the yield strength is reduced by 400 MPa, since high phase fractions of relatively weak retained austenite are present. Due to the TRIP effect, confirmed by the X-ray diffraction measurements after tensile testing, cf. figure 98, high strain hardening is observed as the retained austenite transforms to martensite. Finally, the tensile strength reaches the same level of strength and the total elongation is 5 % higher. Compared to the sample annealed at 700 °C with similar yield strength, the tensile strength is increased by 500 MPa, while the total elongation stays constant at 15 %.

Martensitic TRIP assisted steels feature low yield strength, high tensile strength and high elongations at the same time, which is absolutely new for high strength low alloyed steels. Furthermore, the uniform elongation reaches significantly higher values compared to quenched and tempered steels.

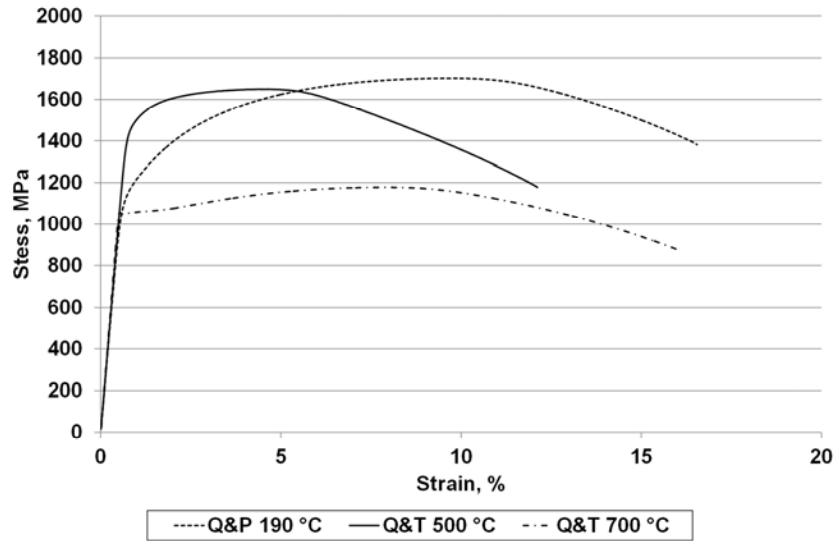


Figure 107: Comparison of stress strain curves from two-step Quenching and Partitioning and Quenching and Tempering with similar yield and tensile strength

Last of all, the mechanical properties of this study are compared to the results with full austenitization available in literature, already presented in chapter 3.7. Therefore, the new tensile test results are present in figure 108 as well. Weighted by the product of total elongation and tensile strength, the martensitic TRIP assisted steel obtained in this study outperforms all known values for this steel family in literature.

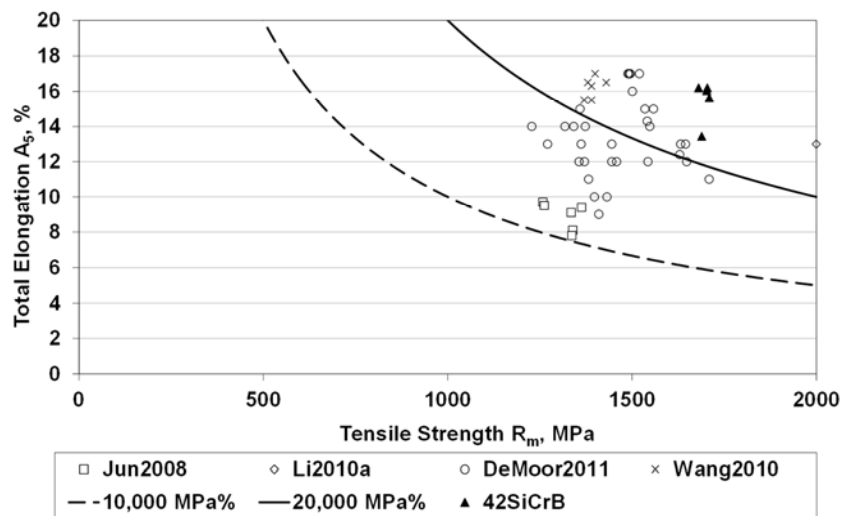


Figure 108: Comparison of total elongation vs. tensile strength of martensitic TRIP assisted steels made by Quenching and Partitioning after full austenitization [Jun2008] [Wang2010] [Li2010] [DeMoor2011]

Comparing the maximum retained austenite volume fractions with the performance, respectively the product of tensile strength and total elongation, cf. figure 109, it is obvious that the material in this study has a significantly higher retained austenite volume fraction. I am convinced that the outstanding properties of the 42SiCrB steel, processed by two-step Quenching and Partitioning, are caused by the high amount of retained austenite and the corresponding TRIP effect.

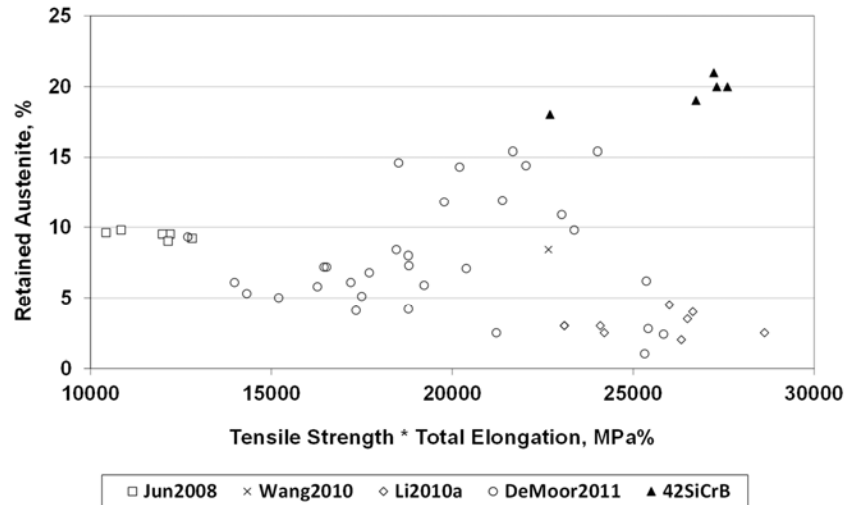


Figure 109: Influence of the retained austenite volume fraction on the product of tensile strength and total elongation for Quenching and Partitioning with full austenitization [Jun2008] [Wang2010] [Li2010] [DeMoor2011]

Although the results of Li et al. [Li2010] and a selection of Emmanuel De Moor's values [DeMoor2011] show that high amounts of retained austenite are not mandatory for high performance steels. With 5 % of retained austenite or less, the contribution of the TRIP effect is quite questionable. The steels developed in these studies conceal another mystery. I share the opinion of Harshad K. D. H. Bhadeshia [Bhadeshia2002] that multiphase steels can significantly gain in strength and elongation from their composite structures as well.

Nevertheless, the initial hypothesis of this study, that higher amounts of retained austenite have positive impact on the mechanical properties of martensitic TRIP assisted steels is confirmed.

## 8. Summary

$42\text{SiCrB}$  steel is characterized by the same counteracting mechanisms like the most low alloyed steels forming bainite, secondary martensite and or cementite when applied to Quenching and Partitioning heat treatments. However it is possible to prevent these if the following scientific findings of this study are considered:

Sufficient carbon partitioning can be guaranteed by analytical or numerical calculations of carbon diffusion, if the size of the retained austenite is known. The found dependence of the average retained austenite dimensions on the prior austenite grain size and the retained austenite volume fraction is of particular interest as both are significant for successful heat treatments.

Two heat treatment parameters are identified to influence the bainite formation: The quenching and the partitioning temperature. The first should be low enough, the second high enough to make bainite formation unlikely.

The maximum partitioning time and temperature are limited by cementite precipitation in austenite. MatCalc simulations are identified to be helpful preventing cementite precipitation by optimization of the chemistry or the partitioning heat treatment parameters.

Applying Quenching and Partitioning heat treatments to  $42\text{SiCrB}$  steel in compliance with these findings 20 % of retained austenite are stabilized in this study. This introduces significant TRIP effect to the martensitic matrix resulting in a new steel family with its own particularities: low yield strength and improved elongation at very high tensile strength levels. The product of tensile strength and total elongation of  $42\text{SiCrB}$  steel exceeds 27,000 MPa%, this is outstanding for low alloyed steel.

Finally this study is a recipe for successful Quenching & Partitioning.

Enjoy!

---

## 9. References

- [Ågren1986]: ÅGREN, J.: A revised expression for the diffusivity of carbon in binary Fe-C austenite. In: *Scripta Metallurgica* 20 (1986), no. 11, p. 1507-1510
- [Andersson2002]: ANDERSSON, J.-O.; HELANDER, T.; HÖGLUND, L.; SHI, P. and SUNDMAN, B.: THERMO-CALC and DICTRA, computational tools for materials science. In: *Calphad* 26 (2002), no. 2, p. 273-312
- [Andrews1965]: ANDREWS, K. W.: Empirical Formulae for the Calculation of some Transformation Temperatures. In: *JISI* 203 (1965), p. 721-727
- [ArcelorMittal2013]: ARCELORMITTAL: TRIP (Transformation Induced Plasticity) steels, Brochure, 2013
- [ASTM-E975]: ASTM INTERNATIONAL: X-Ray Determination of Retained Austenite in Steel with Near Random Crystallographic Orientation, Standard, E 975, 2003
- [Bagliani2013]: BAGLIANI, E. P.; SANTOFIMIA, M. J.; ZHAO, L.; SIETSMA, J. and ANELLI, E.: Microstructure, tensile and toughness properties after quenching and partitioning treatments of a medium-carbon steel. In: *Materials Science and Engineering: A* 559 (2013), p. 486-495
- [Bhadeshia1979]: BHADESHIA, H. K. D. H.: The Theory and Significance of Retained Austenite in Steels, PhD thesis, University of Cambridge, 1979
- [Bhadeshia1980]: BHADESHIA, H. K. D. H. AND EDMONDS, D. V.: The mechanism of bainite formation in steels. In: *Acta Metallurgica* 28 (1980), no. 9, p. 1265-1273
- [Bhadeshia2002]: BHADESHIA, H. K. D. H.: TRIP-Assisted Steels? In: *ISIJ International* 42 (2002), no. 9, p. 1059-1060
- [Bhadeshia2006]: BHADESHIA, H. K. D. H. AND HONEYCOMBE, R.: Steels - Microstructure and Properties, Oxford, *Butterworth-Heinemann*, 2006
- [Borgenstam1997]: BORGENTAM, A. & HILLERT, M.: Activation energy for isothermal martensite in ferrous alloys. *Acta Materialia* 45 (1997), p. 651-662
- [Bragg1915]: BRAGG, W. L. AND BRAGG, W. H.: x rays and crystal structure, London, *G. BELL AND SONS, LTD.*, 1915
- [Cerny2011]: ČERNÝ, I.; MIKULOVÁ, D.; SÍS, J.; MAŠEK, B.; JIRKOVÁ, H. and MALINA, J.: Fatigue properties of a low alloy 42SiCr steel heat treated by quenching and partitioning process. In: *Procedia Engineering*, 2011, p. 3310-3315
- [Chantler1995]: CHANTLER, C. T.: Theoretical Form Factor, Attenuation and Scattering Tabulation for  $Z=1-92$  from  $E=1-10$  eV to  $E=0.4-1.0$  MeV. In: *Journal of Physical and Chemical Reference Data* 24 (1995), no. 1, p. 71-643



- [Chantler2005]: CHANTLER, C.; OLSEN, K.; DRAGOSET, R.; CHANG, J.; KISHORE, A.; KOTOCHIGOVA, S. and ZUCKER, D. S.: X-Ray Form Factor, Attenuation and Scattering Tables (version 2.1), National Institute of Standards and Technology, Gaithersburg, MD, online, <http://physics.nist.gov/ffast>, 2005
- [Clarke2008]: CLARKE, A. J.; SPEER, J. G.; MILLER, M. K.; HACKENBERG, R. E.; EDMONDS, D. V.; MATLOCK, D. K.; RIZZO, F. C.; CLARKE, K. D. and MOOR, E. D.: Carbon partitioning to austenite from martensite or bainite during the quench and partition (Q&P) process: A critical assessment. In: *Acta Materialia* 56 (2008), no. 1, p. 16-22
- [Clarke2009]: CLARKE, A. J.; SPEER, J. G.; MATLOCK, D. K.; RIZZO, F. C.; EDMONDS, D. V. and SANTOFIMIA, M. J.: Influence of carbon partitioning kinetics on final austenite fraction during quenching and partitioning. In: *Scripta Materialia* 61 (2009), no. 2, p. 149-152
- [Crank1979]: CRANK, J.: The Mathematics of Diffusion, *Clarendon Press.*, 1979
- [DeKnijf2012]: DE KNIJF, D.; PETROV, R.; FOJER, C. and KESTENS, L. A. I.: Optimization and characterization of a quenching and partitioning heat treatment on a low carbon steel. In: *Materials Science and Technology Conference and Exhibition MS&T*, 2012, p. 1077-1085
- [DeMeyer2002]: DE MEYER, M.; MAHIEU, J. and DE COOMAN, B. C.: Empirical Microstructure Prediction Method for Combined Intercritical Annealing and Bainite Transformation of TRIP Steel. In: *Material Science and Technology* 18 (2002), p. 1121-1132
- [DeMoor2008]: DE MOOR, E.; LACROIX, S.; CLARKE, A. J.; PENNING, J. and SPEER, J. G.: Effect of Retained Austenite Stabilized via Quench and Partitioning on the Strain Hardening of Martensitic Steels. In: *Metallurgical and Materials Transactions A* 39 (2008), p. 2586-2595
- [DeMoor2008a]: DE MOOR, E.; PENNING, J.; FÖJER, C.; CLARKE, A. J. and SPEER, J. G.: Alloy Design for Enhanced Austenite Stabilization via Quenching and Partitioning. In: *International Conference on New Developments in Advanced High-Strength Sheet Steels proceedings*, 2008, p. 199-207
- [DeMoor2011]: DE MOOR, E.; SPEER, J. G.; EDMONDS, D. K.; J.-H., K. and LEE, S.-B.: Effect of Carbon and Manganese on the Quenching and Partitioning Response of CMnSi Steels. In: *ISIJ International* 1 (2011), no. 51, p. 137-144
- [Debye1916]: DEBYE, P. and SCHERRER, P.: Interferenzen an regellos orientierten Teilchen im Röntgenlicht. I. In: *Nachrichten von der Gesellschaft der Wissenschaften zu Göttingen, Mathematisch-Physikalische Klasse* 46 (1916), p. 1-15

- [Dijk2005]: VAN DIJK, N. H.; BUTT, A. M.; ZHAO, L.; SIETSMA, J.; OFFERMAN, S. E.; WRIGHT, J. P. and VAN DER ZWAAG, S.: Thermal stability of retained austenite in TRIP steels studied by synchrotron X-ray diffraction during cooling. In: *Acta Materialia* 53 (2005), no. 20, p. 5439-5447
- [Dmitrieva2011]: DMITRIEVA, O.; PONGE, D.; INDEN, G.; MILLÁN, J.; CHOI, P.; SIETSMA, J. and RAABE, D.: Chemical gradients across phase boundaries between martensite and austenite in steel studied by atom probe tomography and simulation. In: *Acta Materialia* 59 (2011), no. 1, p. 364-374
- [Downs2003]: DOWNS, R. T. and HALL-WALLACE, M.: The American Mineralogist Crystal Structure Database. In: *American Mineralogist* 88 (2003), p. 247-250
- [Edmonds2006]: EDMONDS, D. V.; HE, K.; RIZZO, F. C.; COOMAN, B. C. D.; MATLOCK, D. K. and SPEER, J. G.: Quenching and partitioning martensite–A novel steel heat treatment. In: *Materials Science and Engineering: A* 438-440 (2006), S. 25-34
- [Edmonds2006a]: EDMONDS, D. V.; HE, K.; RIZZO, F. C.; CLARKE, A.; MATLOCK, D. K. and SPEER, J. G.: Microstructural Features of a New Martensitic Steel Heat Treatment: Quenching and Partitioning. In: *Materials Science Forum* 539-543, 2006, p. 4819-4825
- [Einstein1905]: EINSTEIN, A.: Über die von der molekularkinetischen Theorie der Wärme geforderte Bewegung von in ruhenden Flüssigkeiten suspendierten Teilchen. In: *Annalen der Physik* 17 (1905), p. 549-560
- [Epp2012]: EPP, J.; HIRSCH, T. and CURFS, C.: In situ X-ray diffraction analysis of carbon partitioning during quenching of low carbon steel. In: *Metallurgical and Materials Transactions A: Physical Metallurgy and Materials Science* 43 (2012), no. 7, p. 2210-2217
- [Fick1855]: FICK, A.: Über Diffusion. In: *Annalen der Physik* 170 (1855), p. 59-86
- [Futch2012]: FUTCH, D. B.; THOMAS, G. A.; SPEER, J. G. and FINDLEY, K. O.: Thermomechanical simulation of hot rolled Q&P sheet steels. In: *Iron and Steel Technology* 9 (2012), no. 12, p. 101-106
- [Gao2013]: GAO, G.; ZHANG, H.; TAN, Z.; LIU, W. and BAI, B.: A carbide-free bainite/martensite/austenite triplex steel with enhanced mechanical properties treated by a novel quenching-partitioning-tempering process. In: *Materials Science and Engineering A* 559 (2013), p. 165-169
- [Gegner2006]: GEGNER, J.: Komplexe Diffusionsprozesse in Metallen, *expert Verlag*, 2006

- [Gerdemann2004]: GERDEMANN, F.: Microstructure/property correlations in steels heat-treated by the quenching and partitioning process, Diploma thesis, RWTH Aachen and ASPPRC Colorado School of Mines, 2004
- [Gupta1994]: GUPTA, C. K. and SURI, A. K.: Extractive metallurgy of niobium, *CRC Press, Inc.*, 1994
- [Hammersley1989]: HAMMERSLEY, A. P. and RIEKEL, C.: MFIT: Multiple Spectra Fitting Program. In: *Synchrotron Radiation News* 2 (1989), p. 24-26
- [Hammersley1997]: HAMMERSLEY, A. P.: FIT2D: An Introduction and Overview, ESRF Internal Report, 1997
- [Hatcher2012]: HATCHER, N.; MADSEN, G. K. H. and DRAUTZ, R.: DFT-based tight-binding modeling of iron-carbon. In: *Physical Review B - Condensed Matter and Materials Physics* 86 (2012), no. 155115, p. 1-12
- [He2003]: HE, B. B.: Introduction to two-dimensional X-ray diffraction. In: *Powder Diffraction* 18 (2003), no. 2, p. 71-85
- [He2009]: HE, B. B.: Two-Dimensional X-Ray Diffraction, *John Wiley and Sons, Inc., Hoboken, New Jersey*, 2009
- [Hillert2004]: HILLERT, M. and ÅGREN, J.: On the definitions of paraequilibrium and orthoequilibrium. In: *Scripta Materialia* 50 (2004), no. 5, p. 697-699
- [Hollomon1945]: HOLLOMON, J. H. and JAFFE, L. D.: Time-temperature Relations in Tempering Steel. In: *Transactions of the American Institute of Mining and Metallurgical Engineers* 162 (1945), p. 222-249
- [Honda1932]: HONDA, K. and NISHIYAMA, Z.: On the Nature of the Tetragonal and Cubic Martensites. In: *The Science Reports of the Tôhoku Imperial University*, 1932, p. 299-331
- [Houdremont1956]: HOUDREMONT, E.: Handbuch der Sonderstahlkunde, *Springer-Verlag OHG, Berlin*, 1956
- [Hougardy1984]: HOUGARDY, H. P.: Darstellung der Umwandlungen für technische Anwendungen und Möglichkeiten ihrer Beeinflussung. In: *Werkstoffkunde Stahl Band 1: Grundlagen*, *Springer-Verlag Berlin/Heidelberg und Verlag Stahleisen m.b.H., Düsseldorf*, 1984
- [Hougardy1990]: HOUGARDY, H. P.: Umwandlung und Gefüge unlegierter Stähle: *Stahl Eisen Verlag*, 1990
- [Hsu2007]: HSU, T. Y. and XU, Z.: Design of structure, composition and heat treatment process for high strength steel. In: *PRICM 6: Sixth Pacific Rim International Conference on Advanced Materials and Processing (Materials Science Forum)*, *Trans Tech Publications Ltd.*, 2007, p. 2283-2286

- [Hsu2013]: HSU, T. Y.; JIN, X. J. and RONG, Y. H.: Strengthening and toughening mechanisms of quenching-partitioning-tempering (Q-P-T) steels. In: *Journal of Alloys and Compounds* 577 (2013), no. 1, p. 568-571
- [Hultgren1947]: HULTGREN, A.: Isothermal transformation of austenite. In: *ASM Transactions* 39 (1947), p. 915-1005
- [ISO2566]: INTERNATIONAL ORGANIZATION FOR STANDARDIZATION: ISO 2566 Umrechnung von Bruchdehnungswerten Teil 1: Unlegierte und niedrig legierte Stähle, Beuth Verlag GmbH, 1999
- [ISO6507]: INTERNATIONAL ORGANIZATION FOR STANDARDIZATION: ISO 6507 Metallische Werkstoffe - Härteprüfung nach Vickers - Teil 1: Prüfverfahren, Beuth Verlag GmbH, 2006
- [ISO6892]: INTERNATIONAL ORGANIZATION FOR STANDARDIZATION: ISO 6892 Metallic materials - Tensile testing - Part 1: Method of test at room temperature, Beuth Verlag GmbH, 2009
- [ISO10275]: INTERNATIONAL ORGANIZATION FOR STANDARDIZATION: ISO 10275 Metallic materials - Sheet and strip - Determination of tensile strain hardening exponent, Beuth Verlag GmbH, 2007
- [IUCr1968]: INTERNATIONAL UNION OF CRYSTALLOGRAPHY: International tables for X-ray crystallography; Vol. 3; Physical and chemical tables, 1968
- [Jang2013]: JANG, J. H.; BHADSHIA, H. K. D. H. and SUH, D.-W.: Solubility of carbon in tetragonal ferrite in equilibrium with austenite. In: *Scripta Materialia* 68 (2013), p. 195-198
- [Joensson1994]: JÖNSSON, B.: Ferromagnetic ordering and diffusion of Carbon and Nitrogen in bcc Cr-Fe-Ni. In: *Zeitschrift fuer Metallkunde* 85 (1994), p. 498-501
- [Jun2008]: JUN, H. J. and FONSTEIN, N.: Microstructure and Tensile Properties of TRIP-aided Cr Sheet Steels: TRIP Dual and Q&P. In: *International Conference on New Developments in Advanced High-Strength Sheet Steels proceedings*, 2008, p. 155-168
- [Kemmer1985]: Kemmer, J.: Positionempfindliche Silicium-Kernstrahlungsdetektoren. In: *Physikalische Blätter* 41 (1985), no. 5, p. 117-122
- [Kim2008]: KIM, S. J.; SPEER, J.; KIM, H. S. and DE COOMAN, B. C.: Kinetics of Phase Transformations during Q&P Processing. In: *International Conference on New Developments in Advanced High-Strength Sheet Steels proceedings*, 2008, p. 179-189
- [Kim2009]: KIM, D. H.; SPEER, J. G.; KIM, H. S. and DE COOMAN, B. C.: Observation of an isothermal transformation during quenching and partitioning processing. In: *Metallurgical and Materials Transactions A: Physical Metallurgy and Materials Science* 40 (2009), no. 9, p. 2048-2060

- [Kitahara2006]: KITAHARA, H.; UEJI, R.; TSUJI, N. and MINAMINO, Y.: Crystallographic features of lath martensite in low-carbon steel. In: *Acta Materialia* 54 (2006), no. 5, p. 1279-1288
- [Koistinen1959]: KOISTINEN, D. P. and MARBURGER, R. E.: A general equation prescribing the extent of the austenite-martensite transformation in pure iron-carbon alloys and plain carbon steels. In: *Acta Metallurgica* 7 (1959), no. 1, p. 59-60
- [Koseki2011]: KOSEKI, T. and BHADSHIA, H.: Martensitic Transformation, Tokyo University, 2011
- [Kozeschnik2008]: KOZESCHNIK, E. and BHADSHIA, H. K. D. H.: Influence of silicon on cementite precipitation in steels. In: *Materials Science and Technology* 24 (2008), p. 343-347
- [Kozeschnik2012]: KOZESCHNIK, E.; JANSSENS, K. and BATAILLE, C.: Modeling Solid-State Precipitation, *Momentum Press*, 2012
- [Kozeschnik2004]: KOZESCHNIK, E.; SVOBODA, J.; FRATZL, P. and FISCHER, F. D.: Modelling of kinetics in multi-component multi-phase systems with spherical precipitates: II: Numerical solution and application. In: *Materials Science and Engineering: A* 385 (2004), no. 1, S. 157-165
- [Kraus2000]: KRAUS, W. and NOLZE, G.: PowderCell 2.3, Federal Institute for Materials Research and Testing, Berlin, 2000
- [Kraus1996]: KRAUS, W. and NOLZE, G.: POWDER CELL - a program for the representation and manipulation of crystal structures and calculation of the resulting X-ray powder patterns. In: *Journal of Applied Crystallography* 29 (1996), p. 301-303
- [Krauss1990]: KRAUSS, G.: Steels: Heat Treatment and Processing Principles, *ASM International*, 1990
- [Li2010]: LI, H. Y.; LU, X. W.; LI, W. J. and JIN, X. J.: Microstructure and Mechanical Properties of an Ultrahigh-Strength 40SiMnNiCr Steel during the One-Step Quenching and Partitioning Process. In: *Metallurgical and Materials Transactions A* 41 (2010), p. 1284-1300
- [Liu2011a]: LIU, H.; JIN, X.; DONG, H. and SHI, J.: Martensitic microstructural transformations from the hot stamping, quenching and partitioning process. In: *Materials Characterization* 62 (2011), no. 2, p. 223-227
- [Liu2011]: LIU, H.; LU, X.; JIN, X.; DONG, H. and SHI, J.: Enhanced mechanical properties of a hot stamped advanced high-strength steel treated by quenching and partitioning process. In: *Scripta Materialia* 64 (2011), no. 8, p. 749-752
- [Lyakishev1984]: LYAKISHEV, N. P.; TULIN, N. A. and PLINER, Y. L.: Niobium in steels and alloys: metallurgical aspects of niobium from mineral deposits to alloy production and applications: *Companhia Brasileira de Metalurgica e Mineração - CBMM*, 1984

- [Matlock2003]: MATLOCK, D. K.; BRÄUTIGAM, V. E. and SPEER, J. G.: Application of the Quenching and Partitioning (Q&P) Process to a Medium-Carbon, High-Si Microalloyed Bar Steel. In: *Materials Science Forum* 426-432, *Trans Tech Publications Ltd.*, 2003, p. 1089-1094
- [Matsumura1987]: MATSUMURA, O.; SAKUMA, Y. and TAKECHI, H.: Trip and its kinetic aspects in austempered 0.4C-1.5Si-0.8Mn steel. In: *Scripta Metallurgica* 21 (1987), no. 10, p. 1301-1306
- [McCaffrey2005]: MCCAFFREY, J.: Easy Guide to Calibrating TEM's and STEM's, Norrox Scientific Ltd. Ottawa, Canada, online, 2005
- [Mittemeijer1992]: MITTEMEIJER, E. J.: Analysis of the kinetics of phase transformations. In: *Journal of Materials Science* 27 (1992), no. 15, p. 3977-3987
- [Mittemeijer1991]: MITTEMEIJER, E. J. and WIERSZYLLOWSKI, I. A.: Isothermal and nonisothermal kinetics of tempering iron-carbon and iron-nitrogen martensites and austenites. In: *Materials Research and Advanced Techniques* 82 (1991), no. 6, p. 419-429
- [Mola2013]: MOLA, J. and DE COOMAN, B. C.: Quenching and partitioning (Q&P) processing of martensitic stainless steels. In: *Metallurgical and Materials Transactions A: Physical Metallurgy and Materials Science* 44 (2013), no. 2, p. 946-967
- [Momma2011]: MOMMA, K. and IZUMI, F.: VESTA 3 for three-dimensional visualization of crystal, volumetric and morphology data. In: *J. Appl. Crystallogr* 44 (2011), p. 1272-1276
- [Morgan1953]: MORGAN, E. R. and KO, T.: Thermal stabilization of austenite in iron-carbon-nickel alloys. In: *Acta Metallurgica* 1 (1953), no. 1, p. 36-48
- [Nayak2008]: NAYAK, S. S.; ANUMOLU, R.; MISRA, R. D. K.; KIM, K. H. and LEE, D. L.: Microstructure-hardness relationship in quenched and partitioned medium-carbon and high-carbon steels containing silicon. In: *Materials Science and Engineering: A* 498 (2008), p. 442-456
- [Nishiyama1978]: NISHIYAMA, Z.: Martensitic Transformation, *Academic Press*, 1978
- [Oka1988]: OKA, M. & OKAMOTO, H.: Swing back in kinetics near Ms in hypereutectoid steels. In *Metallurgical Transactions A* 19 (1988), p. 447-452
- [Oliver1928]: OLIVER, D. A.: Proposed new criteria of ductility from a new law connecting the percentage elongation with size of test-piece. In: *Proceedings of the Institution of Mechanical Engineers* 115, 1928, p. 827-864
- [Onink1993]: ONINK, M.; BRAKMAN, C. M.; TICHELAAAR, F. D.; MITTEMEIJER, E. J.; VAN DER ZWAAG, S.; ROOT, J. H. and KONYER, N. B.: The lattice parameters of austenite and ferrite in FeC alloys as functions of carbon concentration and temperature. In: *Scripta Metallurgica et Materiala* 29 (1993), no. 8, p. 1011-1016

- [Pickardt2003]: PICKARDT, T.: Hochtemperatur-Mößbauerspektroskopie am metallischen Eisen und einer Eisen-Molybdän-Legierung bis 1500°C, PhD thesis, Universität Hamburg Fachbereich Chemie, 2003
- [Roth2009]: ROTH, I.; KRUPP, U.; CHRIST, H. J.; KÜBBELER, M. and FRITZEN, C.-P.: Deformation induced martensite formation in metastable austenitic steel during in situ fatigue loading in a scanning electron microscope. In: *ESOMAT proceedings*, 2009, no. 06030, p. 1-5
- [Santofimia2008]: SANTOFIMIA, M. J.; ZHAO, L. and SIETSMA, J.: Model for the interaction between interface migration and carbon diffusion during annealing of martensite-austenite microstructures in steels. In: *Scripta Materialia* 59 (2008), no. 2, p. 159-162
- [Santofimia2008a]: SANTOFIMIA, M. J.; ZHAO, L.; PETROV, R. and SIETSMA, J.: Characterization of the microstructure obtained by the quenching and partitioning process in a low-carbon steel. In: *Materials Characterization* 59 (2008), no. 12, p. 1758-1764
- [Santofimia2008b]: SANTOFIMIA, M. J.; TAKAHAMA, Y.; ZHAO, L. and SIETSMA, J.: Analysis of the Quenching and Partitioning (Q&P) Process with partial Austenitisation in a low-carbon steel by phase field modelling. In: *New Developments on Metallurgy and Applications of High Strength Steels, Buenos Aires*, 2008, p. 777-787
- [Santofimia2009]: SANTOFIMIA, M. J.; SPEER, J. G.; CLARKE, A. J.; ZHAO, L. and SIETSMA, J.: Influence of interface mobility on the evolution of austenite-martensite grain assemblies during annealing. In: *Acta Materialia* 57 (2009), no. 15, p. 4548-4557
- [Saunders1998]: SAUNDERS, N. and MIODOWNIK, A. P.: CALPHAD (Calculation of Phase Diagrams): A Comprehensive Guide, *Elsevier Science*, 1998
- [Sauveur1924]: SAUVEUR, A.: What is Steel? - Another Answer. In: *The Iron Age* 113 (1924), p. 581-583
- [Schell2014]: SCHELL, N.; KING, A.; BECKMANN, F.; FISCHER, T.; MÜLLER, M. and SCHREYER, A.: The high energy materials science beamline (HEMS) at PETRA III. In: *Materials Science Forum* 772, 2014, p. 57-61
- [Seki2005]: SEKI, I. and NAGATA, K.: Lattice Constant of Iron and Austenite Including Its Supersaturation Phase of Carbon. In: *ISIJ International* 45 (2005), no. 12, p. 1789-1794
- [Shutts2006]: SHUTTS, A. J.; SPEER, J. G.; MATLOCK, D. K.; EDMONDS, D.; RIZZO, F. and DAMM, E.: Q&P Processing of High Carbon Bar Steel. In: *New Developments in Long and Forged Products Proceedings*, 2006, p. 191-202
- [Smoluchowski1906]: VON SMOLUCHOWSKI, M.: Zur Kinetischen Theorie der Brown'schen Molekularbewegung und der Suspensionen. In: *Annalen der Physik* 21 (1906), p. 756-780

- [Speer2003]: SPEER, J.; MATLOCK, D. K.; COOMAN, B. D. and SCHROTH, J.: Carbon partitioning into austenite after martensite transformation. In: *Acta Materialia* 51 (2003), no. 9, p. 2611-2622
- [Speer2003a]: SPEER, J.; STREICHER, A.; MATLOCK, D.; RIZZO, F. and KRAUSS, G.: Quenching and partitioning: a fundamentally new process to create high strength TRIP sheet microstructures. In: DAMM, E. B. and MERWIN, M.: *Austenite Formation and Decomposition*, 2003, p. 505-522
- [Speer2004]: SPEER, J. G.; EDMONDS, D. V.; RIZZO, F. C. and MATLOCK, D. K.: Partitioning of carbon from supersaturated plates of ferrite, with application to steel processing and fundamentals of the bainite transformation. In: *Current Opinion in Solid State and Materials Science* 8 (2004), no. 3-4, p. 219-237
- [Speer2011]: SPEER, J.; DE MOOR, E.; FINDLEY, K.; MATLOCK, D.; DE COOMAN, B. and EDMONDS, D.: Analysis of microstructure evolution in quenching and partitioning automotive sheet steel. In: *Metallurgical and Materials Transactions A: Physical Metallurgy and Materials Science* 42 (2011), no. 12, p. 3591-3601
- [Spiess2009]: SPIEB, L.; TEICHERT, G.; SCHWARZER, R.; BEHNKEN, H. and GENZEL, C.: *Moderne Röntgenbeugung - Röntgendiffraktometrie für Materialwissenschaftler, Physiker und Chemiker, Vieweg+Teubner, GWV Fachverlage GmbH, Wiesbaden, 2009*
- [Stadelmann1987]: STADELMANN, P. A.: JEMS - a software package for electron diffraction analysis and HREM image simulation in materials science. In: *Ultramicroscopy* 21 (1987), no. 2, p. 131-145
- [Stahlschluessel2013]: STAHL SCHLÜSSEL: *Stahlschlüssel: Verlag Stahlschlüssel Wegst GmbH, Marbach, 2013*
- [Streicher2004]: STREICHER, A.; SPEER, J.; MATLOCK, D. and DE COOMAN, B.: Quenching and Partitioning Response of a Si-Added TRIP Sheet Steel. In: *AHSS Proceedings*, 2004, p. 51-62
- [Svoboda2004]: SVOBODA, J.; FISCHER, F.; FRATZL, P. and KOZESCHNIK, E.: Modelling of kinetics in multi-component multi-phase systems with spherical precipitates: I: Theory. In: *Materials Science and Engineering: A* 385 (2004), p. 166-174
- [Takahashi1989]: TAKAHASHI, M. and BHADOSHIA, H. K. D. H.: Interpretation of dilatometric data for transformations in steels. In: *Journal of Materials Science Letters* 8 (1989), no. 4, p. 477-478
- [Thomas2008]: THOMAS, G.; SPEER, J. and MATLOCK, D.: Considerations in the Application of the 'Quenching and Partitioning' Concept to Hot-Rolled AHSS Production. In: *Iron and Steel Technology* 5 (2008), no. 5, p. 209-217
- [TKSE2009]: THYSEN KRUPP STEEL EUROPE: *Produktinformation Restaustenit Stähle, Brochure, 2009*



- [VanBohemmen2008]: VAN BOHEMEN, S.; SANTOFIMIA, M. and SIETSMA, J.: Experimental evidence for bainite formation below Ms in Fe-0.66C. In: *Scripta Materialia* 58 (2008), no. 6, p. 488-491
- [VanOrstrand1915]: VAN ORSTRAND, C. E. and DEWEY, F. P.: Preliminary report on the diffusion of solids. In: *Shorter contributions to general geology* 95 (1915), p. 83-96
- [SEP1681]: VEREIN DEUTSCHER EISENHÜTTENLEUTE: STAHL-EISEN-Prüfblatt 1681 - Guidelines for preparation, execution and evaluation of dilatometric transformation tests on iron alloys, Verlag Stahleisen mbH, Düsseldorf, 1998
- [Wang2010]: WANG, C.; SHI, J.; CAO, W. and DONG, H.: Characterization of microstructure obtained by quenching and partitioning process in low alloy martensitic steel. In: *Materials Science and Engineering: A* 527 (2010), no. 15, p. 3442-3449
- [Wang2011]: WANG, X.; GUO, Z. and RONG, Y.: Mechanism exploration of an ultrahigh strength steel by quenching-partitioning-tempering process. In: *Materials Science and Engineering: A* 529 (2011), p. 35-40
- [Wang2011a]: WANG, L. and FENG, W.: Development and Application of Q&P Sheet Steels. In: WENG, Y.; DONG, H. AND GAN, Y. (ed.): *Advanced Steels*, Springer Berlin Heidelberg, 2011, p. 255-258
- [Werner1990]: WERNER, D. H.: Boron and Boron Containing Steels, Verlag Stahleisen mbH, Düsseldorf, 1990
- [White1998]: WHITE, C.; KRAUSS, G. and MATLOCK, D.: Solidification Structure and the Effects of Hot Reduction in Continuously Cast Steels for Bar and Forgings. In: *I&SM* 25 (1998), no. 9, p. 73-79
- [Wyckoff1963]: WYCKOFF, R. W. G.: Crystal structures, Interscience Publishers, 1963
- [Yang2009]: YANG, H.-S. and BHADESHIA, H. K. D. H.: Austenite grain size and the martensite-start temperature. In: *Scripta Materialia* 60 (2009), no. 7, p. 493-495
- [Zackay1967]: ZACKAY, V. F.; PARKER, E. R.; FAHR, D. and BUSH, R.: The Enhancement of Ductility in High-Strength Steels. In: *Transactions of the American Society for Metals* 60 (1967), p. 252-259
- [Zhang2011]: ZHANG, K.; ZHANG, M.; GUO, Z.; CHEN, N. and RONG, Y.: A new effect of retained austenite on ductility enhancement in high-strength quenching-partitioning-tempering martensitic steel. In: *Materials Science and Engineering A* 528 (2011), no. 29, p. 8486-8491
- [Zhong2006]: ZHONG, N.; WANG, X.; RONG, Y. and WANG, L.: Interface Migration between Martensite and Austenite during Quenching and Partitioning (Q&P) Process. In: *Journal of Materials Sciences and Technology* 22 (2006), no. 6, p. 751-754

- 
- [Zhou2012]: ZHOU, S.; ZHANG, K.; WANG, Y.; GU, J. and RONG, Y.: The mechanism of high strength-ductility steel produced by a novel quenching-partitioning-tempering process and the mechanical stability of retained austenite at elevated temperatures. In: *Metallurgical and Materials Transactions A: Physical Metallurgy and Materials Science* 43 (2012), no. 3, p. 1026-1034
- [Zhou2011]: ZHOU, S.; ZHANG, K.; WANG, Y.; GU, J. and RONG, Y.: High strength-elongation product of Nb-microalloyed low-carbon steel by a novel quenching-partitioning-tempering process. In: *Materials Science and Engineering: A* 528 (2011), no. 27, p. 8006-8012
- [Zhu2012]: ZHU, Y.; WANG, F.; ZHOU, H.; WANG, G. and JIANG, B.: Stepping-quenching-partitioning treatment of 20SiMn2MoVA steel and effects of carbon and carbide forming elements. In: *Science China Technological Sciences* 55 (2012), no. 7, p. 1838-1843

## 10. Appendix

### A. Calculated reference intensity ratios

Table A 1: Calculation of Copper radiation reference intensity ratios

i	{hkl}	$2\Theta, ^\circ$	m	$f_0$	f	$f_T$	K	F	L	P	$R_{i(hkl)}$
$\alpha$	{110}	44.67	12	18.5	17.7	0.98	2	34.6	1.87	0.75	1
$\alpha$	{200}	65.02	6	15.3	14.5	0.96	2	27.9	1.03	0.59	0.14
$\alpha$	{211}	82.33	24	13.1	12.5	0.94	2	23.4	0.77	0.51	0.25
$\gamma$	{111}	43.51	8	18.7	17.9	0.98	4	70.1	1.96	0.76	0.74
$\gamma$	{200}	50.67	6	17.5	16.7	0.97	4	64.9	1.51	0.70	0.34
$\gamma$	{220}	74.49	12	14.0	13.3	0.95	4	50.5	0.86	0.54	0.18

Table A 2: Calculation of Cobalt radiation reference intensity ratios

i	{hkl}	$2\Theta, ^\circ$	m	$f_0$	f	$f_T$	K	F	L	P	$R_{i(hkl)}$
$\alpha$	{110}	13.01	12	18.5	18.5	0.98	2	36.2	19.6	1	1
$\alpha$	{200}	18.44	6	15.3	15.3	0.96	2	29.2	9.9	1	0.16
$\alpha$	{211}	22.63	24	13.1	13.1	0.94	2	24.6	6.6	1	0.31
$\gamma$	{111}	12.68	8	18.7	18.7	0.98	4	73.2	20.6	1	0.73
$\gamma$	{200}	14.66	6	17.5	17.5	0.97	4	67.9	15.5	1	0.36
$\gamma$	{220}	20.79	12	14.0	14.0	0.95	4	53.1	7.8	1	0.22

Table A 3: Calculation of reference intensity ratios for 100 keV

i	{hkl}	$2\Theta, ^\circ$	m	$f_0$	f	$f_T$	K	F	L	P	$R_{i(hkl)}$
$\alpha$	{110}	3.51	12	18.5	18.5	0.98	2	36.2	267	1	1
$\alpha$	{200}	4.96	6	15.3	15.3	0.96	2	29.2	134	1	0.16
$\alpha$	{211}	6.07	24	13.1	13.1	0.94	2	24.6	89	1	0.31
$\gamma$	{111}	3.42	8	18.7	18.7	0.98	4	73.2	281	1	0.73
$\gamma$	{200}	3.95	6	17.5	17.5	0.97	4	67.9	211	1	0.35
$\gamma$	{220}	5.58	12	14.0	14.0	0.95	4	53.1	106	1	0.22

## B. Source code for cementite precipitation in austenite

```
$ Cementite in austenite precipitation in Fe-Cr-Mn-Si-C steel
$ Author: Niko Große-Heilmann
$ Date: 02.09.2014
$ Based on: Ernst Kozeschnik and Harry Bhadeshia "Influence of silicon
on cementite precipitation in steels" [Kozeschnik2008]
$ Materials Science and Technology 2008 VOL 24 NO 3

$ variables
set-variable-value Silicon 2 $ Si Content in wt.%
set-variable-value Carbon 2 $ C Content in wt.%
set-variable-value Manganese 0.6 $ Mn Content in wt.%
set-variable-value Chrome 1.3 $ Cr Content in wt.%
set-variable-value ttp_end_time 1e11 $ Simulation end time in s
set-variable-string tempscale 0..1200 $ default Temperature scaling
set-variable-string timescale 1..1e8 $ default Time scaling
set-variable-value ttp_max_temp 1200 $ Upper TTP-Plot Temperature
set-variable-value ttp_min_temp 25 $ Lower TTP-Plot Temperature
set-variable-value ttp_stepsize 5 $ TTP plot step size
set-variable-value npc 25 $ number of precipitate classes

$ initiate workspace
use-module core $ select core module for kinetic simulation
close-workspace f $ close any open workspace without asking for save
new-workspace $ open new workspace
@ echo n
set-workspace-info +Selected elements: $ information about the script
set-workspace-info +Fe, C, Si, Mn, Cr
set-workspace-info +Precipitation Domain: Austenite (FCC_A1)
set-workspace-info +Precipitate phases: M3C (Cementite) set-workspace-
info +Paraequilibrium Condition
echo y

$ Database and Composition
open-thermodyn-database mc_fe.tdb $ Thermodynamic database
select-elements Fe C Mn Si Cr $ select elements
select-phase fcc_a1 cementite $ select phases
read-thermodyn-database $ read thermodynamic database
read-mobility-database mc_fe.ddb $ read diffusion database
```

```
enter-composition wp c=Carbon mn=Manganese si=Silicon cr=Chrome

$calculate initial equilibrium
set-temperature-celsius 1200 $ Temperature
set-automatic-startvalues
calculate-equilibrium

$ setup plot
new-gui-window p1
set-gui-window-property . X T°C $ Temperature in Celsius on x-axis
set-plot-option . A X 1 T Temperature, °C $ x-axis title
set-plot-option . A Y 1 T Phase fraction of Cementite $ y-axis title
set-plot-option . L B $ Bottom legend
set-plot-option . A Y 1 S 0..0.5 $ Y-Axis scaling
set-plot-option . S N B F $ Cementite %s $ Plotting phase fraction
set-gui-window-property . Y b/w_no_symb $ Style b/w without symbols

$ calculate orthoequilibrium
set-step-option Y T $ "Temperature" type
set-step-option R 1200 0 L 10 $ Temperature Range and stepsize
set-step-option O C Y $ Temperature in Celsius
step-equilibrium $ calculate stepped orthoequilibrium
set-plot-option 1 S D * $ Lock all Series in Plot 1

$ plot driving force for cementite precipitation
set-temperature-celsius 1200 $ Temperature
set-automatic-startvalues $ reset
calculate-equilibrium $ calc reference equilibrium in one phase region

$ setup plot for driving force
new-gui-window p1
set-gui-window-property . X T°C $ Celsius set as variable on x-axis
set-plot-option . A X 1 T Temperature, °C $ x-axis title
set-plot-option . A Y 1 T Driving Force, J/mol $ y-axis title
set-plot-option . L B $ Bottom legend
set-plot-option . A Y 1 S 0..6000 $ Y-Axis scaling
set-plot-option . S N B DFMS $ Cementite %s $ Plotting the Driving Force
set-gui-window-property . Y b/w_no_symb $ Style b/w without symbols
```

```
$ calculate orthoequilibrium
set-step-option Y W $ "Temperature without equilibrium" type
set-step-option R 1200 0 L 10 $ Temperature Range and stepsize
set-step-option O C Y $ Temperature in Celsius
step-equilibrium $ calculate stepped othoequilibrium
set-plot-option 2 S D * $ Lock all Series in Plot 2

$ set paraequilibrium conditions for cementite
change_phase_status Cementite C Si U UN$Si $ set Cementite constrained
Si content to nominal
change_phase_status Cementite C Mn U UN$Mn $ set Cementite constrained
Mn content to nominal
change_phase_status Cementite C Cr U UN$Cr $ set Cementite constrained
Cr content to nominal

$ calculate paraequilibrium
set-temperature-celsius 1200 $ Initial Temperature 1000 °C
set-automatic-startvalues $ set startvalues
calculate-equilibrium $ calculate initial equilibrium
set-step-option Y T $ "Temperature" type
set-step-option R 1200 0 L 10 $ Temperature Range and stepsize
set-step-option O C Y $ Temperature in Celsius
step-equilibrium $ calculate stepped Paraequilibrium

$ plot setup
set-plot-option 1 S L * Y $ Lock all Series in Plot 1
set-plot-option 1 S M 0 Orthoequilibrium $ name series
set-plot-option 1 S M 1 Paraequilibrium $ name series

$ calculate driving force under paraequilibrium
set-temperature-celsius 1200 $ Temperature
set-automatic-startvalues $ reset
calculate-equilibrium $ calc reference equilibrium in one phase region
set-step-option Y W $ "Temperature without equilibrium" type
set-step-option R 1200 0 L 10 $ Temperature Range and stepsize
set-step-option O C Y $ Temperature in Celsius
step-equilibrium $ calculate stepped othoequilibrium

set-plot-option 2 S L * Y $ Lock all Series in Plot 2
set-plot-option 2 S M 0 Orthoequilibrium $ name series
```

```
set-plot-option 2 S M 1 Paraequilibrium $ name series

$ setup precipitation simulation
create-precipitation-domain austenite
set-precipitation-parameter austenite x fcc_a1 $ matrix
set-precipitation-parameter austenite T D E 1e12 $ dislocation density
for nucleation = 1E12 1/m2

$ setup cementite precipitate
create-new-phase Cementite p Cementite(aust,d) $ new precipitate
set-precipitation-parameter Cementite_p0 c npc $ # of classes
set-precipitation-parameter Cementite_p0 d austenite $ set domain
set-precipitation-parameter Cementite_p0 n s d $ nucleation sites at
dislocations
change_phase_status Cementite C Si N $ Si content to nominal
change_phase_status Cementite C Mn N $ Mn content to nominal
change_phase_status Cementite C Cr N $ Cr content to nominal
set-precipitation-parameter Cementite_p0 N C O $ set nucleus
composition to paraequilibrium
calc-nucleus-compositions $ Calculation of Nucleus

$ remove plot errors
set-simulation-parameter T I 300 $ initial data removing plot errors
set-simulation-parameter E 1e01 $ initial data removing plot errors
start-precipitate-simulation $ initial data removing plot errors

$ Output plot
new-gui-window p1 $ generate new plot: temperature
set-gui-window-property . x stepvalue $ default x-axis variable (time)
set-gui-window-property . s u y $ use default x-axis for all plots
set-gui-window-property . s t Time, s $ default x-axis title
set-gui-window-property . s f 1 $ scaling factor is 1
set-gui-window-property . S Y log $ default x-axis log scale
set-gui-window-property . S S #timescale $ default x-axis scaling
set-gui-window-property . n 2 $ 2 plot columns
set-gui-window-property . Y b/w_no_symb $ Style b/w without symbols
set-plot-option . s n b t$c $ add series: temperature
set-plot-option . s m -1 t$c T $ define series legend
set-plot-option . a y 1 t Temperature, °C $ y-axis title
set-plot-option . l n $ no legend
```

```
create-new-plot x . $ create new plot: phase fractions
set-plot-option . l a y $ replace variable names by kinetic alias
set-plot-option . s n b f_prec$* $ add all phase fractions of prec.
set-plot-option . a y 1 t Phase fraction $ change y-axis title
set-plot-option . a y 1 y log $ use logarithmic scale for y-axis
set-plot-option . a y 1 s 1e-8.. $ scale the y-axis from 1e-8..
set-plot-option . l b $ show legend at the bottom of the figure

create-new-plot x . $ create new plot: mean radii
set-plot-option . l a y $ replace variable names by kinetic alias
set-plot-option . s n b r_mean$* $ add all mean radii of precipitates
set-plot-option . a y 1 t Mean radius, nm $ change y-axis title
set-plot-option . a y 1 y log $ use logarithmic scale for y-axis
set-plot-option . a y 1 f 1e9 $ scaling factor is 1e9
set-plot-option . l b $ show legend at the bottom of the figure

create-new-plot x . $ create new plot: number densities
set-plot-option . l a y $ replace all variable names by kinetic alias
set-plot-option . s n b num_part$* $ add all number densities
set-plot-option . a y 1 t Number density, m<sup>-3</sup> $ y-axis
set-plot-option . a y 1 y log $ use logarithmic scale for y-axis
set-plot-option . a y 1 s 1.. $ scale the y-axis from 1..
set-plot-option . l b $ show legend at the bottom of the figure

move-gui-window . 50 10 700 950 $ resize/move window to new position
update-gui-window . $ update the GUI window

$ calculate ttp diagram
set-ttp-parameter E ttp_end_time $ simulation end time
set-ttp-parameter T ttp_max_temp $ Temperature max
set-ttp-parameter O ttp_min_temp $ Temperature min
set-ttp-parameter D ttp_stepsize $ step size
start-ttp-simulation $ Start TTP calculation

$ plotting ttp diagram
new-gui-window p6 $ Create TTP-Frame
set-plot-option . P R R $ Set to relative
set-plot-option . S N D Cementite_P0 0.05 $ New series 5%
```



```

set-plot-option . S M 0 "5 % Orthoequilibrium" $ 5%
set-plot-option . S N D Cementite_P0 0.95 $ New series 5%
set-plot-option . S M 1 "95 % Orthoequilibrium" $ 95%
set-plot-option . A Y 1 T Temperature, °C $ 1st y-axis title
SET_PLOT_OPTION . A Y 1 S #tempscale $ 1st y-axis scaling
set-gui-window_property . S U Y $ use default x-axis
set-gui-window_property . S Y log $ default x-axis log scale
set-gui-window_property . S S 1.. $ default x-axis scaling
set-gui-window_property . S T Time, s $ default x-axis title
set-gui-window_property . Y b/w_no_symb $ Style b/w without symbols
update-gui-windows -1 $ update windows
set-plot-option . S L * Y $ Lock all Series in Plot 2
set-plot-option . A X 1 T Time, s $ x-axis title
set-plot-option . A Y 1 T Temperature, °C $ y-axis title
set-plot-option . L B $ Bottom legend
set-plot-option . A X 1 S #timescale $ X-Axis scaling
set-plot-option . A Y 1 S #tempscale $ Y-Axis scaling

```

#### \$ Paraequilibrium Precipitation

```

set-plot-option . S N D Cementite_P0 0.05 $ New series 5%
set-plot-option . S M 2 "5 % Paraequilibrium" $ 5%
set-plot-option . S N D Cementite_P0 0.95 $ New series 95%
set-plot-option . S M 3 "95 % Paraequilibrium" $ 95%

```

```

change_phase_status Cementite C Si U UN$Si $ constrained Si
change_phase_status Cementite C Mn U UN$Mn $ constrained Mn
change_phase_status Cementite C Cr U UN$Cr $ constrained Cr

```

```

set-precipitation-parameter Cementite_p0 N C P $ set nucleus
composition to paraequilibrium

```

```

calc-nucleus-compositions $ Calculation of Nucleus

```

#### \$ start ttp calculation

```

set-ttp-parameter E ttp_end_time $ simulation end time
set-ttp-parameter T ttp_max_temp $ Temperature max
set-ttp-parameter O ttp_min_temp $ Temperature min
set-ttp-parameter D ttp_stepsize $ step size
start-ttp-simulation $ Start TTP calculation

```

```
update-gui-windows -1 $ update plots
set-plot-option 7 S L * Y $ Lock all Series in TTP Plot
set-gui-window_property . S S #timescale $ default x-axis scaling
set-plot-option . A Y 1 S #tempscale $ Y-Axis scaling
```

### C. Source Code for para-equilibrium driving force

```

$ Script to calculate driving forces for paraequilibrium cementite
precipitation in austenite in Fe-Si-Cr-Mn-C system with different
carbon contents.
$ Author: Niko Große-Heilmann
$ Date: 02.09.2014

$ variables
set-variable-value Silicon 2 $ Si Content in wt.%
set-variable-value Carbon 0.4 $ C Content in wt.%
set-variable-value Carbon1 1 $ C Content in wt.%
set-variable-value Carbon2 1.5 $ C Content in wt.%
set-variable-value Carbon3 2 $ C Content in wt.%
set-variable-value Manganese 0.6 $ Mn Content in wt.%
set-variable-value Chrome 1.3 $ Cr Content in wt.%
set-variable-string tempscale 0..400 $ default Temperature scaling
set-variable-string dfscale 0..4000 $ default driving force scale

$ setup workspace
use-module core $ select core module for kinetic simulation
close-workspace f $ close any open workspace without asking for save
new-workspace $ open new workspace
@ echo n
set-workspace-info +Selected elements: $ information
set-workspace-info +Fe, C, Si, Mn, Cr
set-workspace-info +Precipitation Domain: Austenite (FCC_A1)
set-workspace-info +Precipitate phases: M3C (Cementite) under
Paraequilibrium Condition
echo y

$setup database and chemical composition
open-thermodyn-database mc_fe.tdb $ Thermodynamic database
select-elements Fe C Mn Si Cr $ select elements
select-phase fcc_a1 cementite $ select phases
read-thermodyn-database $ read thermodynamic database
read-mobility-database mc_fe.ddb $ read diffusion database
enter-composition wp c=Carbon mn=Manganese si=Silicon cr=Chrome

$ set paraequilibrium conditions for cementite
change_phase_status Cementite C Si U UN$Si $ constrain Si

```

```
change_phase_status Cementite C Mn U UN$Mn $ constrain Mn
change_phase_status Cementite C Cr U UN$Cr $ constrain Cr

$ create plot for driving force of cementite precipitation
new-gui-window p1
set-gui-window-property . X T$C $ Celsius set as variable on x-axis
set-plot-option . A X 1 T Temperature, °C $ x-axis title
set-plot-option . A Y 1 T Driving Force, J/mol $ y-axis title
set-plot-option . L B $ Bottom legend
set-plot-option . A X 1 S #tempscale $ Y-Axis scaling
set-plot-option . A Y 1 S #dfscales $ Y-Axis scaling
set-gui-window-property . Y b/w_no_symb $ Style b/w without symbols

$ calculate driving force for Carbon level 0
set-temperature-celsius 1200 $ Temperature
set-automatic-startvalues $ reset
calculate-equilibrium $ calc reference equilibrium in one phase region
set-step-option Y W $ "Temperature without equilibrium" type
set-step-option R 1200 0 L 10 $ Temperature range and stepsize
set-step-option O C Y $ Temperature in Celsius
step-equilibrium $ calculate stepped othoequilibrium

$ setup plot
set-plot-option . S N B DFM$Cementite %s $ Plotting the Driving Force
set-plot-option . S D 0 $ Duplicate and Lock Series
set-plot-option . S M 0 "0.4 wt.% C" $ name series

$ calculate driving force for Carbon level 1
enter-composition wp c=Carbon1 $ set composition
set-temperature-celsius 1200 $ Temperature
set-automatic-startvalues $ reset
calculate-equilibrium $ calc reference equilibrium in one phase region
set-step-option Y W $ "Temperature without equilibrium" type
set-step-option R 1200 0 L 10 $ Temperature Range and stepsize
set-step-option O C Y $ Temperature in Celsius
step-equilibrium $ calculate stepped othoequilibrium

$ setup plot
set-plot-option . S D 1 $ Duplicate and Lock Series
```

```
set-plot-option . S M 1 "1.0 wt.% C" $ name series

$ calculate driving force for Carbon level 2
enter-composition wp c=Carbon2 $ set composition
set-temperature-celsius 1200 $ Temperature
set-automatic-startvalues $ reset
calculate-equilibrium $ calc reference equilibrium in one phase region
set-step-option Y W $ "Temperature without equilibrium" type
set-step-option R 1200 0 L 10 $ Temperature Range and stepsize
set-step-option O C Y $ Temperature in Celsius
step-equilibrium $ calculate stepped othoequilibrium

$ setup plot
set-plot-option . S D 2 $ Duplicate and Lock Series
set-plot-option . S M 2 "1.5 wt.% C" $ name series

$ calculate driving force for Carbon level 3
enter-composition wp c=Carbon3 $ set composition
set-temperature-celsius 1200 $ Temperature
set-automatic-startvalues $ reset
calculate-equilibrium $ calc reference equilibrium in one phase region
set-step-option Y W $ "Temperature without equilibrium" type
set-step-option R 1200 0 L 10 $ Temperature Range and stepsize
set-step-option O C Y $ Temperature in Celsius
step-equilibrium $ calculate stepped othoequilibrium

$ setup plot
set-plot-option . S D 3 $ Duplicate and Lock Series
set-plot-option . S M 3 "2.0 wt.% C" $ name series

$remove last series
set_plot_option 1 S R 4
move_gui_window 3 50 50 650 650
```

#### D. Source Code for MATCALC diffusion calculation

```
$ Isothermal diffusion simulation in Fe-Cr-Mn-Si-C austenite/ferrite
$ Author: Niko Große-Heilmann
$ Based on: Georg Stechauner's template (03.10.2011) for Darken's
$ uphill-diffusion experiment

$ make sure we are in right module
use-module core

$ create new workspace
new-workspace

$ load thermodynamic and kinetic data
open-thermodyn-database mc_fe.tdb
select-elements fe cr mn si c
select-phases fcc_a1 bcc_a2
read-thermodyn-database
read-mobility-database mc_fe.ddb

$ change the simulation parameters here
set-variable-value temp 200
set-variable-value num_cells_fcc 50 $ number of cells for fcc
set-variable-value num_cells_bcc 120 $ number of cells for bcc
set-variable-value grid_size_x 6.8e-6 $ total size of interest in m
set-variable-value sim_end_time 1e4 $ simulation end in s
set-variable-value comp_u_c 0.018290 $ carbon content in u fraction
set-variable-value comp_u_cr 0.013731 $ chromium content in u fraction
set-variable-value comp_u_si 0.039110 $ silicon content in u fraction
set-variable-value comp_u_mn 0.005998 $ mangan content in u fraction
set-variable-value num_cells_y 1 $ set initial value
set-variable-value grid_size_y 1 $ grid setup
set-variable-value grid_size_z 1 $ grid setup

$ calculated variables
set-variable-value num_cells_x num_cells_fcc+num_cells_bcc
set-variable-value num_cells_fcc_1 num_cells_fcc+num_cells_bcc/2-1
set-variable-value num_cells_bcc_1 num_cells_bcc/2
set-variable-value max_x_index num_cells_x-1 $ grid parameters
set-variable-value max_y_index num_cells_y-1 $ grid parameters
```

```
format-variable-string num_cells_fcc_1_str %d num_cells_fcc_1
format-variable-string num_cells_bcc_1_str %d num_cells_bcc_1
format-variable-string num_cells_fcc_str %d num_cells_fcc
format-variable-string max_x_index_str %d max_x_index
set-variable-string index_left_bcc 0.0
set-variable-string index_right_bcc #max_x_index_str.0
set-variable-string index_left_fcc #num_cells_bcc_1_str.0
set-variable-string index_right_fcc #num_cells_fcc_1_str.0

$ set some initial conditions
enter-composition u c=comp_u_c si=comp_u_si cr=comp_u_cr mn=comp_u_mn
set-temperature-celsius temp
calculate-equilibrium

$ create window to display 2D sample geometry
new-gui-window g5
set-variable-value paint_window_id active_frame_id $ window id
move-gui-window paint_window_id 0 100 560 300 $ 1-dim size

$ create a precipitation domain for austenite
create-precipitation-domain austenite
set-precipitation-parameter austenite x fcc_a1 $ set fcc as matrix

$ create a 2nd precipitation domain for martensite
create-precipitation-domain martensite
set-precipitation-parameter martensite x bcc_a2 $ set fcc as matrix

$ switch to simulation module ...
use-module simulation

$ create the cell structure
create-simulation-grid num_cells_x num_cells_y 1
set-grid-coordinates grid_size_x grid_size_y grid_size_z
set-grid-geometry p $ planar grid geometry

$ create a new material and couple with precipitation domain
create-material austenite
set-material-property austenite g d austenite
```

```
$ create a 2nd new material and couple with precipitation domain
create-material martensite
set-material-property martensite g d martensite

$ freeze paint frame during rest of setup
set-gui-window-property paint_window_id m y $ manual update

$ set default boundary conditions
set-default-boundary-cond g o $ open to ambient

$ initialize cell temperatures
set-cell-property a v t temp

$ initialize phases of cells
remove-cell-selection a $ unselect all cells
add-cell-selection l #index_left_bcc #index_right_bcc
set-cell-property * m martensite

remove-cell-selection a $ unselect all cells
add-cell-selection l #index_left_fcc #index_right_fcc
set-cell-property * m austenite

$ initialize cell composition
set-cell-property a v c c comp_u_c $ carbon content of all cells
set-cell-property a v c cr comp_u_cr $ carbon content of all cells
set-cell-property a v c si comp_u_si $ carbon content of all cells
set-cell-property a v c mn comp_u_mn $ manganese content of all cells

$ store in simulation state
create-simulation-state start

$ window rearrangement ...
set-gui-window-property paint_window_id i z 110 $ zoom
set-gui-window-property paint_window_id i w v $ display cell variable
set-gui-window-property paint_window_id i V _CWP$C $ set variable

$ a new window for plotting the profile ...
new-gui-window g1
```



```
set-variable-value profile_window_id active_frame_id $ window_id
set-variable-value profile_plot_id last_plot_id $ plotid
set-gui-window-property profile_window_id s u y $ use default x-axis
set-gui-window-property profile_window_id s t Distance, m $ title
set-plot-option profile_plot_id s n s _CWP$C
set-plot-option profile_plot_id s n s _CWP$Si
set-plot-option profile_plot_id s n s _CWP$Cr
set-plot-option profile_plot_id s n s _CWP$Mn
set-plot-option profile_plot_id a y 1 t Carbon content, wt.% $ title
set-plot-option profile_plot_id a y 1 s 0..2.5 $ y-axis scaling
set-gui-window-property profile_window_id I t 0.0
set-gui-window-property profile_window_id I o max_x_index.max_y_index
move-gui-window profile_window_id 100 100 600 600
set-gui-window-property profile_window_id L $ lock start values

$ simulation setup
set-simulation-parameter e sim_end_time $ simulation end time
set-simulation-parameter i a 0.01 1e+023 $ automatic step size
set-simulation-parameter u 500 $ update every x s
set-simulation-parameter d f $ diffusion field simulation
set-simulation-parameter t i temp $ temperature control: isothermal
set-simulation-parameter r g 1.05 $ store Buffer States in log

$ unfreeze paint frame
set-gui-window-property paint_window_id m n $ reset to automatic
window update $ update
update-gui-windows paint_window_id $ update

$ Settings completed. Press CTRL+J to start simulation.
```

## E. Metallography of CCT Diagram samples

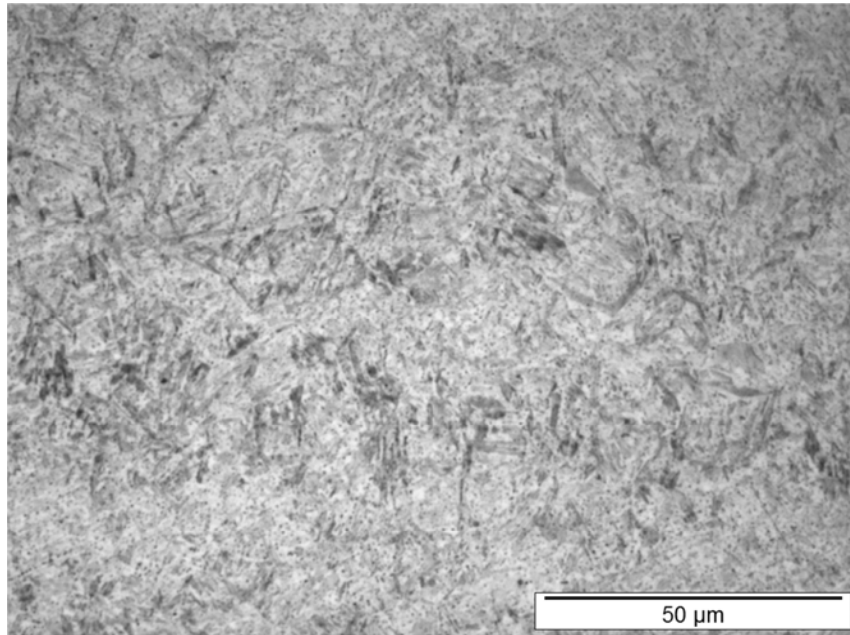


Figure E 1: Light optical micrograph of 42SiCrB steel after continuous quenching at 20 Ks<sup>-1</sup>, prepared with Nital etchant. The microstructure consists of martensite.

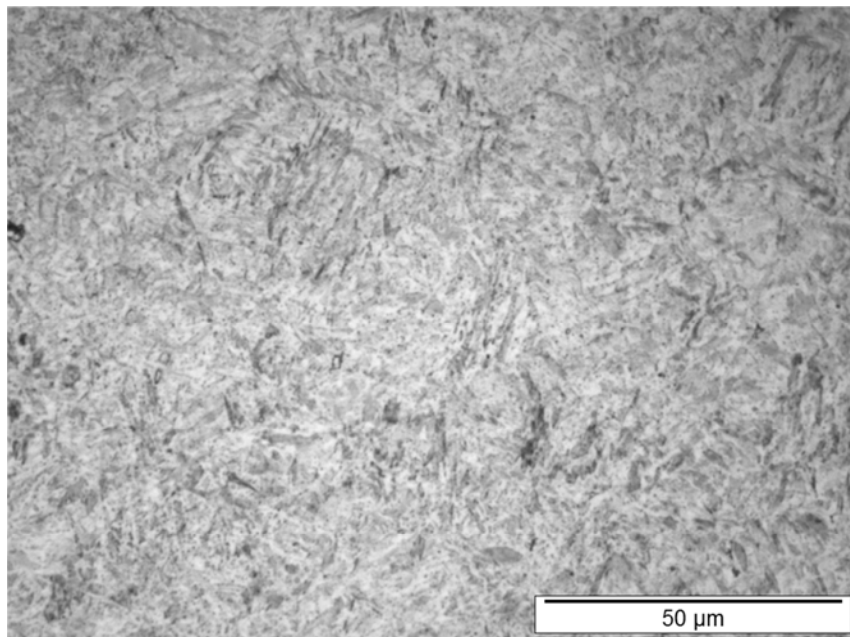


Figure E 2: Light optical micrograph of 42SiCrB steel after continuous quenching at 10 Ks<sup>-1</sup>, prepared with Nital etchant. The microstructure consists of martensite.

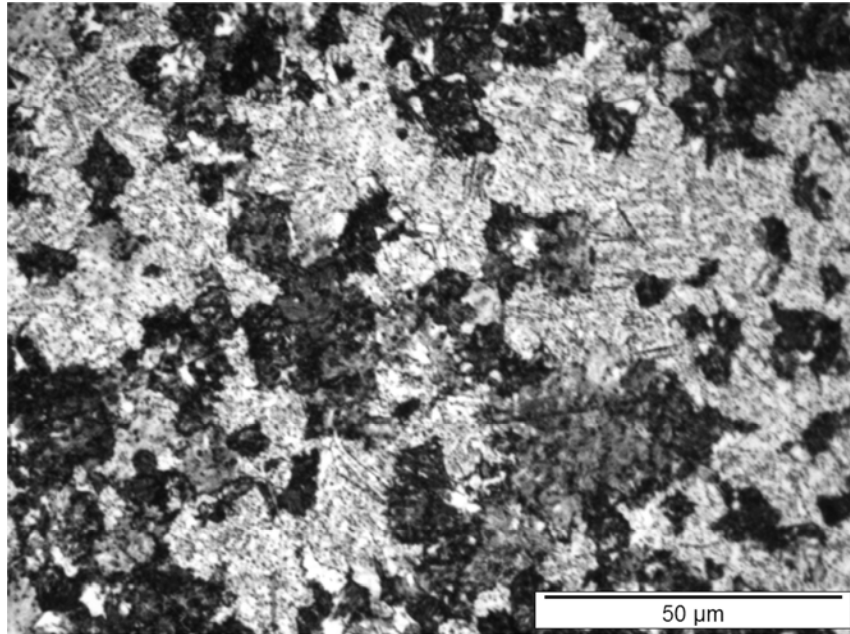


Figure E 3: Light optical micrograph of  $42\text{SiCrB}$  steel after continuous quenching at  $2\text{ Ks}^{-1}$ , prepared with Nital etchant. The microstructure consists of martensitic matrix with high amounts of black pearlite. Microscopic white ferrite isles are visible as well

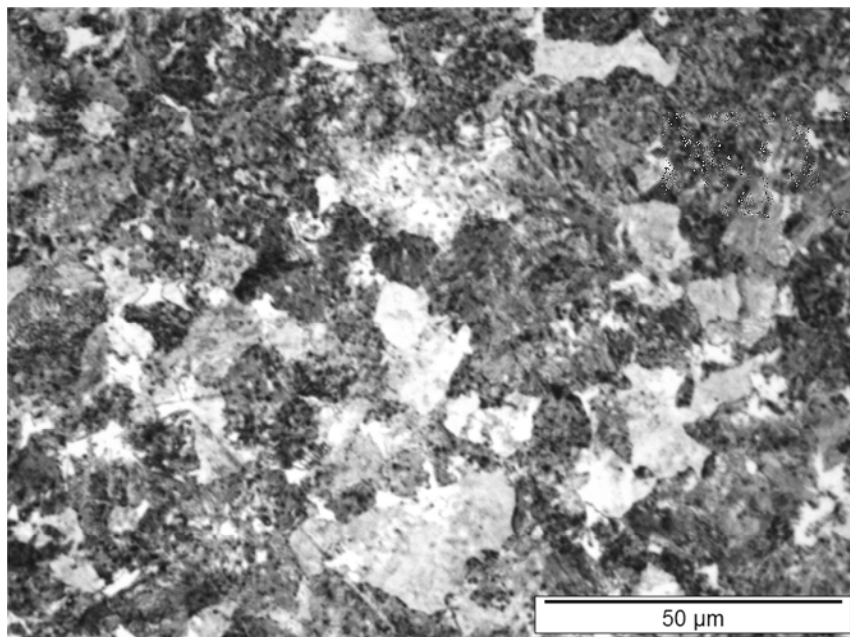


Figure E 4: Light optical micrograph of  $42\text{SiCrB}$  steel after continuous quenching at  $1\text{ Ks}^{-1}$ , prepared with Nital etchant. The microstructure consists of black pearlite and white ferrite

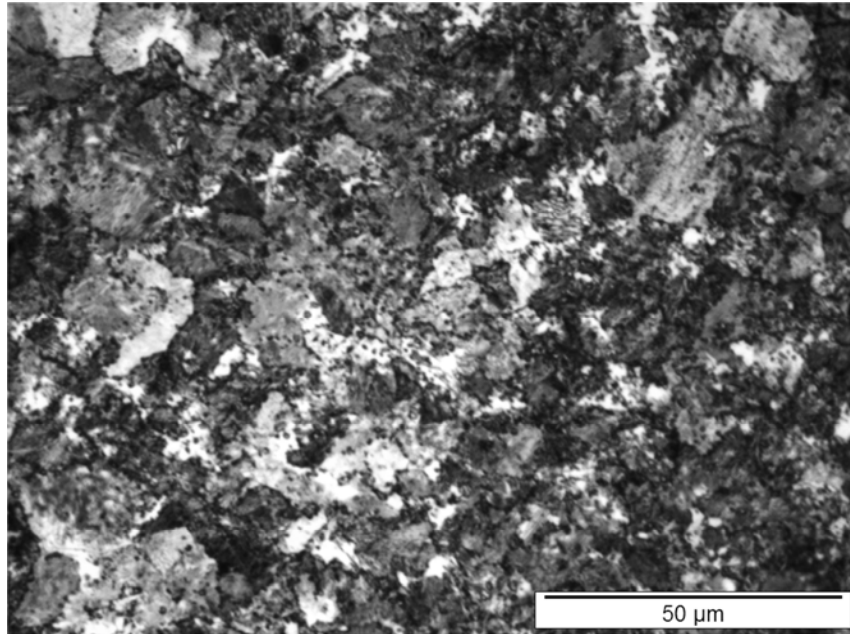


Figure E 5: Light optical micrograph of  $42\text{SiCrB}$  steel after continuous quenching at  $0.5\text{ Ks}^{-1}$ , prepared with Nital etchant. The microstructure consists of pearlite matrix, microscopic white ferrite isles are visible as well

#### F. TEM Diffraction pattern

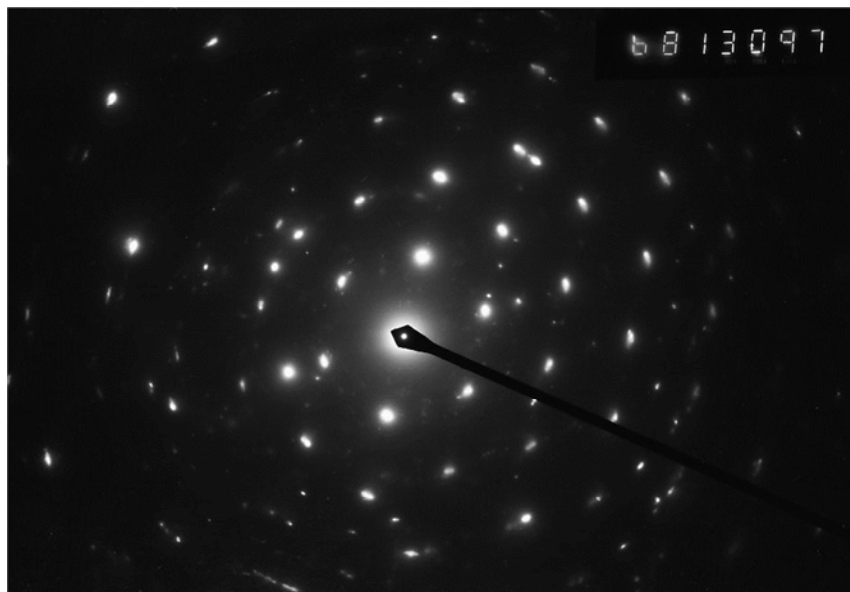


Figure F 1: TEM diffraction pattern of the  $42\text{SiCrB}$  steel after quenching to  $160\text{ }^\circ\text{C}$  and 300 s partitioning at  $475\text{ }^\circ\text{C}$ .

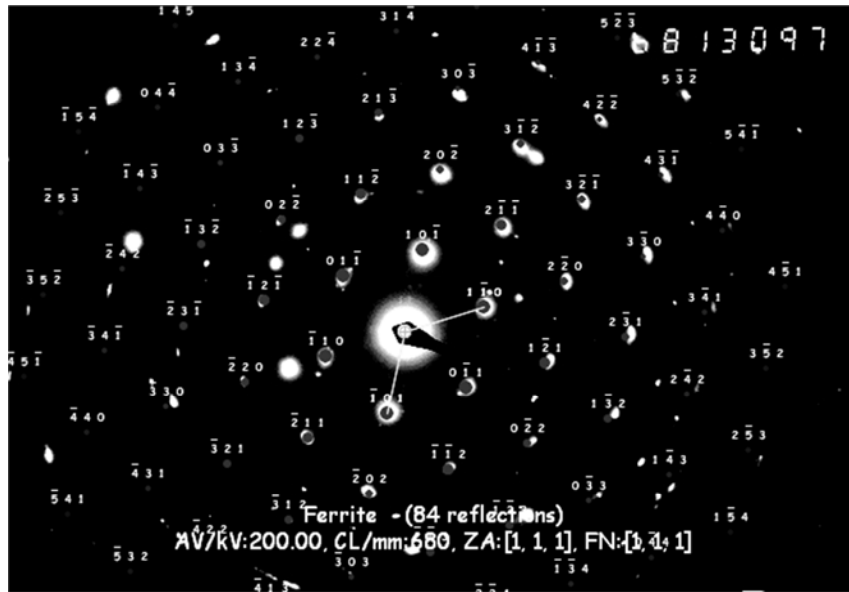


Figure E 2 TEM Diffraction pattern, with indexation of the martensitic matrix.

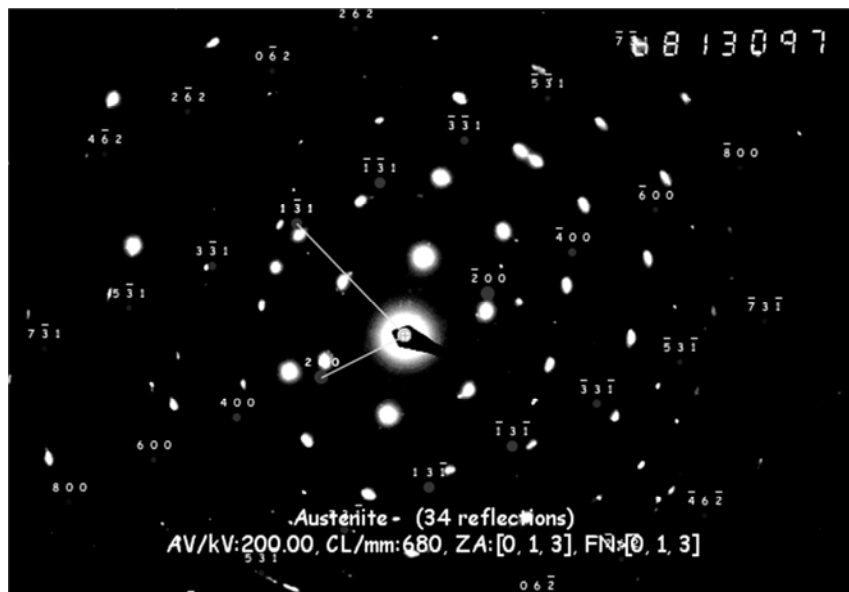


Figure E 3 TEM Diffraction pattern, with indexation of the retained austenite used for dark field imaging.

## Lebenslauf

### Persönliche Daten

Name	Niko Große-Heilmann
Geburtsdatum	9. Dezember 1980 in Warendorf
Familienstand	Verheiratet mit Daniela Große-Heilmann, geb. Fiener
Kinder	Tochter Hannah Große-Heilmann Sohn Justus Große-Heilmann

### Schulbildung

08/1986 bis 07/1990	Kardinal von Galen Grundschule, Harsewinkel
08/1990 bis 06/1999	CJD Christophorusschule-Gymnasium Versmold

Abschluss	Abitur
-----------	--------

### Studium

10/1999 bis 05/2006	Maschinenbau Studium an der Universität Paderborn Studienrichtung Produktentwicklung Schwerpunkt Metallische Werkstoffe
Abschluss	Diplom-Ingenieur
03/2011 bis heute	Doktoratsstudium der technischen Wissenschaften Technische Universität Wien Institut für Werkstoffwissenschaft und Werkstofftechnik

### Beruf

07/2006 bis 05/2008	Wissenschaftlicher Mitarbeiter Universität Paderborn Lehrstuhl für Werkstoffkunde
07/2008 bis heute	Entwicklungsingenieur Werkstofftechnik Benteler Steel/Tube GmbH, Paderborn